

Copyright
by
Hans-Peter Brecht
2007

**The Dissertation Committee for Hans-Peter Franz Brecht certifies that this
is the approved version of the following dissertation:**

**Noninvasive Optoacoustic Monitoring of Blood Oxygenation
in Large Blood Vessels**

Committee:

Rinat Esenaliev, Supervisor

Donald Prough , Co-Supervisor

Harvey Fishman

Massoud Motamedi

Gracie Vargas

Dean Graduate School of
Biomedical Sciences

Stanislav Emelianov

**Noninvasive Optoacoustic Monitoring of Blood Oxygenation
in Large Blood Vessels**

by

Hans-Peter Franz Brecht, B.S.

Dissertation

Presented to the Faculty of the Graduate School of

The University of Texas Medical Branch

in Partial Fulfillment

of the Requirements

for the Degree of

Doctor of Philosophy

The University of Texas Medical Branch

December, 2007

Dedication

My family and friends that helped and supported me along the way.

Acknowledgements

Brent Bell

Inga Cicinaite

Donald Deyo

Igor Patrikeev

Yuri Petrov

Irina Petrova

Donald Prough

Noninvasive Optoacoustic Monitoring of Blood Oxygenation in Large Blood Vessels

Publication No. _____

Hans-Peter Brecht, PhD

The University of Texas Medical Branch, 2007

Supervisor: Rinat Esenaliev

Continuous monitoring of cerebral blood oxygenation is critically important for successful treatment of patients with severe traumatic brain injury and patients undergoing cardiac surgery. At present, the techniques for monitoring blood oxygenation are invasive. We propose the noninvasive monitoring of cerebral venous blood hemoglobin saturation (SvO_2) by optoacoustic probing of blood circulating in the internal jugular vein (IJV). This thesis describes the tests of the optoacoustic system with three different probes in phantoms, *in vitro*, and *in vivo* in sheep along with different data processing algorithms. A LabView®-based scanning system, that automatically moves the optoacoustic probe across the IJV while continuously taking measurements, was developed and used for testing the optoacoustic probes. Automatic signal processing determined the signal with the best probe-vessel alignment which was then used for further processing. The scanning system was tested in phantoms using solutions with different absorption coefficients and with blood at various levels of hemoglobin

saturation (SO_2). Amplitudes and profiles of the optoacoustic signals recorded from the phantoms closely followed the SO_2 changes in accordance with blood optical properties. These data indicate that the scanning system is capable of improving the accuracy of noninvasive monitoring of hemoglobin saturation by minimizing errors associated with lateral misalignment of the probe with respect to blood vessels.

Table of Contents

Dedication.....	IV
Acknowledgements.....	V
Table of Contents.....	VIII
List of Tables.....	XI
List of Figures.....	XII
List of Abbreviations.....	XVIII
CHAPTER 1: INTRODUCTION	1
Clinical Importance.....	1
Existing techniques for cerebral blood oxygenation monitoring.....	1
Anatomy and resulting implications for optoacoustic monitoring.....	5
CHAPTER 2: THEORY AND PRINCIPLES OF OPTOACOUSTICS	7
Optoacoustic Wave Detection: Transmission Mode.....	11
Optoacoustic Wave Detection: Reflection Mode.....	12
Optoacoustic Probe.....	13
Ideal optoacoustic probe.....	13
Considerations for the Optoacoustic Probe Design.....	13

CHAPTER 3: EXPERIMENTAL SETUP	17
CHAPTER 4: PIEZOCERAMIC PROBE DESIGN AND RATIONALE AND TEST	20
Probe Test.....	22
CHAPTER 5: PHANTOM STUDIES WITH THE PIEZOCERAMIC PROBE	25
CHAPTER 6: <i>IN VIVO</i> STUDIES OF THE PIEZOCERAMIC PROBE WITH SHEEP	29
CHAPTER 7: INTERMEDIATE PROBE DESIGNS	45
CHAPTER 8: PVDF PROBE DESIGN AND RATIONALE AND TEST	48
Probe Test.....	50
Scanning Setup	51
Angular Sensitivity.....	52
CHAPTER 9: PHANTOM STUDIES WITH TH PVDF PROBE	54
Experimental Setup.....	54
Phantom Preparation.....	54
Scanning Setup	55
CHAPTER 10: <i>IN VITRO</i> STUDIES WITH THE PVDF PROBE	63
Phantom Preparation.....	63
CHAPTER 11: DESIGN RATIONALE AND TEST OF PVDF PROBE 2	72
Probe Design	72
Probe Test.....	73
Angular Sensitivity.....	76
CHAPTER 12: PHANTOM STUDIES WITH PVDF PROBE2	77
Experimental Setup.....	77
Phantom Preparation.....	78
Scanning Setup	78
CHAPTER 13: <i>IN VITRO</i> STUDIES WITH PVDF PROBE2	82

Phantom Preparation.....	82
Experimental setup	82
CHAPTER 14: IN VIVO STUDIES WITH PVDF PROBE 2 IN VOLUNTEERS	94
Experimental Setup.....	94
CHAPTER 15: DISCUSSION	101
Piezoceramic probe:	101
PVDF Probe 1.....	103
PVDF Probe 2.....	105
Further Development of the Optoacoustic System.....	107
Data Aquisition.....	107
Probe.....	107
Other data processing algorithms.....	108
CHAPTER 16: CONCLUSION	114
GLOSSARY	116
APPENDIX	117
In Vivo studies in sheep (Additional Graphs).....	117
Block Diagrams of Labview programs used for data acquisition and processing	122
Program for data acquisition of a single file.....	122
Program for data acquisition and probe scanning	123
Program for determination of value of integral	123
Program for determination of power spectrum	124
Program for determination of the exponential coefficient	124
REFERENCES	125

List of Tables

TABLE 1: CENTRAL FREQUENCY GENERATED IN BLOOD WITH DIFFERENT ATTENUATION COEFFICIENTS.	14
TABLE 2: COMPARATIVE CHART OF THE ELECTRO-ACOUSTICAL PROPERTIES FOR DIFFERENT PIEZO-ELECTRICAL MATERIALS [⁴⁹].	15

List of Figures

FIGURE 1: ABSORPTION COEFFICIENTS OF WATER, OXYGENATED AND DEOXYGENATED BLOOD WITH A HEMATOCRIT OF 5% [12].	2
FIGURE 2: MEASUREMENT OF CEREBRAL SO₂ UTILIZING INFRARED SPECTROSCOPY.	4
FIGURE 3: TOP: DIAGRAM OF THE HUMAN NECK SHOWING THE LOCATION OF INTERNAL JUGULAR VEIN ON EITHER SIDE OF THE NECK NEXT TO THE CAROTID ARTERY AND SOME OF THE SUPPLYING BLOOD VESSELS [46]. BOTTOM: ULTRASOUND IMAGE OF THE IJV LOCATED AT A DEPTH OF 1 CM WITH A DIAMETER OF 1 CM.	6
FIGURE 4: PRINCIPLES OF OPTOACOUSTIC SIGNAL GENERATION.	7
FIGURE 5: DETECTION OF OPTOACOUSTIC PULSES IN TRANSMISSION MODE (LEFT).	11
FIGURE 6: DETECTION OF OPTOACOUSTIC PULSES IN REFLECTION MODE (LEFT). INTENSITY DISTRIBUTION IN THE MEDIUM (MIDDLE) AND RESULTING OPTOACOUSTIC SIGNAL DETECTED IN REFLECTION MODE (RIGHT).	12
FIGURE 7: TUNING CURVE OPOLETTE532 TYPE II AS STATED FROM THE MANUFACTURER.	17
FIGURE 8: OPTOACOUSTIC SETUP FOR <i>IN VIVO</i> STUDIES	18
FIGURE 9: TYPICAL GAIN PLOT OF THE AH-17PD AMPLIFIER.	19
FIGURE 10: SCHEMATIC REPRESENTATION OF THE PIEZOCERAMIC OPTOACOUSTIC PROBE.	21
FIGURE 11: TWO SQUARE PULSE WITH DIFFERENT PULSE WIDTHS (A) AND CORRESPONDING POWER SPECTRUM OF THE WIDE (B) AND NARROW (C) PULSE.	22
FIGURE 12: OPTOACOUSTIC SIGNAL DERIVED FROM 2-MM THICK BLACK RUBBER WITH ULTRA HIGH ABSORPTION COEFFICIENT.	23
FIGURE 13: VOLTAGE SPECTRUM OF OPTOACOUSTIC SIGNAL DERIVED FROM 2-MM THICK BLACK RUBBER WITH ULTRA HIGH ABSORPTION COEFFICIENT.	24
FIGURE 14: SCHEMATIC REPRESENTATION OF THE EXPERIMENT WITH THE JUGULAR VEIN PHANTOM.	26

FIGURE 15: SIGNAL FROM THE PROBE AT VARIOUS VERTICAL DISPLACEMENTS. THE ENERGY USED WAS 25 μJ AND THE ABSORPTION COEFFICIENT OF THE SOLUTION WAS 15 cm^{-1}.	27
FIGURE 16: OPTOACOUSTIC SIGNAL RECORDED FROM THE JUGULAR VEIN PHANTOM AT VARIOUS LATERAL DISPLACEMENTS.	28
FIGURE 17: OPTOACOUSTIC SIGNALS GENERATED AT 700, 800, AND 1064 NM AT BLOOD OXYGENATIONS OF (A) 91.9%, (B) 54.6%, AND (C) 19% [⁵⁸].	32
FIGURE 18: TIME COURSE OF BLOOD OXYGENATION (BLACK SQUARES) AND OPTOACOUSTIC SIGNAL AMPLITUDES AT 700 NM (BLUE FILLED CIRCLES) AND 1064 NM (RED TRIANGLES).	34
FIGURE 19: OPTOACOUSTIC SIGNAL AMPLITUDES AT 700 NM (BLUE FILLED CIRCLES) AND 1064 NM (RED SQUARES) NORMALIZED TO THE SIGNAL AMPLITUDE AT 805 NM.	35
FIGURE 20: DIAGRAM OF THE DATA PROCESSING ALGORITHM.	37
FIGURE 21: TIME COURSE OF BLOOD OXYGENATION (BLACK SQUARES), AND INTEGRATED OPTOACOUSTIC SIGNALS FOR 700 NM (BLUE FILLED CIRCLES) AND 1064 NM (RED TRIANGLES).	38
FIGURE 22: CORRELATION OF TEMPORAL INVERSE INTEGRAL RATIO WITH BLOOD OXYGENATION AT 700 NM (BLUE FILLED CIRCLES) AND 1064 NM (RED SQUARES)	39
FIGURE 23: RATIO OF TEMPORAL PROFILES 700 NM / 1064 NM OF SHEEP FROM BOTH CYCLES (BLUE FILLED CIRCLES) AND DERIVED FROM COMPUTER MODELING USING MONTE CARLO SIMULATION (RED SQUARES) [⁵⁸].	41
FIGURE 24: RATIO OF NORMALIZED AMPLITUDES 1064 NM / 700 NM OF ALL SHEEP.	42
FIGURE 25: RATIO OF TEMPORAL PROFILES 700 NM / 1064 NM OF ALL SHEEP.	43
FIGURE 26: SCHEMATIC REPRESENTATION OF THE 10 MHZ PIEZOCERAMIC OPTOACOUSTIC PROBE.	45
FIGURE 27: TWO OPTOACOUSTIC SIGNALS DERIVED FROM 2-MM THICK BLACK RUBBER WITH ULTRA HIGH ABSORPTION COEFFICIENT.	46
FIGURE 28: SCHEMATIC REPRESENTATION OF THE PVDF PROBE CUT LENGTHWISE OVERLYING THE JUGULAR VEIN PHANTOM.	49

FIGURE 29: OPTOACOUSTIC SIGNAL MEASURED FROM 2-MM THICK BLACK RUBBER WITH ULTRA HIGH ABSORPTION COEFFICIENT.	50
FIGURE 30: VOLTAGE SPECTRUM OF OPTOACOUSTIC SIGNAL MEASURED FROM THE 2-MM THICK STRONG ABSORBING RUBBER.	51
FIGURE 31: NORMALIZED OPTOACOUSTIC SIGNAL AMPLITUDE VERSUS THE ANGLE OF DETECTION OF THE TRANSDUCER.	53
FIGURE 32: TYPICAL SCAN OF THE OPTOACOUSTIC PROBE ACROSS A JUGULAR PHANTOM (D = 9.8 MM) FILLED WITH NAPHTHOL GREEN SOLUTION ($\mu_A = 15 \text{ CM}^{-1}$).	56
FIGURE 33: OPTOACOUSTIC SIGNALS RECORDED FROM THE 9.8-MM JUGULAR PHANTOM FILLED WITH DYE SOLUTIONS OF DIFFERENT ABSORPTION COEFFICIENTS AND WATER.	57
FIGURE 34: OPTOACOUSTIC SIGNALS RECORDED FROM THE 9.8-MM JUGULAR PHANTOM FILLED WITH DYE SOLUTIONS OF DIFFERENT ABSORPTION COEFFICIENTS AFTER WATER BACKGROUND SUBTRACTION.	58
FIGURE 35: CORRELATION BETWEEN THE INVERSE INTEGRAL OF OPTOACOUSTIC SIGNALS IN THE BACKWARD DETECTION AND ACTUAL ABSORPTION COEFFICIENT IN SILICONE TUBES (9.8 AND 12.7 MM).	59
FIGURE 36: DIAGRAM OF THE DATA PROCESSING ALGORITHM UTILIZING THE EXPONENTIAL FIT.	60
FIGURE 37: CORRELATION BETWEEN MEASURED EXPONENTIAL COEFFICIENT OF OPTOACOUSTIC SIGNALS IN THE BACKWARD DETECTION AND REAL ABSORPTION COEFFICIENT IN SILICONE TUBES (9.8 AND 12.7 MM).	61
FIGURE 38: MULTIPLE SCANS ACROSS A 12.7-MM JUGULAR PHANTOM CONTAINING SHEEP BLOOD WITH BLOOD OXYGENATION RANGING FROM 94.3% TO 14.5%.	64
FIGURE 39: OPTOACOUSTIC SIGNALS RECORDED FROM THE 9.8-MM JUGULAR PHANTOM FILLED WITH SHEEP BLOOD OF DIFFERENT LEVELS OF BLOOD OXYGENATION.	65
FIGURE 40: CORRELATION BETWEEN INVERSE INTEGRAL AND BLOOD OXYGENATION <i>IN VITRO</i> IN A SILICONE TUBE WITH A DIAMETER OF 12.7 MM.	66

FIGURE 41: CORRELATION BETWEEN EXPONENTIAL COEFFICIENT AND BLOOD OXYGENATION IN TWO SILICONE TUBES WITH A DIAMETER OF 9.8 AND 12.7 MM.	67
FIGURE 42: CORRELATION BETWEEN OPTOACOUSTIC SIGNAL AMPLITUDES AND BLOOD OXYGENATION AT VARIOUS LATERAL DISPLACEMENTS (0, 1.2, 2.0, AND 2.8 MM).	69
FIGURE 43: CORRELATION OF THE EXPONENTIAL COEFFICIENT WITH BLOOD OXYGENATION AT VARIOUS DISPLACEMENTS (0, 1.2, 2.0, AND 2.8 MM).	70
FIGURE 44: SCHEMATIC REPRESENTATION OF THE THIRD PVDF PROBE.	73
FIGURE 45: OPTOACOUSTIC SIGNAL RECORDED BY THE NEW PROBE FROM 2-MM THICK BLACK RUBBER WITH VERY HIGH ABSORPTION COEFFICIENT.	74
FIGURE 46: FREQUENCY RESPONSE OF THE NEW PVDF OPTOACOUSTIC PROBE.	75
FIGURE 47: NORMALIZED OPTOACOUSTIC SIGNAL AMPLITUDE VERSUS ANGLE OF INCIDENCE ON THE PROBE.	76
FIGURE 48: OPTOACOUSTIC SIGNALS RECORDED FROM THE 12.7-MM JUGULAR PHANTOM FILLED WITH DYE SOLUTIONS OF DIFFERENT ABSORPTION COEFFICIENTS BEFORE WATER BACKGROUND SUBTRACTION.	79
FIGURE 49: OPTOACOUSTIC SIGNALS RECORDED FROM THE 12.7-MM JUGULAR PHANTOM FILLED WITH DYE SOLUTIONS OF DIFFERENT ABSORPTION COEFFICIENTS AFTER WATER BACKGROUND SUBTRACTION.	80
FIGURE 50: CORRELATION BETWEEN EXPONENTIAL SLOPE OF OPTOACOUSTIC SIGNALS AND ACTUAL ABSORPTION COEFFICIENT IN THE SILICONE TUBE.	81
FIGURE 51: EXPERIMENTAL SETUP FOR <i>IN VITRO</i> STUDIES.	84
FIGURE 52: OPTOACOUSTIC SIGNALS RECORDED FROM THE 25.4-MM JUGULAR PHANTOM FILLED WITH SHEEP BLOOD OF DIFFERENT BLOOD OXYGENATIONS (96.5% TO 49%).	85
FIGURE 53: OPTOACOUSTIC SIGNALS FROM THE 25.4-MM JUGULAR PHANTOM FILLED WITH SHEEP BLOOD OF VARYING BLOOD OXYGENATION (49% TO 96.5%) AFTER WATER SUBTRACTION.	86

FIGURE 54: NORMALIZED OPTOACOUSTIC SIGNAL AMPLITUDE FOR JUGULAR PHANTOM OF VARIOUS DIAMETERS (15.8, 19.05, AND 25.4 MM)	87
FIGURE 55: OPTOACOUSTIC SIGNALS RECORDED FROM THE 12.7-MM JUGULAR PHANTOM FILLED WITH BLOOD ($SAO_2 = 94.8\%$) SURROUNDED BY INTRALIPID SOLUTION OF DIFFERENT CONCENTRATIONS (1/200, 1/100, 1/50, AND 1/25).	88
FIGURE 56: NORMALIZED OPTOACOUSTIC SIGNALS RECORDED FROM THE 12.7-MM JUGULAR PHANTOM FILLED WITH BLOOD ($SAO_2 = 94.8\%$) SURROUNDED BY INTRALIPID SOLUTION OF DIFFERENT CONCENTRATIONS (1/200, 1/100, AND 1/50).	89
FIGURE 57: OPTOACOUSTIC SIGNALS RECORDED FROM THE 9.8-MM JUGULAR PHANTOM FILLED WITH BLOOD OF VARIOUS SO_2 LEVELS SURROUNDED BY A 1/100 DILUTION OF INTRALIPID SOLUTION ($\mu_{EFF} = 1 \text{ cm}^{-1}$).	90
FIGURE 58: NORMALIZED OPTOACOUSTIC SIGNALS RECORDED FROM THE 9.8-MM JUGULAR PHANTOM FILLED WITH BLOOD OF VARIOUS SO_2 LEVELS SURROUNDED BY A 1/200 DILUTION OF INTRALIPID SOLUTION.	91
FIGURE 59: CORRELATION INVERSE INTEGRAL WITH BLOOD OXYGENATION FOR THE 9.8- AND 12.7-MM JUGULAR PHANTOMS FILLED WITH BLOOD OF VARIOUS BLOOD OXYGENATIONS SURROUNDED BY A 1/200 DILUTION OF INTRALIPID SOLUTION.	92
FIGURE 60: AMPLITUDE CORRELATION OF OPTOACOUSTIC SIGNALS WITH SO_2 FOR THE 9.8- AND 12.7-MM JUGULAR PHANTOMS FILLED WITH BLOOD OF VARIOUS BLOOD OXYGENATIONS SURROUNDED BY A 1/200 DILUTION OF INTRALIPID SOLUTION.	93
FIGURE 61A: ULTRASOUND IMAGE OF THE EXTERNAL JUGULAR VEIN OF A FEMALE HEALTHY VOLUNTEER.	95
FIGURE 61B: CORRESPONDING OPTOACOUSTIC SIGNAL MEASURED FROM THE EXTERNAL JUGULAR VEIN OF A HEALTHY FEMALE VOLUNTEER.	96
FIGURE 62A: ULTRASOUND IMAGE OF INTERNAL JUGULAR VEIN OF A HEALTHY FEMALE VOLUNTEER.	97
FIGURE 62B: CORRESPONDING OPTOACOUSTIC SIGNAL MEASURED FROM THE INTERNAL JUGULAR VEIN OF A HEALTHY FEMALE VOLUNTEER.	98
FIGURE 63A: ULTRASOUND IMAGE OF INTERNAL JUGULAR VEIN OF A MALE HEALTHY VOLUNTEER.	99

FIGURE 63B: CORRESPONDING OPTOACOUSTIC SIGNAL MEASURED FROM THE IJV OF A HEALTHY MALE VOLUNTEER.	99
FIGURE 64: VOLTAGE SPECTRUM OF OPTOACOUSTIC SIGNAL MEASURED FROM 2-MM THICK BLACK RUBBER WITH VERY HIGH ABSORPTION COEFFICIENT USING THE PIEZOCERAMIC AND PVDF PROBES.	103
FIGURE 65: COMPUTED ILLUMINATION OF A 10-MM DIAMETER BLOOD VESSEL WITH AN ABSORPTION COEFFICIENT OF 5 cm^{-1} (LEFT) AND 30 cm^{-1} (RIGHT).	104
FIGURE 66: POWER SPECTRUM OF THE OPTOACOUSTIC SIGNAL DERIVED FROM THE EXTERNAL JUGULAR VEIN OF SHEEP FOR THREE DIFFERENT BLOOD OXYGENATIONS (16.3%, 64.1%, AND 94.8%) AT THE WAVELENGTH OF 700 NM.	110
FIGURE 67: POWER SPECTRUM OF THE OPTOACOUSTIC SIGNAL DERIVED FROM THE 9.8-MM JUGULAR VEIN PHANTOM FILLED WITH ABSORBING SOLUTION (5, 10, 15 AND 20 cm^{-1}).	111
FIGURE 68: A) EXPONENTIAL DECAY OF THE OPTOACOUSTIC SIGNALS FROM THE PHANTOM STUDIES (FIGURE 43); B) POWER SPECTRUM OF THE EXPONENTIAL DECAY OF THE OPTOACOUSTIC SIGNAL DERIVED FROM THE 9.8-MM JUGULAR VEIN PHANTOM FILLED WITH ABSORBING SOLUTION (5, 10, 15 AND 20 cm^{-1}).	112
FIGURE 69: TIME COURSE OF OPTOACOUSTIC SIGNAL AMPLITUDES AT 700 NM (BLUE FILLED CIRCLES) AND 1064 NM (RED TRIANGLES) WITH RESPECT TO BLOOD OXYGENATION (BLACK SQUARES).	117
FIGURE 70: OPTOACOUSTIC SIGNAL AMPLITUDES AT 700 NM (BLUE FILLED CIRCLES) AND 1064 NM (RED EMPTY SQUARES) CORRECTED WITH THE OPTOACOUSTIC SIGNAL AMPLITUDE AT 800 NM FOR VARIATIONS IN INCIDENT LASER POWER.	118
FIGURE 71: TIME COURSE OF UTILIZING TEMPORAL PROFILE AT 700 NM (BLUE FILLED CIRCLES) AND 1064 NM (GREEN TRIANGLES) WITH RESPECT TO BLOOD OXYGENATION (BLACK FILLED DIAMONDS). GRAPH SHOWS BOTH CYCLES.	119
FIGURE 72: CORRELATION OF TEMPORAL PROFILES WITH BLOOD OXYGENATION AT 700 NM (BLUE FILLED CIRCLES) AND 1064 NM (RED SQUARES) CORRECTED FOR VARIATIONS IN INCIDENT LASER POWER.	120
FIGURE 73: RATIO OF TEMPORAL PROFILED 700/1064 NM FOR ALL FOUR SHEEP AT BOTH CYCLES (1ST CYCLE BLUE DIAMONDS 2ND CYCLE RED SQUARES).	121

List of Abbreviations

A.U. = Arbitrary Units

EJV = External Jugular Vein

FiO₂ = Fraction of Inspired Oxygen

FWHM = Full Width Half Maximum

HWHM = Half Width Half Maximum

ID = Inner Diameter

IJV = Internal Jugular Vein

MPE = Maximal Permissible Exposure

OPO = Optical Parametric Oscillator

PVC-P = Polyvinylchloride – plastisol

PVDF = Polyvinylidene Fluoride

RBC = Red Blood Cell

SO₂ = Oxygen Saturation of Hemoglobin

SaO₂ = Arterial Oxygen Saturation of Hemoglobin

SjvO₂ = Jugular Vein Oxygen Saturation of Hemoglobin

SNR = Signal-to-Noise Ratio

tHb = Total Hemoglobin Concentration

TTL = Transistor-Transistor Logic

US = Ultrasound

CHAPTER 1: INTRODUCTION

Clinical Importance

Of an estimated 1.4 million traumatic brain injuries that occur each year in the US, approximately 6% result in permanent disability, and 3.6% result in death [1]. Current treatment strategies are aimed at minimizing additional brain damage due to secondary mechanisms such as edema, ischemia, and hypoxia. In the intensive care unit, secondary injury is detected through monitoring of cerebral hemodynamics, electrical activity, and the percentage of oxygen-saturated hemoglobin (i.e., the ratio of oxygen-bound hemoglobin to total hemoglobin) in the cerebral circulation. Continuous monitoring of the percentage of hemoglobin saturation (SO_2) can greatly improve the outcome for these patients [2-8].

Existing techniques for cerebral blood oxygenation monitoring

Currently, there are two methods for monitoring cerebral blood oxygenation. One method utilizes near infrared spectroscopy, which detects changes in the absorption coefficient of hemoglobin upon binding oxygen (see Figure 1). Near infrared spectroscopy can be applied invasively or noninvasively. The invasive method involves placement of a fiber-optic probe through a catheter into the IJV to measure continuously the percentage of oxygenated hemoglobin in the internal jugular vein ($SjvO_2$). The disadvantages of this method are invasiveness, and accuracy that varies depending on catheter tip placement. The noninvasive method provides a measurement of the local SO_2 of both cerebral blood and tissue by utilizing photon migration to determine the depth in

the sample where the spectroscopic signal is generated [9]. Photon migration assumes the most likely path of the signal, but due to the multi-layered structure of the head and strong light scattering in the tissue, this method is very inaccurate.

Another method uses a trans-cranial probe to measure directly the partial pressure of oxygen (pO_2), which reflects the amount of oxygen dissolved in the blood [10,11]. This method is invasive and provides an indication of only regional oxygenation; therefore, its clinical use is limited.

The existing cerebral SO_2 monitoring systems are based on infrared spectroscopy, which utilizes the change in the absorption coefficient of hemoglobin upon binding oxygen.

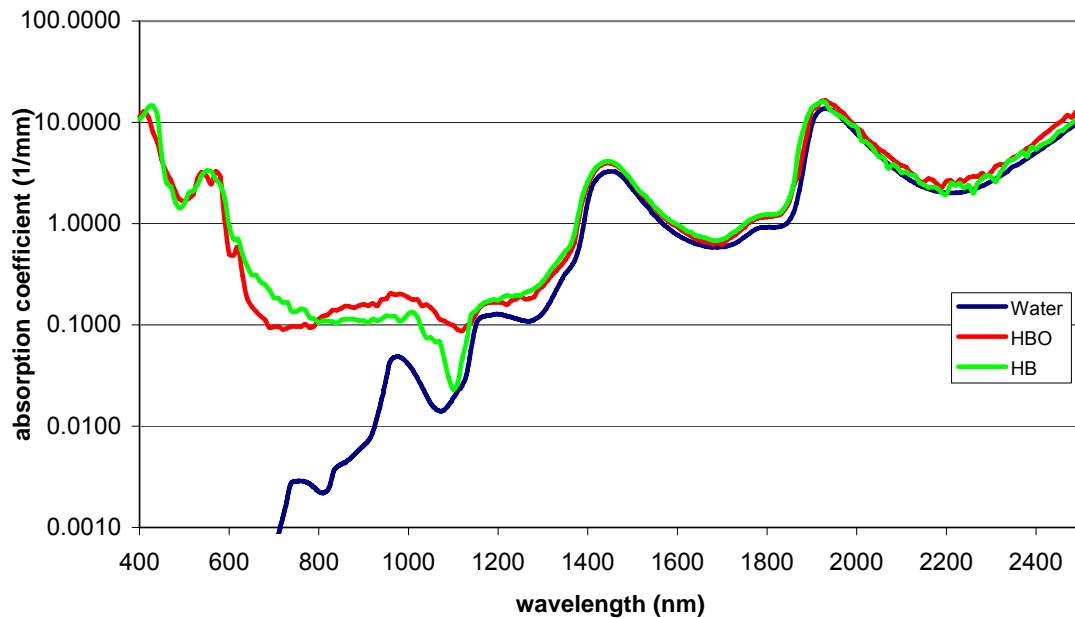


Figure 1: Absorption coefficients of water, oxygenated and deoxygenated blood with a hematocrit of 5% [12]. Note that the absorption coefficients of oxygenated and deoxygenated blood are the same at 800 nm, allowing the use of this wavelength as a reference point known as the isosbestic point.

The SO_2 can be measured from the ratio of the absorption coefficients determined at two wavelengths. One wavelength is located below 800 nm where the absorption coefficient of deoxygenated blood is higher than that of oxygenated blood. The other is located above 800 nm where the absorption coefficient of oxygenated blood is higher than that of deoxygenated blood. At 800 nm, the absorption coefficient of oxy- and deoxygenated blood is the same. This specific wavelength is a useful reference point known as the isosbestic point (isos, Greek meaning equal).

As described above, the jugular venous catheter facilitates these measurements directly in the jugular bulb using optical fibers that direct the light towards the measurement site. This direct contact between light and blood makes spectroscopic detection using a catheter potentially very accurate; however, problems with the catheter method are: a) invasiveness, b) measurement variability, which depends on catheter tip placement (e.g., near the vessel wall), and c) blood clot formation at the catheter tip. Inaccuracies in the determination of SO_2 can occur when the catheter tip is placed incorrectly and/or when a blood clot forms at the catheter tip causing the loss of direct contact with circulating blood.

Alternatively, near-infrared spectroscopy can be used noninvasively to measure SO_2 in the cerebrum (Figure 2) [^{13,14}]. Even though most photons traveling in the tissue from the light source to the detector follow the indicated mean path, a significant percentage of photons that contribute to the detected signal take a different path. Due to the multiple light paths that deviate from the mean path, this noninvasive method is also inaccurate in monitoring the SO_2 [^{15,16}]. Additionally, this method cannot measure venous blood oxygenation because it measures a signal from a mixture of arterial, capillary, and venous blood.

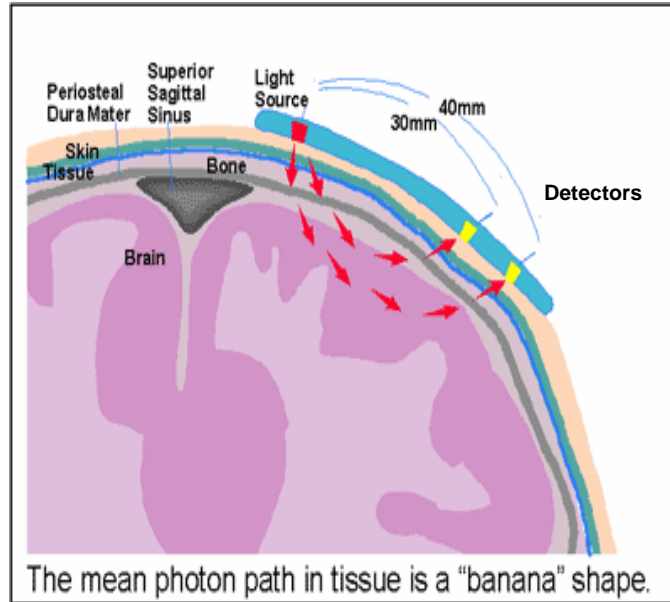


Figure 2: Measurement of cerebral SO_2 utilizing infrared spectroscopy. Photons exit the light source, travel through the cerebrum, and are detected as they exit the head. The most probable “mean” photon path is indicated by the arrows.^[17]

Presently, a system capable of noninvasively and accurately monitoring cerebral blood oxygenation is not available.

Recently proposed as a technique for tissue characterization and diagnostic imaging, laser optoacoustics combines the merits of optical tomography (high optical contrast) and ultrasound imaging (minimal scattering of optoacoustic waves) to yield a noninvasive diagnostic modality with high contrast, sensitivity and resolution ^[18-44]. This work will concentrate on the determination of hemoglobin saturation in large blood vessels such as the internal jugular vein (IJV). The advantage of the large blood vessel diameter is the quasi plane-layered geometry when probed with an optoacoustic probe with a limited angle of acceptance.

Anatomy and resulting implications for optoacoustic monitoring

The internal jugular vein (IJV) is the only vein that drains cerebral blood. The IJV also drains some blood from the superficial part of the face and the neck (Figure 3). Anatomically, the IJV is a continuation of the transverse sinus, and begins in the posterior compartment of the jugular foramen at the base of the skull. A dilatation in the IJV, called the superior bulb, marks its origin from which it runs down the side of the neck in a vertical direction, initially lying lateral to the internal carotid artery, and then lateral to the common carotid artery. The IJV unites at the root of the neck with the subclavian vein to form the brachiocephalic vein. The left vein is generally smaller than the right, and each contains a pair of valves, which are located about 2.5 cm above the termination of the vessel [⁴⁵].

The jugular veins are ideally suited for measurements with the optoacoustic technique due to their limited depth of roughly 1 cm, their large diameter between 8 and 20 mm and the absence of overlying bone which attenuates and reflects ultrasound. The depth of 1 cm allows sufficient light to penetrate the overlying tissue to generate the US wave in the IJV. The large diameter of the IJV reduces curvature effects and allows the treatment of the IJV as a quasi layered geometry. The absence of bone greatly reduces signal attenuation and artifacts which would occur at alternative sites such as the superior sagittal sinus located within the skull.

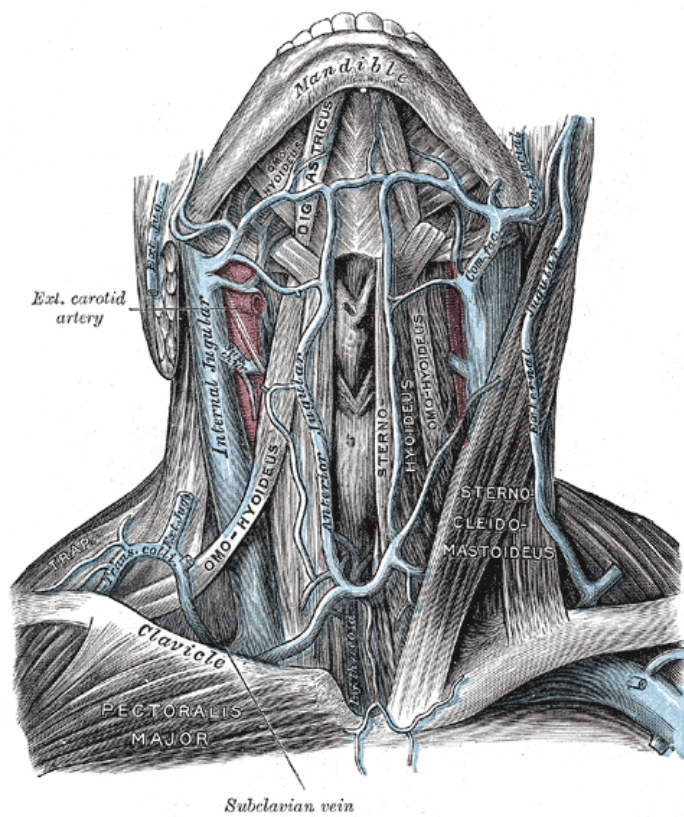


Figure 3: Top: Diagram of the human neck showing the location of internal jugular vein on either side of the neck adjacent to the carotid artery and some of the supplying blood vessels [45]. (This media file is in the public domain in the United States. This applies to U.S. works where the copyright has expired, often because its first publication occurred prior to January 1, 1923). Bottom: Ultrasound Image of the IJV located at a depth of 1 cm with a diameter of 1 cm.

CHAPTER 2: THEORY AND PRINCIPLES OF OPTOACOUSTICS

To obtain more consistent and accurate measurements of the percentage of oxygen-saturated hemoglobin compared to the existing methods, we propose to use the optoacoustic technique for noninvasive continuous monitoring of cerebral SO_2 . Optoacoustic spectroscopy is based on the photo-thermal effect. The oldest technical application of the photo-thermal effect is believed to be the photophone, a communication device invented in 1881 by Alexander Graham Bell. Bell found that audible sound could be heard coming from a tube filled with various materials when the light shining on the transparent tube was modulated by an optical chopper. Modulation of the light shining on an absorbing substance produces a similar modulation in temperature through the photo-thermal effect [46]. The optoacoustic technique is based on the same effect but uses short pulses of monochromatic light (lasers) instead of the modulation of white light.

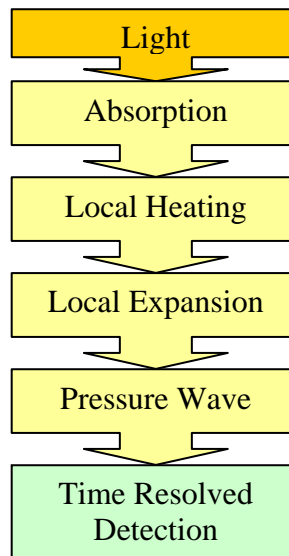


Figure 4: Principles of optoacoustic signal generation.

When a short (nanosecond) laser pulse (Figure 4) irradiates a medium, stress (optoacoustic pressure) is produced upon absorption of the incident energy by the medium. The stress p produced in the medium can be described as:

$$p = \rho_0 c_s^2 \beta \Delta T \quad (1)$$

where ρ_0 [kg/m³] is the density of the medium, c_s [m/s] is the velocity of sound in the medium, β [1/K] is the thermal expansion coefficient, and ΔT [K] is the temperature rise of the medium.

The temperature rise is dependent on the fluence of the laser pulse:

$$\Delta T = \frac{\mu_a F}{\rho_0 c_p} \quad (2)$$

where F [J/m²] is the laser fluence, μ_a [1/m] is the absorption coefficient and c_p [J/kgK] is the heat capacity at a constant pressure. By combining equations (1) and (2) the stress equation becomes:

$$p = \left(\frac{\beta c_s^2}{c_p} \right) \mu_a \cdot F(z) = \Gamma \cdot \mu_a \cdot F(z) \quad (3)$$

where $\Gamma = \frac{\beta c_s^2}{c_p}$ is the Grüneisen parameter. Because the fluence decreases in

the absorbing, non-scattering medium and is given by Beer's Law:

$$F(z) = F_0 \cdot e^{-\mu_a \cdot z} \quad (4)$$

substitution of Eq. (4) into (3) yields the optoacoustic pressure distribution in the medium [47]:

$$p(z) = \Gamma \cdot \mu_a \cdot F_0 e^{-\mu_a \cdot z} \quad (5)$$

The laser-induced stress relaxes during the time it takes for the optoacoustic wave to transit through the heated volume. This time can be estimated as:

$$t_a \propto \frac{1}{\mu_a c_0} \quad (6)$$

If the duration of the laser pulse is significantly shorter than the relaxation time $\tau_L \ll t_a$ (stress-confined radiation conditions), the distribution of the optoacoustic pressure follows the spatial distribution of the heat sources. The thermal relaxation time in the heated volume is much slower and inversely related to thermal diffusivity, χ , as follows :

$$t_\chi \propto \frac{1}{\mu_a^2 \chi} \gg t_a \quad (7)$$

In the case of bulk absorption of light, heat diffusion in the course of the short laser pulses is insignificant [31].

According to Eq. (6), nanosecond laser pulses can be used in many optoacoustic applications. Nanosecond lasers are used in our optoacoustic monitoring systems because the absorption coefficient of the medium can be obtained from the argument of an exponent fitted to the optoacoustic pressure profile induced by the nanosecond pulses.

The refractive index of tissue is higher than that of air. This results in the reflection of light at the air / tissue interface (Fresnel reflection), while the remaining part of the light penetrates into the tissue. Scattering and absorption are responsible for the attenuation of light intensity in the tissue. There are three parameters describing light propagation in tissue: μ_a [1/cm] absorption coefficient, μ_s [1/cm] scattering coefficient, and g [dimensionless] an anisotropy factor that is equal to the average of the cosines of the angles of scattering. When $g = 1$ there is total forward scattering, $g = 0$ at isotropic scattering and $g = -1$ at total backward scattering. If $g \leq 0.1$ and $\mu_s \gg \mu_a$, the effective attenuation coefficient of light in tissue, μ_{eff} , can be calculated from these the parameters [48]:

$$\mu_{eff} = \sqrt{3\mu_a(\mu_a + \mu_s')} \quad (8)$$

where $\mu_s(1-g) = \mu_s'$ is the reduced scattering coefficient. The parameter g is valid only for a single scattering event. In turbid media, such as tissue, there is

multiple scattering. A dimensionless parameter, k , can be introduced in this case. It is dependent on the optical properties of the irradiated tissue.

Therefore, the pressure distribution in tissue can be presented as:

$$\Delta p(z) = \Gamma \cdot \mu_a \cdot k \cdot F_0 e^{-\mu_{\text{eff}} \cdot z} \quad (9)$$

Since z and t are related by

$$z = c_s \cdot t \quad (10)$$

the temporal profile of the optoacoustic pressure signal is presented as:

$$\Delta p(t) = \Gamma \cdot \mu_a \cdot k \cdot F_0 e^{(-\mu_{\text{eff}} \cdot c_s \cdot t)} \quad (11)$$

This relation indicates that the temporal profile of the optoacoustic signal is dependent on the effective attenuation coefficient of the tissue and the speed of sound. The effective attenuation coefficient of blood is dependent on hemoglobin oxygenation. Therefore, the effective attenuation coefficient of the tissue can be obtained from an analysis of the temporal profile of the optoacoustic signal and the hemoglobin oxygenation determined.

This project focuses on: 1) the development of a novel optoacoustic probe, 2) signal processing approaches, and 3) *in vitro* and *in vivo* tests of the optoacoustic system. Improvement in these important areas will advance the optoacoustic monitoring of hemoglobin saturation toward its eventual application in clinical practice.

Optoacoustic Wave Detection: Transmission Mode

In an absorbing medium without scattering, the incident light is exponentially attenuated according to the Beer's law (Figure 5). By placing an acoustic detector on the side of the medium opposite to the irradiated side, an exponential optoacoustic signal can be detected.

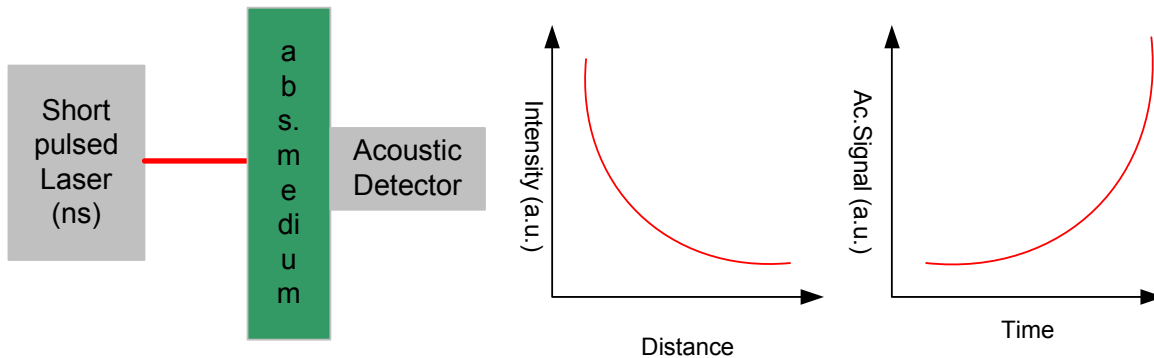


Figure 5: Detection of optoacoustic pulses in transmission mode (left). Intensity distribution in the medium (middle) and resulting optoacoustic signal detected in transmission mode (right).

In a medium with scattering and absorption, the intensity distribution is defined by the absorption and scattering coefficients; therefore, the exponential growth in the optoacoustic signals is dependent on the effective attenuation coefficient.

Additionally, multilayered samples with varying absorbing and scattering properties will result in a complex acoustic signal and modulations at each interface.

Optoacoustic Wave Detection: Reflection Mode

In the reflection mode, irradiation and detection are performed on the same side of the medium. Figure 6 shows an ideal optoacoustic signal measured in the reflection mode. However, the real signals have often a non-exponential shape due to diffraction of optoacoustic waves in the medium caused by edge waves from the perimeter of the excitation beam.

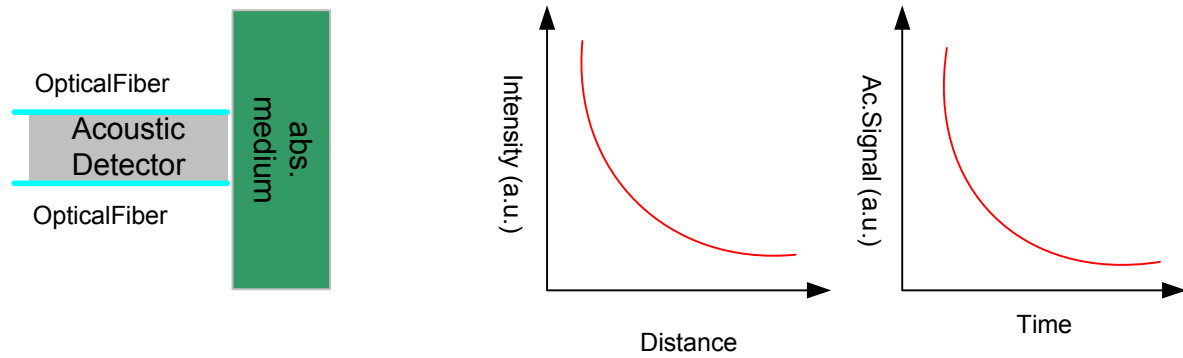


Figure 6: Detection of optoacoustic pulses in reflection mode (left). Intensity distribution in the medium (middle) and resulting optoacoustic signal detected in reflection mode (right).

Optoacoustic Probe

IDEAL OPTOACOUSTIC PROBE

The ideal optoacoustic probe is sensitive, wide-band, free of artifacts, provides symmetrical illumination and is symmetrical in ultrasound reception. Additionally, it should only be sensitive to ultrasound. To achieve these features, thought must be given to specific parameters.

CONSIDERATIONS FOR THE OPTOACOUSTIC PROBE DESIGN

To design and build an optoacoustic probe, shape, bandwidth, sensitivity, electrical matching and acoustic matching must be considered. To respond to the temporal variations in the amplitude of the optoacoustic signal, the detector must have sufficient bandwidth. The necessary bandwidth can be estimated from the attenuation coefficient that we expect to measure. The attenuation coefficient of blood in the near infrared range (700 to 1100 nm) is 5 to 20 cm^{-1} . The stress relaxation time (Equation 6) can be used to estimate the necessary frequency bandwidth to accurately record the wide-band optoacoustic signal. By multiplying the attenuation coefficient by the speed of sound in the medium (1500 m/s), we can calculate the central frequency that is necessary for accurate determination of the attenuation coefficient of blood samples. Table 1 shows the central frequency necessary for the measurement of blood absorption coefficients in the near-infrared range.

Attenuation coefficient (cm ⁻¹)	Central Frequency (MHz)
5	0.75
10	1.5
15	2.25
20	3

Table 1: Central frequency generated in blood with different attenuation coefficients.

The noise level of the presently used preamplifier is 70 μV_{rms} . In order to achieve a signal-to-noise ratio (SNR) of 20 or higher, the optoacoustic signal generated by the piezo-element needs to exceed 700 μV :

$$SNR = 20 \log_{10} \left(\frac{A_0}{A} \right) \quad (12)$$

Estimation of the generated pressure (Equations 4 and 5) yields a pressure change of 100 and 400 Pa for an attenuation coefficient of 5 and 20 cm⁻¹ in the internal jugular vein at a depth of 1 cm and at a fluence determined by the maximal permissible exposure for skin ($MPE_{\text{Skin}} = 20 \text{ mJ/cm}^2 @ 700 \text{ nm}$). Therefore, the sensitivity of our material needs to exceed 0.5 $\mu\text{V}/\text{Pa}$ to achieve a SNR of 20. The use of a piezo-material with even higher sensitivity allows the reduction of laser fluence to levels below the maximal permissible exposure for ocular tissues as well as the use of laser diodes that would substantially reduce the cost, size, and weight of the optoacoustic system.

The sensitivity of a piezo-material is related to the coupling coefficient (k), the acoustic impedance, and the capacitance of the piezo-element. The coupling coefficient is a dimensionless number between 0 and 1 that describes the effectiveness of the conversion of mechanical deformation into electrical energy.

The higher the coupling coefficient, the better is the conversion of mechanical into electrical energy.

In this work we used both PZT and PVDF piezo-material. We selected the piezo ceramic material for its high sensitivity and the PVDF for its close acoustic impedance to tissue. Table 2 shows the coupling coefficients for three commonly used piezo-materials. PZT stands for Lead Zirconate Titanate, a piezo ceramic material, while PVDF stands for PolyVinylidene Fluoride and 1-3 composite is a composite of PZT in an epoxy matrix.

	PZT	PVDF	PZT- epoxy composite
Acoustic impedance (Mray)	33	4.5	8 to 12
Coupling coefficient	0.476	0.2 to 0.3	0.5 to 0.7
Dielectric constant	170	6	200 to 600
Density (g/cm³)	7.5	2	3.5 to 4

Table 2: Comparative chart of the electro-acoustical properties for different piezo-electrical materials [⁴⁹].

The acoustic impedance is another important parameter defined as:

$$Z = \rho v_s \quad (13)$$

where ρ is the density of the medium and v_s is the speed of sound in the medium [⁵⁰].

If an ultrasound wave crosses a boundary between two materials with different acoustic impedances, there will be reflection of the ultrasound wave at the boundary. The fraction of the incident wave intensity in reflected waves can be derived because particle velocity and local particle pressures are required to be continuous across the boundary between materials. Reflectance of an ultrasound wave is described by:

$$R = \left[\frac{Z_1 - Z_2}{Z_1 + Z_2} \right]^2 \quad (14)$$

The capacitance of the piezo-element is important because it determines the voltage signal recorded by the registration system. The higher the capacitance of the material compared to the capacitance of the preamplifier, the greater the generated voltage. The capacitance of the piezoelectric material is determined by:

$$C = \varepsilon \varepsilon_0 \frac{A}{d} \quad (15)$$

where ε is the dielectric constant (Table 1), $\varepsilon_0 = 8.8542 \cdot 10^{-12} \text{ A s V}^{-1} \text{ m}^{-1}$, A is the area of the electrodes and d is the distance between the electrodes [51]. A piezo-element with a larger area is capable of generating a signal of greater amplitude for a given pressure wave.

A matching of acoustic impedance between backing material and piezo-element is crucial because any mismatch will lead to reflections of the ultrasound waves and will increase the artifacts of the system [52].

CHAPTER 3: EXPERIMENTAL SETUP

The optoacoustic setup consisted of a pulsed laser system with pulse duration of 5 ns. The system included either a Nd:YAG laser (Ultra CFR, Big Sky Technologies, Inc., Bozeman, MT) at a wavelength 1064 nm with a pulse duration of 5 ns or a tunable Optical Parametric Oscillator (OPO) (Opolette 532 II, Opotek Inc., Carlsbad, CA) with a wavelength range between 690 to 2400 nm and a pulse duration of 5 ns. The OPO output power was wavelength-dependent (Figure 7). The laser pulse was then coupled into an optical fiber, which directed the light to the optoacoustic probe. The optoacoustic probe was varied throughout the experiments. The optoacoustic signal collected from the probe was then amplified using pre- and secondary amplifiers and then acquired with a 2 Channel 100 MHz digitizer (NI 5112, National Instruments Corp., Austin, TX) and stored on the laptop computer using a LabView program developed in our laboratory.

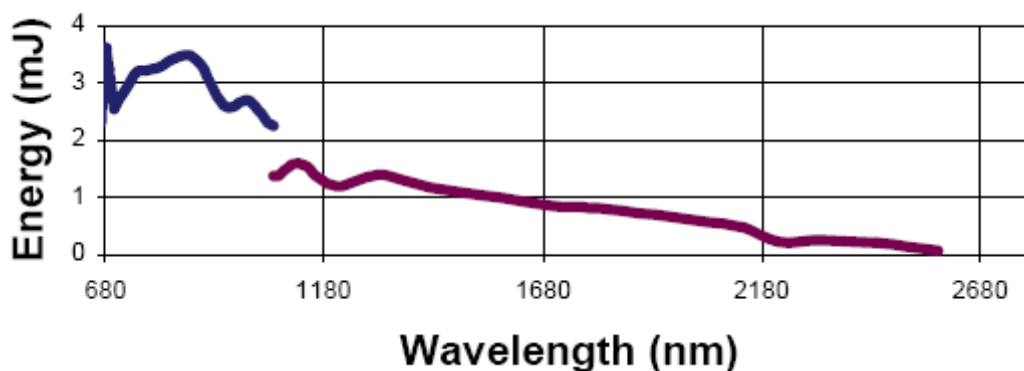


Figure 7: Tuning Curve Opolette 532 Type II as stated from the manufacturer.

Figure 8 shows a diagram of the setup for *in vivo* studies.

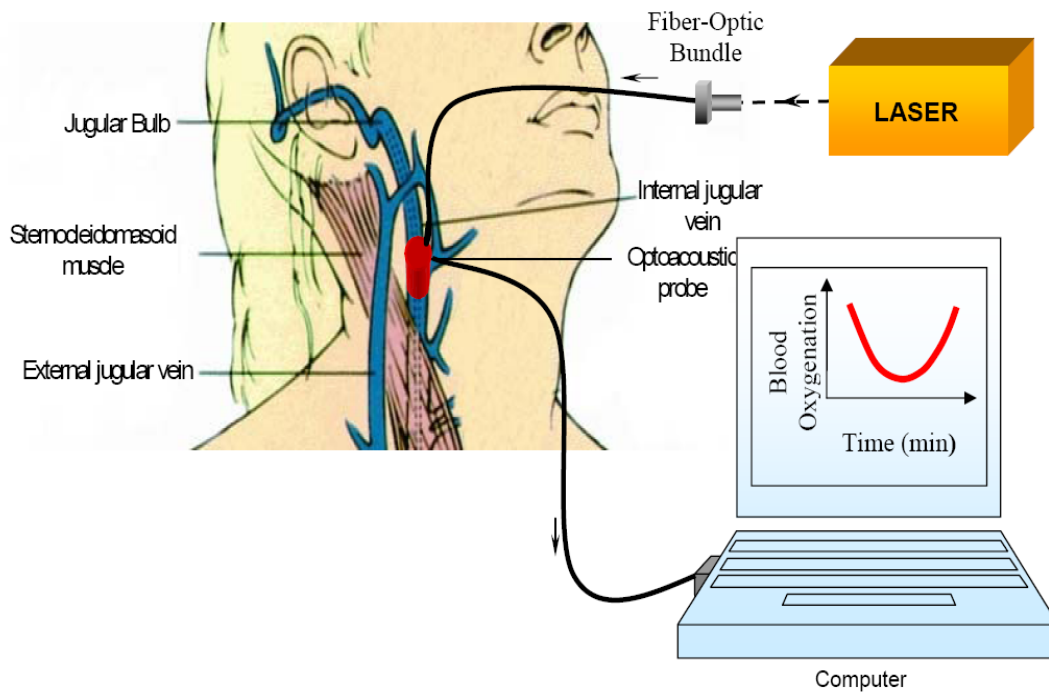


Figure 8: Optoacoustic setup for *in vivo* studies showing laser system, optoacoustic probe, measurement location and underlying anatomy, and the data collection system of the signals

The preamplifier used in our system was a 17 dB low-noise hydrophone preamplifier (Specialty Engineering Associates, AH-17DB) which was powered by batteries to reduce noise. The nominal voltage gain was 17 dB into 50 Ω . The input impedance was 1 M Ω in parallel with a capacitance of 20 pF. Figure 9 shows the gain plot of the preamplifier as stated from the manufacturer.

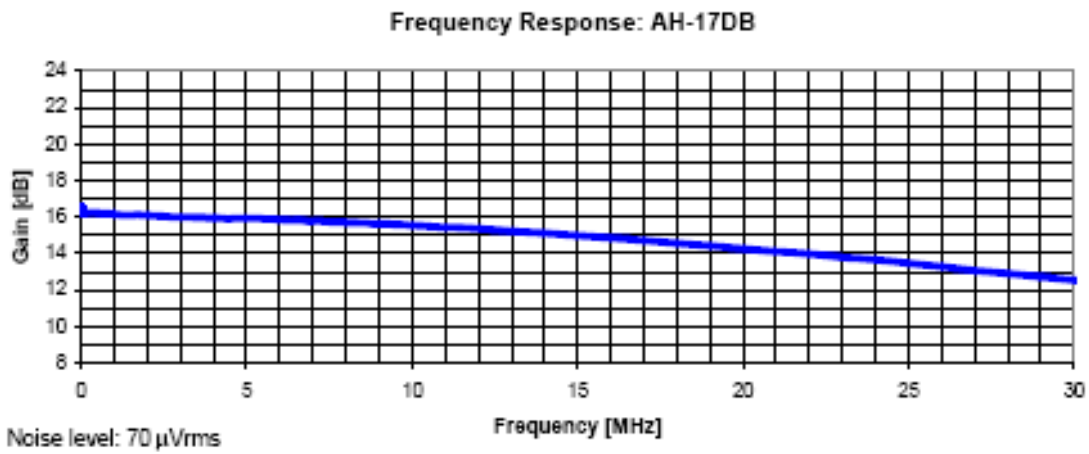


Figure 9: Typical gain plot of the AH-17PD amplifier.

The frequency range of the preamplifier was from 5 kHz to 25 MHz [53].

The secondary amplifier was a bipolar low noise amplifier (Model 322, Analog Modules, Inc. Longwood, FL) which was powered by a bench-top power supply. The nominal voltage gain was 40 dB with a bandwidth from 100 Hz to 10 MHz. The input and output impedance was 50 Ω . The noise was 280 pV/ $\sqrt{\text{Hz}}$.

CHAPTER 4: PIEZOCERAMIC PROBE DESIGN AND RATIONALE AND TEST

In this work we used piezo ceramic as the piezoelectric materials for the transducer. We chose the piezo ceramic material for its high sensitivity. Our presently used piezo ceramic element has a sensitivity of 200 $\mu\text{V}/\text{Pa}$ which provided a SNR ratio of 86 at MPE_{Skin} fluence levels for an attenuation coefficient of 20 cm^{-1} .

The dimension of the piezo-element was 3 mm x 3 mm with a thickness of 1 mm. The central frequency for the piezo-element was calculated by:

$$F_{\text{central}} = \frac{C_s}{2 \cdot d_{\text{piezo}}}, \quad (16)$$

where F_{central} is the central frequency, C_s is the speed of sound through the piezo-element (4165 m/s), and d_{piezo} is the thickness of the piezo-element. The calculated central frequency for the piezo-element was 2 MHz.

The ground electrode was soldered to a brass housing which also housed four 1-mm optical fibers that encircled the piezo-element. These fibers were glued with a special fiber epoxy (Thorlabs, Inc.). The signal from the piezo-element was amplified with a 17 dB low-noise hydrophone preamplifier (Specialty Engineering Associates, AH-17DB) which was powered by batteries to reduce noise. The frequency range of the preamplifier was from 5 kHz to 25 MHz [⁵³].

The probe had an aluminum housing to provide electrical shielding. The piezo-element was also electrically shielded with 5- μm thin aluminum foil. Figure 10 shows a schematic diagram of the probe.

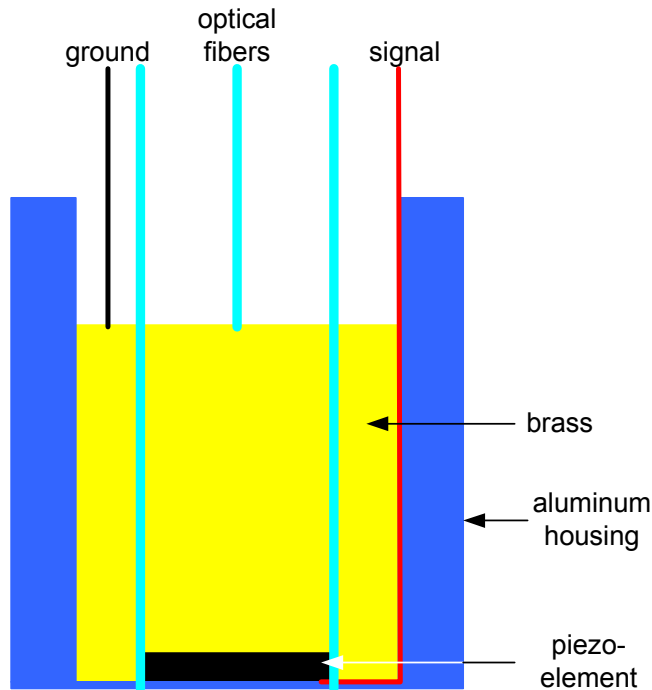


Figure 10: Schematic representation of the piezo ceramic optoacoustic probe.

Current medical single-frequency ultrasound devices work by using a narrow-frequency bandwidth and an index matching layer between the transducer element and the tissue. To prevent reflection, these layers must have a thickness corresponding to half the ultrasound wavelength similar to anti-reflection coatings for optics. Due to the wide bandwidth of the optoacoustic signal, these layers are not useful. An impedance matching layer would produce reflections and noise associated with the reflections of other frequencies that are not matched. Instead, we used a silicone spacer between the skin and the probe which allowed for temporal separation of the unwanted optoacoustic signal generated in the transducer from the optoacoustic signal generated in tissues.

Probe Test

Table 1 shows the central frequencies necessary for the accurate recording of the optoacoustic signals. Our optoacoustic probe required sufficient bandwidth to faithfully record the optoacoustic signals generated in our experiments. Figure 11a shows two square pulses with different pulse widths. Figure 11b shows the corresponding power spectrum of the wide pulse, while Figure 11c shows the corresponding power spectrum of the narrow pulse.

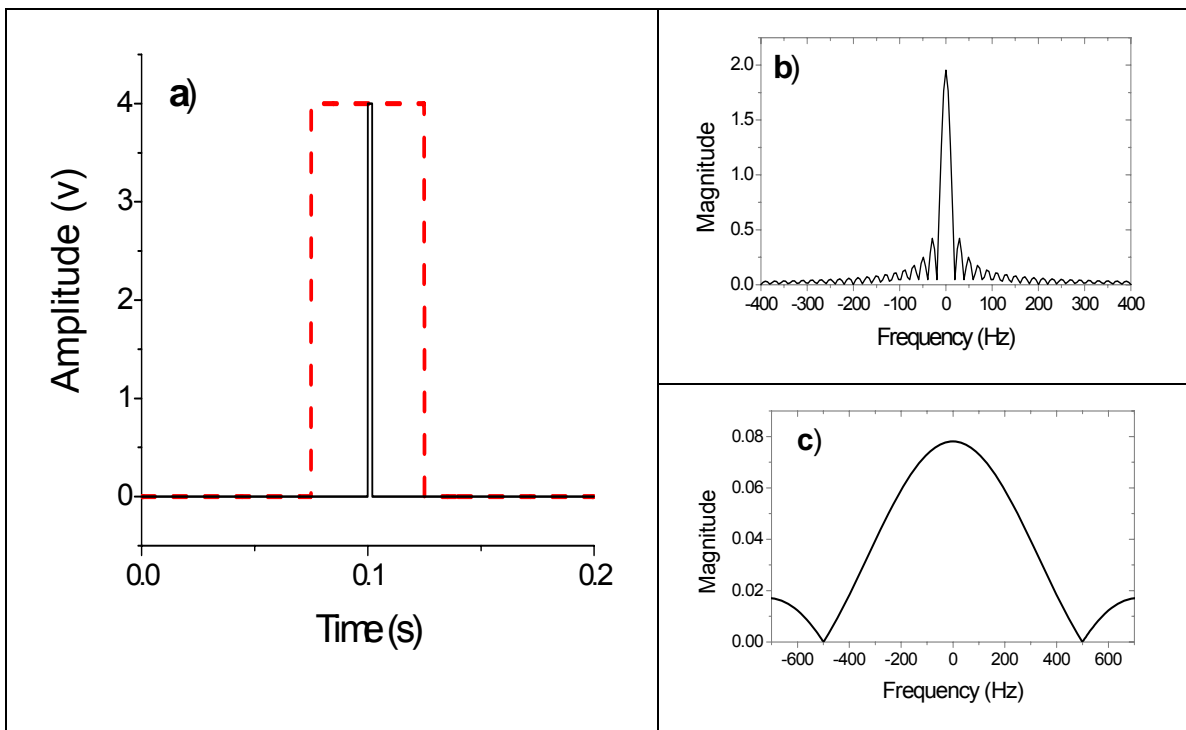


Figure 11: Two square pulses with different pulse widths (a) and corresponding power spectrum of the wide (b) and narrow (c) pulse.

Figure 11 shows that a shorter pulse generates a wider bandwidth in the power spectrum. It is possible to apply a very short pulse to generate a signal

that contains all frequencies at the same amplitude (area between 0 and 50 Hz in Figure 10c).

The frequency response of the optoacoustic probe was tested in the transmission mode (Figure 5). To determine the bandwidth of the piezo ceramic probe, we applied a very short pulse to the piezo-element. A 1-cm thick quartz glass plate was used as the hard boundary. The quartz plate facing the laser beam ensured that the signal had no negative part due to decompression at a soft boundary. A 2-mm thick black rubber layer with a very high absorption coefficient was used to generate the pulse. Acoustic contact was maintained with ultrasound gel. The laser pulse at 1064 nm from the Nd:YAG laser was expanded to 4 cm to prevent diffraction of the resulting ultrasound wave due to edge effects. Figure 12 shows the resulting signal of the short pulse measured with the piezo ceramic transducer. The signal shown is an average over 300 signals.

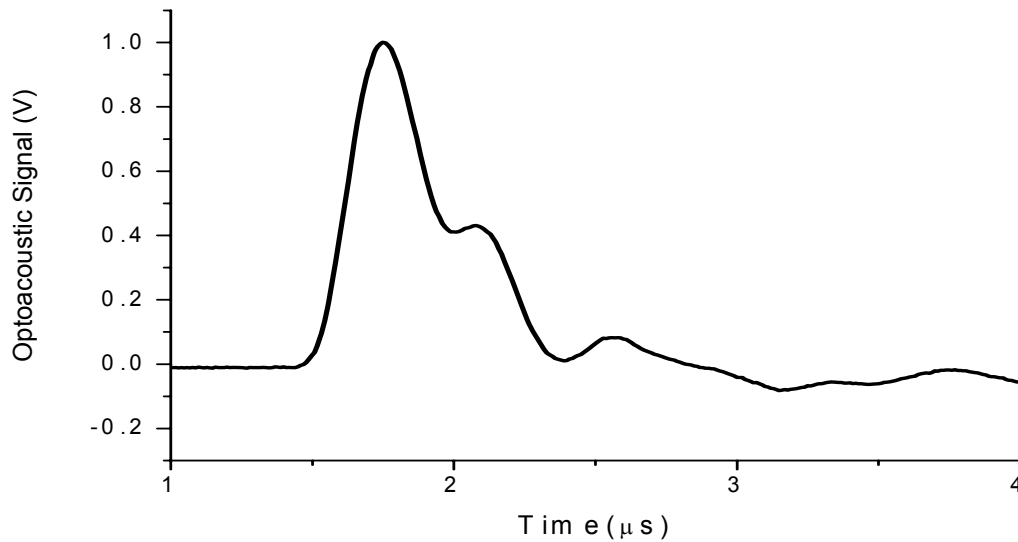


Figure 12: Optoacoustic signal derived from 2-mm thick black rubber with ultra high absorption coefficient.

The impulse response of our optoacoustic probe showed some ringing with a distance between peaks of $0.5 \mu\text{s}$. This delay corresponded to the 2 MHz center frequency of our piezo ceramic material.

Using a Fourier transform, we derived the power spectrum of the signal and determined the frequency response of our optoacoustic probe (Figure 13). The power spectrum resulted in a bandwidth of 3.6 MHz at full width half maximum (FWHM). This bandwidth should be sufficient enough to accurately record the optoacoustic signals generated in our experiments.

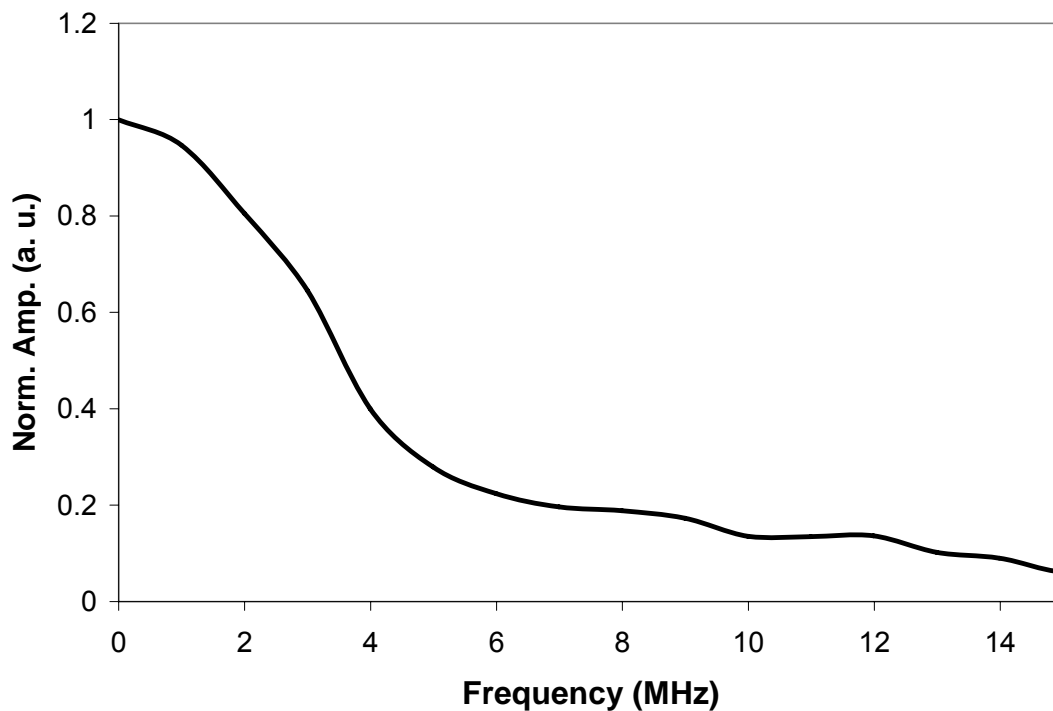


Figure 13: Voltage spectrum of optoacoustic signal derived from 2-mm thick black rubber with ultra high absorption coefficient.

CHAPTER 5: PHANTOM STUDIES WITH THE PIEZOCERAMIC PROBE

The piezo ceramic probe was tested in a crude model to measure the signal from an absorbing media that represents blood through a scattering layer. The model was not an accurate representation of the anatomy of the internal jugular vein.

A non-absorbing plastic tube with a diameter of 1 cm and a length of 3 cm was closed at one end and glued upright on the bottom of a plastic cup. The diameter of the plastic cup was 6 cm. The function of the plastic tube was to contain each of the absorbing naphthol green solutions used as a phantom for blood. This bottomless design prevented reflections due to acoustic impedance mismatch between the solutions and the plastic boundaries. With a naphthol green solution with an absorption coefficient of 10 cm^{-1} , the bulk of the light was absorbed in the first few millimeters and the remainder of the absorbing medium did not take part in the signal generation, whereas the reflections of the ultrasound waves at the boundary could create artifacts. Small rubber tubes were connected to the larger plastic tube to allow the replacement of the absorbing solution that simulated blood in the jugular vein phantom. After assuring the plastic tube was impermeable, it was filled with an absorbing solution (naphthol green adjusted to 10 cm^{-1} at 1064 nm), while the remaining volume of the plastic cup was filled with diluted milk [one part of whole milk (3.5%) and five parts of water] to simulate turbid tissues (with $\mu_{\text{eff}} = 1 \text{ cm}^{-1}$) between the probe and the absorbing medium (Figure 14). The laser used in the phantom experiments was the Nd:YAG laser.

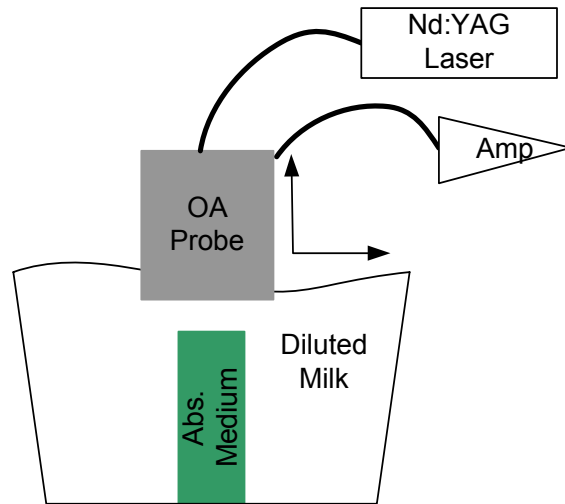


Figure 14: Schematic representation of the experiment with the jugular vein phantom.

In the first experiment the probe was moved vertically away from the phantom (Figure 15). As a result, the signal generated by the jugular phantom shifted further in time with distance. This vertical movement allowed the detection of the signal generated in the absorbing medium. Figure 15 shows the unwanted signal generated by electromagnetic noise induced by the laser power supply, and the optoacoustic signal induced in the probe due to light reflection back into the probe. To separate this part of the signal from the signal generated in the probed area, we introduced the silicone spacer, which was placed between the probe and the skin in the sheep experiments.

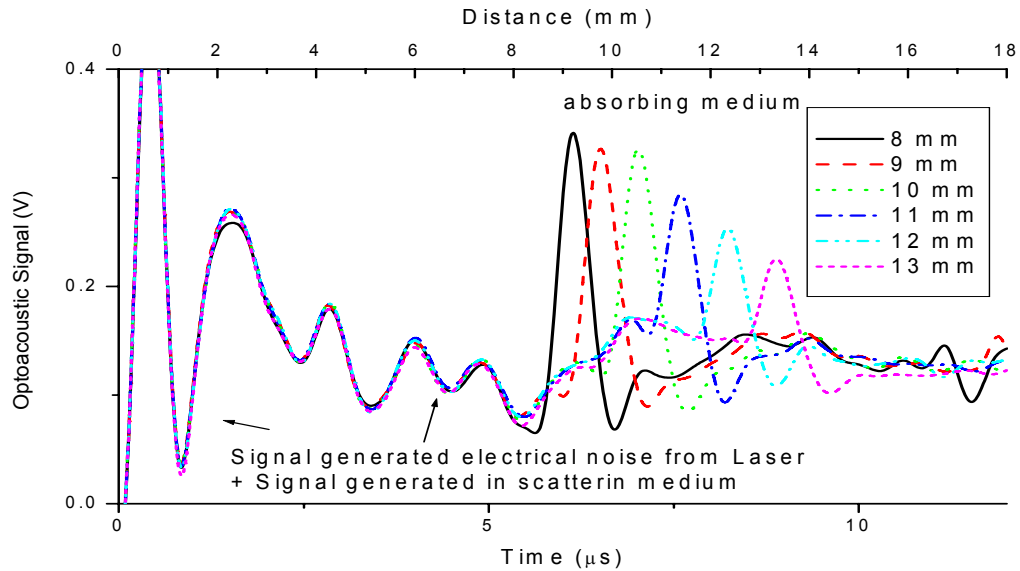


Figure 15: Signal from the probe at various vertical displacements. The energy used was $25 \mu\text{J}$ and the absorption coefficient of the solution was 15 cm^{-1} . The arrows indicate the unwanted signal.

We also performed experiments with lateral displacements to test the stability of the optoacoustic signals measured with the new probe. Figure 16 shows the section of the optoacoustic signal from the absorbing medium. The signal decreased with displacement until it was no longer detectable at 10-mm lateral displacement. The graph shows only the signals between 0 and 5 mm displacement. In addition to a reduction in signal amplitude with increasing probe-vein displacement, there is an increasing temporal delay due to the greater distance between probe and absorbing medium. Additionally ringing was detected as previously detected in the impulse response (Figure 12). The temporal delay between peaks was $1 \mu\text{s}$ which is 1 MHz, half the center frequency of the piezo ceramic material used in the transducer. However, this ringing did not seem to affect the amplitude measurements.

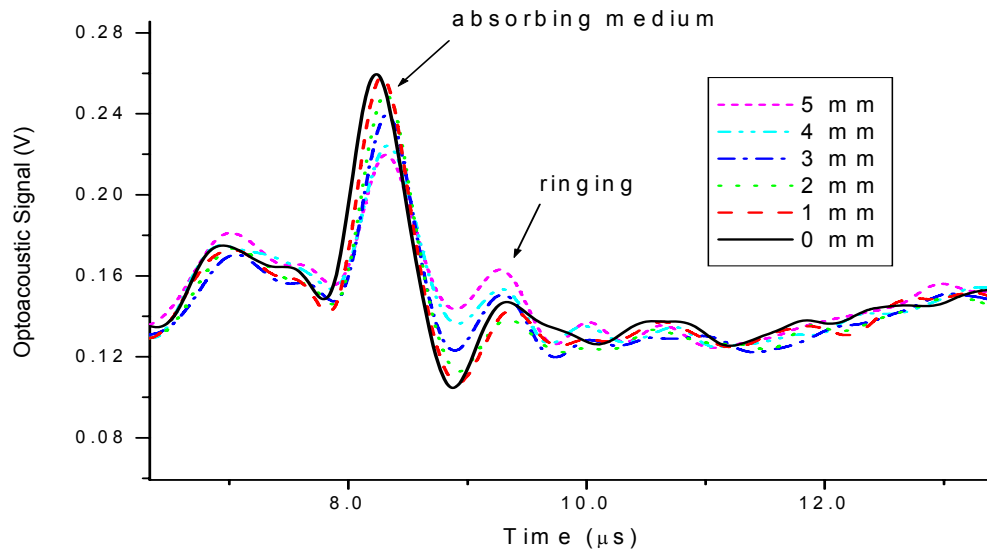


Figure 16: Optoacoustic signal recorded from the jugular vein phantom at various lateral displacements. The vertical distance between the probe and the phantom was 12 mm. The energy of the laser pulses was $25 \mu\text{J}$ and the absorption coefficient of the solution was 15 cm^{-1} .

The phantom studies showed that our optoacoustic probe was capable of detecting optoacoustic signals from an absorbing medium at depths up to 13 mm and beyond. The effect of lateral misalignment between probe and phantom was determined and the influence of the electrical impulse generated by the firing of the laser and its avoidance were studied.

CHAPTER 6: *IN VIVO* STUDIES OF THE PIEZO CERAMIC PROBE WITH SHEEP

The Institutional Animal Care and Use Committee at The University of Texas Medical Branch (UTMB) approved all procedures performed with sheep, which were ordered by and subsequently housed at the Animal Resources Center at UTMB. All facilities are staffed by full-time veterinarians who monitored the humane care of each animal. All catheterizations and surgical procedures were performed under general anesthesia closely monitored by a veterinarian to minimize discomfort and ensure safety for the animals. The sheep were initially sedated with ketamine. Once sedated, isoflurane was used for deep anesthesia. All animals were intubated and mechanically ventilated with a mixture of isoflurane in oxygen. An electrocardiogram was used to monitor the sheep continuously throughout the procedure. The head of each sheep was stabilized to minimize movement that could alter the signal.

For the sheep studies we used the OPO to generate laser pulsed at different wavelengths. The optoacoustic probe was attached to the surface of the sheep skin overlying the external jugular vein (EJV). The position could be varied using a 3-D translation stage. The best position was determined by adjusting the probe to the position where the optoacoustic signal reached the maximal amplitude at 800 nm assuming that the optoacoustic signal amplitude reaches a maximal value at best probe-vein alignment. We choose to use 800 nm for alignment due to the high laser output power of the OPO at this wavelength. Additionally, the optoacoustic signal induced at a wavelength of 800 nm is independent of blood oxygenation. The acoustic contact was provided by ultrasound gel (Aquasonic 100: Parker Laboratories Inc.).

A series of measurements were performed on the EJV of four adult sheep. The measurements were taken at 3 wavelengths: 700, 800, and 1064 nm. At 700 nm the effective attenuation coefficient of blood increases with a decrease in blood oxygenation; therefore, the optoacoustic signal amplitude is expected to rise. While at 1064 nm, the effective attenuation coefficient is decreasing therefore decreasing the optoacoustic signal amplitude. Measurement at the isosbestic point can be used for calibration and normalization for changes in laser output power and total hemoglobin concentration. To minimize the influence of electronic noise and possible motion artifacts on the results, 400 signals were averaged for every record, requiring about 20 seconds. Four hundred signals were more than enough for signal averaging, and the 20-s duration was long enough to allow measurement during at least one full circulatory and respiratory cycle, while still being short enough for the level of blood oxygenation to remain stable. The whole set of measurements at three wavelengths required less than 3 minutes. The laser fluence at the site of probing was well below the Maximal Permissible Exposure (MPE) for skin in the specified spectral range. The maximal permissible exposure for skin is 20 mJ/cm² for the visible range and 100 mJ/cm² at 1064 nm [54,55]. The average laser energy out of our optical probe was 99 μJ at 700 nm, 97 μJ at 800 nm and 64 μJ at 1064 nm. The spot size of the laser beam was expanded to 1 cm after passing through the silicone spacer.

Blood oxygenation in the EJV was changed by varying the fraction of inspired oxygen (FiO₂) by substituting oxygen with nitrogen. We performed 2 cycles on a total of 4 sheep. In each cycle, blood oxygenation was reduced to approximately 20% and then increased to within the normal range again. The sheep was allowed to rest for about 45 minutes to allow time for reversal of circulatory changes, such as intravascular volume shifts and vasoconstriction,

that might occur secondary to hypoxemia. Then the optoacoustic probe was readjusted to the maximal signal amplitude at 800 nm before completing the second cycle.

The oxygenation of arterial blood was monitored by a pulse-oximeter, (which provided real-time assessment of the change in oxygen level during the experiment) attached to the tongue of the sheep. Accurate measurements of the jugular SO_2 were performed with the CO-Oximeter (IL 813 Instrumentation Laboratories, Lexington, MA) by taking blood samples from the catheter inserted in the EJV. Figure 17 shows typical averaged optoacoustic signals from the EJV generated from laser light pulses at three different wavelengths (700, 800, and 1064 nm) at three different levels of blood oxygenation. The first peak represents the signal induced in skin. The time delay that resulted from the use of the silicon spacer, which separated the optoacoustic signal from the electric noise generated by the laser power supply, was removed from the graph.

With a decrease in blood oxygenation, an increase in the amplitude of the optoacoustic signal at 700 nm was detected while the signal amplitude at 1064 nm decreased. The signals at 800 nm were supposed to be independent of oxygenation, but were changing due to changes in the incident laser power. Note that the laser energy used for the excitation of the optoacoustic signals was wavelength dependent (Figure 7). Therefore, the relative optoacoustic signal amplitudes at one level of blood oxygenation did not correlate with variation of the effective attenuation coefficient alone but with incident laser energy as well. However, the relative changes at various blood oxygenations at one wavelength did correlate with changes in the effective attenuation coefficients. Additionally the laser energy output of the OPO was not stable throughout the experiment due to heating of the OPO and was not monitored throughout the experiments.

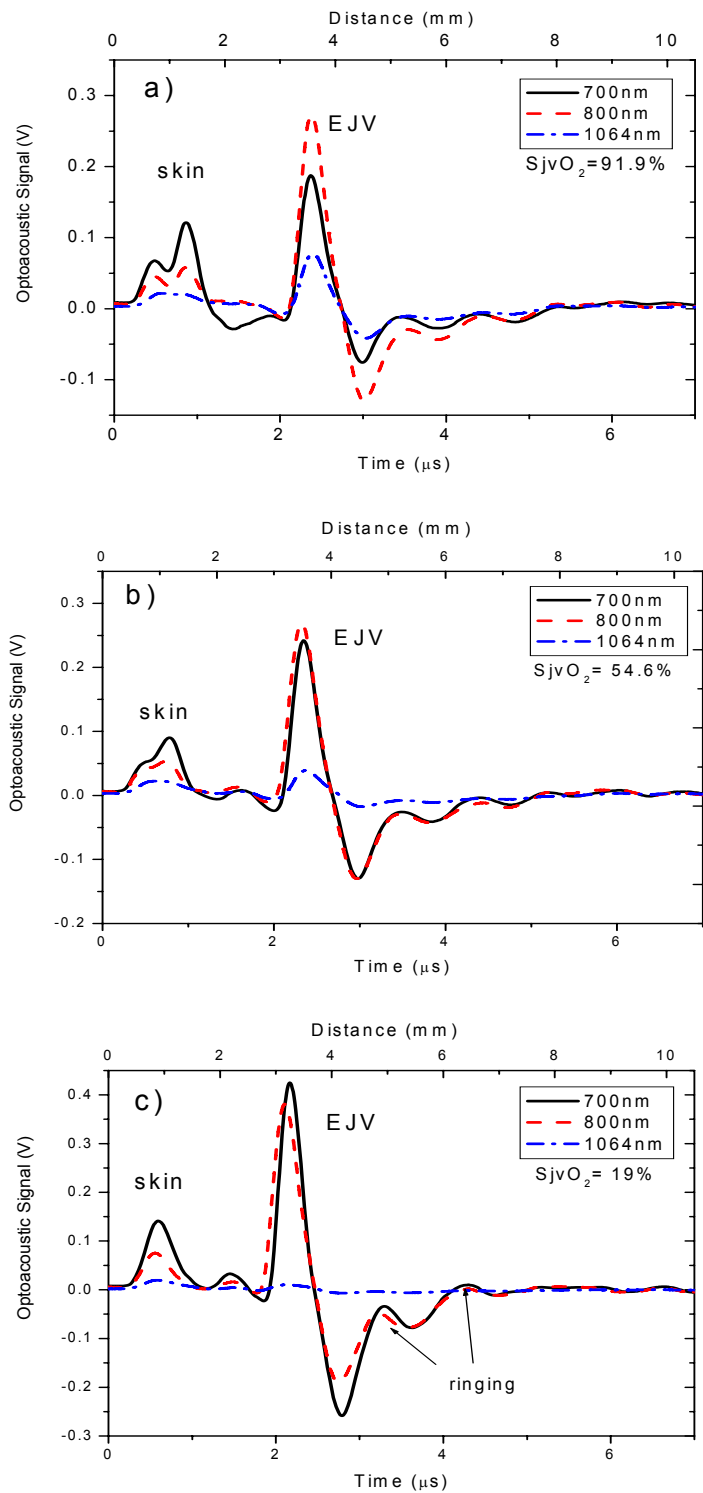


Figure 17: Optoacoustic signals generated at 700, 800, and 1064 nm at blood oxygenations of (a) 91.9%, (b) 54.6%, and (c) 19% [56].

The optoacoustic signals generated in the EJV showed ringing in the tail of the bipolar signal where a monotonic decay was expected. This ringing had a frequency of 1 MHz and was inherent to the probe. It was also detectable in the delta signal generated for the determination of the frequency response (Figure 11) and in the phantom experiments (Figure 15). The time interval was about 1 μ s which corresponded to the thickness of the piezo ceramic crystal.

Figure 18 shows the time course of the optoacoustic signal and the blood oxygenation for one exemplary sheep. The remaining graphs of the other sheep are located in the appendix (Figure 69). Variation of the FiO_2 resulted in changes in the level of blood oxygenation in the EJV and in the optoacoustic signals at 700 and 1064 nm. The optoacoustic signal amplitude at 700 nm (filled circles) rose with a decrease in blood oxygenation (black squares) while the optoacoustic signal amplitude followed blood oxygenation at 1064 nm (red triangles). We performed 2 cycles in which we reduced the level of blood oxygenation and then increased it again. A recovery time for the sheep was included in between the cycles.

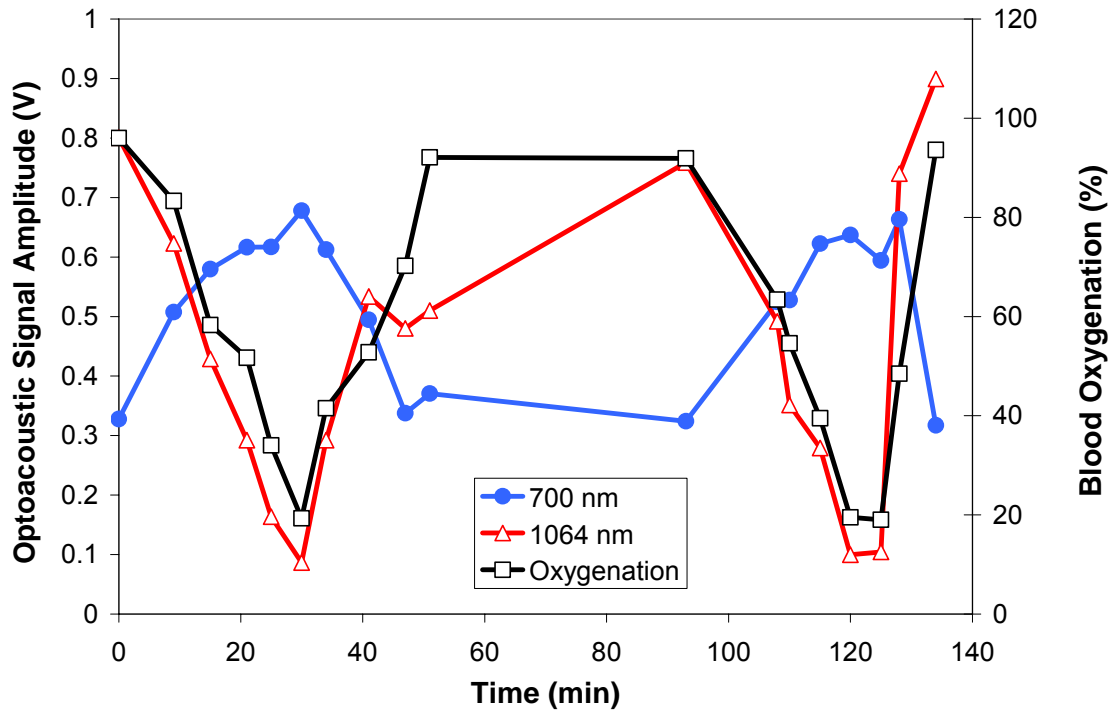


Figure 18: Time course of blood oxygenation (black squares) and optoacoustic signal amplitudes at 700 nm (blue filled circles) and 1064 nm (red triangles).

Figure 19 shows the dependence of the optoacoustic signal amplitudes on the $S_{jv}O_2$ obtained from the sheep for both cycles, the first cycle on top and the second cycle at the bottom for one exemplary sheep. The remaining graphs of the other sheep are located in the appendix (Figure 70). The optoacoustic signal amplitudes were normalized using the signal generated at 800 nm to adjust for changes in laser output power due to heating of the OPO.

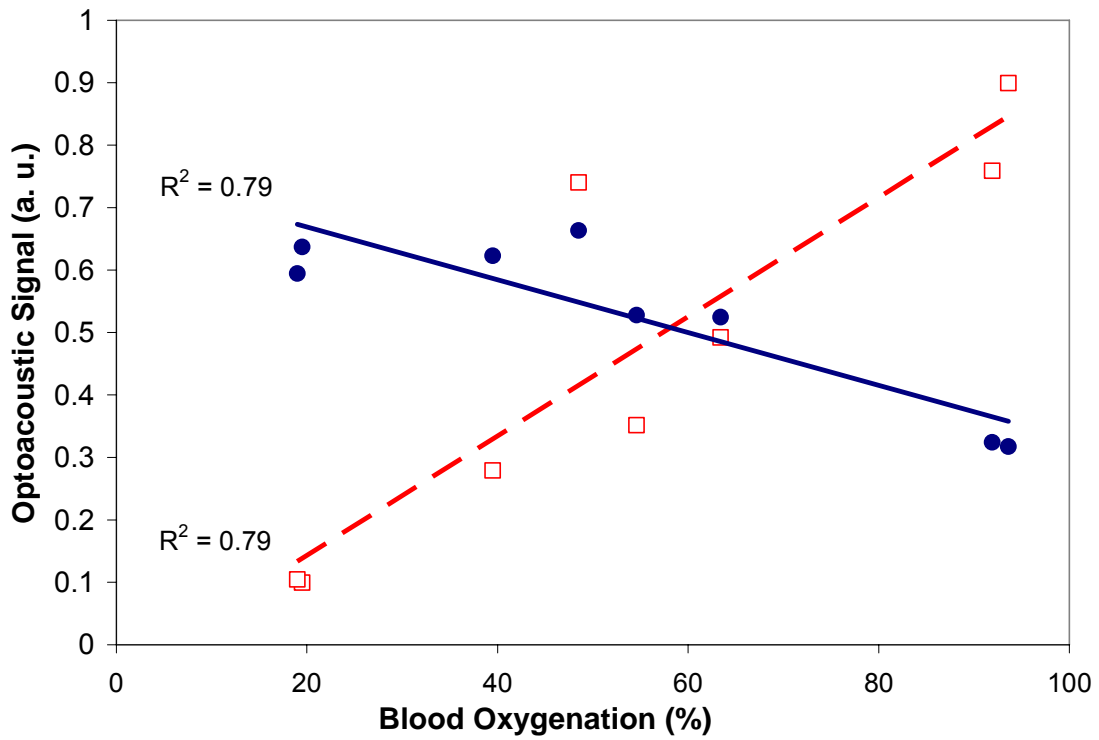
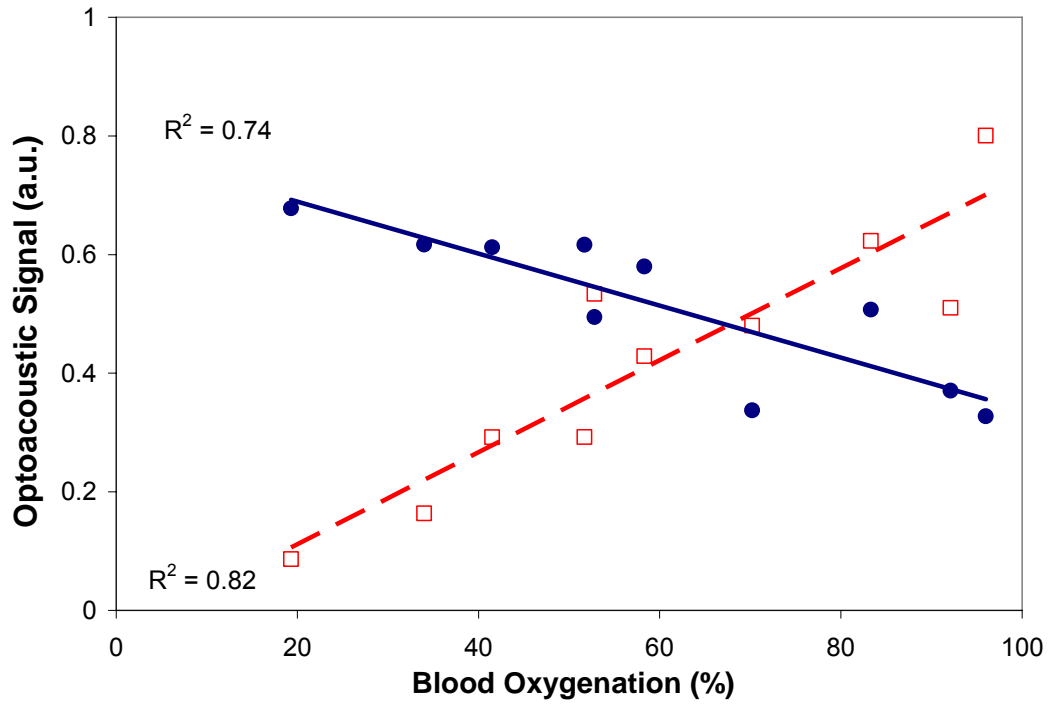


Figure 19: Optoacoustic signal amplitudes at 700 nm (blue filled circles) and 1064 nm (red squares) normalized to the signal amplitude at 805 nm.

These measurements showed a correlation between the optoacoustic signal amplitude and the blood oxygenation in the EJV and indicated a good repeatability of the experiment within one subject. However, the amplitudes of the optoacoustic signals did not allow for a universal calibration. The optoacoustic signal amplitudes were dependent on the effective attenuation coefficient and the laser fluence reaching the blood vessel. The laser fluence varied between subjects due to differences in location and depth of the blood vessel, variation in the tissue overlying the blood vessel, and blood vessel diameter. The correlation between amplitude and SO_2 would have to be established for every test subject and alignment. Therefore, monitoring blood oxygenation using the amplitude measurements alone would not be practical. A new algorithm needs to be established that is less dependent on fluence and alignment. We analyzed the temporal profile of the optoacoustic signals to determine blood oxygenation. We used the decay of the bipolar signal to extract information on blood oxygenation. Karabutov et al proposed that with excitation using a small diameter laser beam with a Gaussian intensity distribution, the decay of the resulting bipolar optoacoustic signal correlates to the optical properties of the irradiated medium [⁵⁷]. The algorithm was described in a prior publication of our group [⁵⁸]. Briefly, the minimal value of the optoacoustic signal generated in the EJV was selected and then normalized to 1. To reduce the effect of internal oscillations in the piezo-element, the signal was integrated starting from the normalized minimum. Then the value of the integral was determined within the first 3 μ s. The 3- μ s delay allowed for the dampening of the signal and (multiplied by the speed of sound in soft tissue of 1500 m/s) correlated to a depth of 4.5 mm into the EJV.

Figure 20 shows a diagram of the data processing algorithm. The shaded area represents the area of the integral.

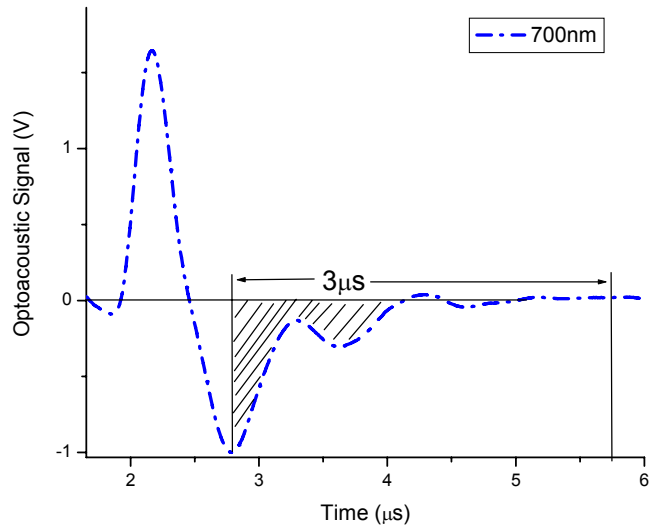


Figure 20: Diagram of the data processing algorithm.

The idea behind this data processing algorithm is that with an increase in the effective attenuation coefficient the laser light is absorbed faster. This should lead to an increased decay of our optoacoustic signal and a reduction in the value of the integral between the normalized minima and the $3 \mu\text{s} / 4.5 \text{ mm}$ delay.

Figure 21 shows the time course of the inverse integral calculated with this algorithm for one exemplary sheep. The remaining graphs of the other sheep are located in the appendix (Figure 71).

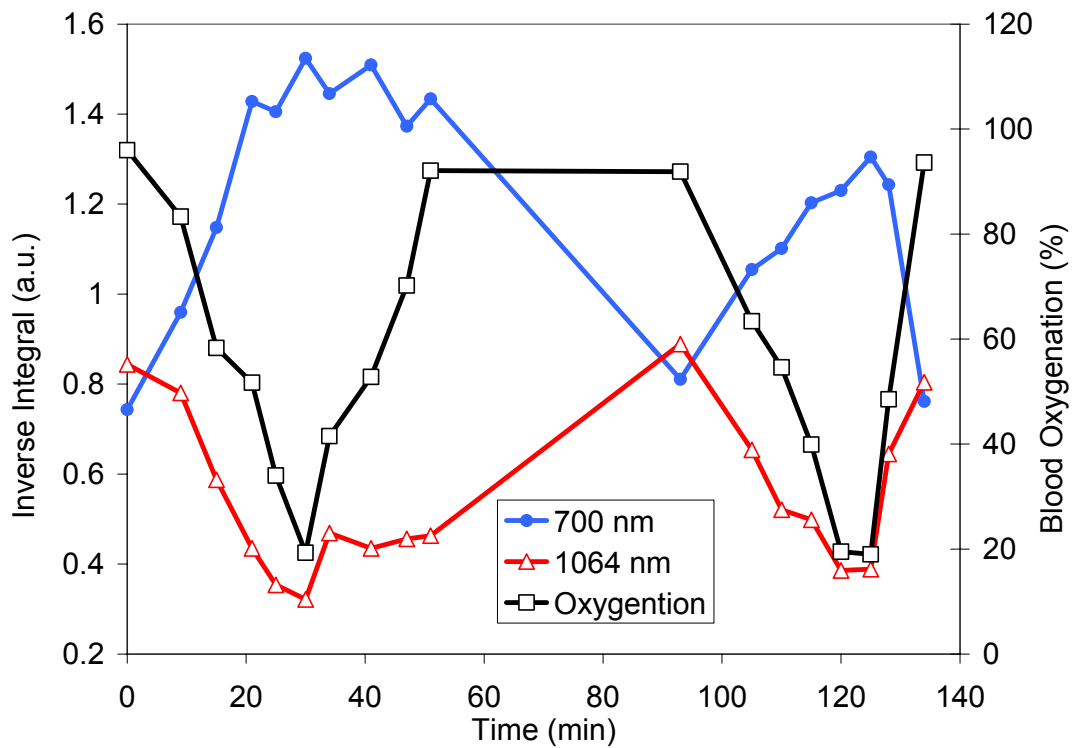


Figure 21: Time course of blood oxygenation (black squares), and integrated optoacoustic signals for 700 nm (blue filled circles) and 1064 nm (red triangles).

To eliminate the influence of total hemoglobin (tHb) variation, the values of the inverse integral were divided by the values of the inverse integral obtained at 800 nm. Total hemoglobin levels changed due to the stress induced in the sheep due to low levels of blood oxygenation. Total hemoglobin levels rose after low levels of blood oxygenation leading to an increase in signal at all wavelengths.

Figure 22 shows the correlation obtained for 700 nm and 1064 nm with blood oxygenation for one exemplary sheep. The remaining graphs of the other sheep are located in the appendix (Figure 72).

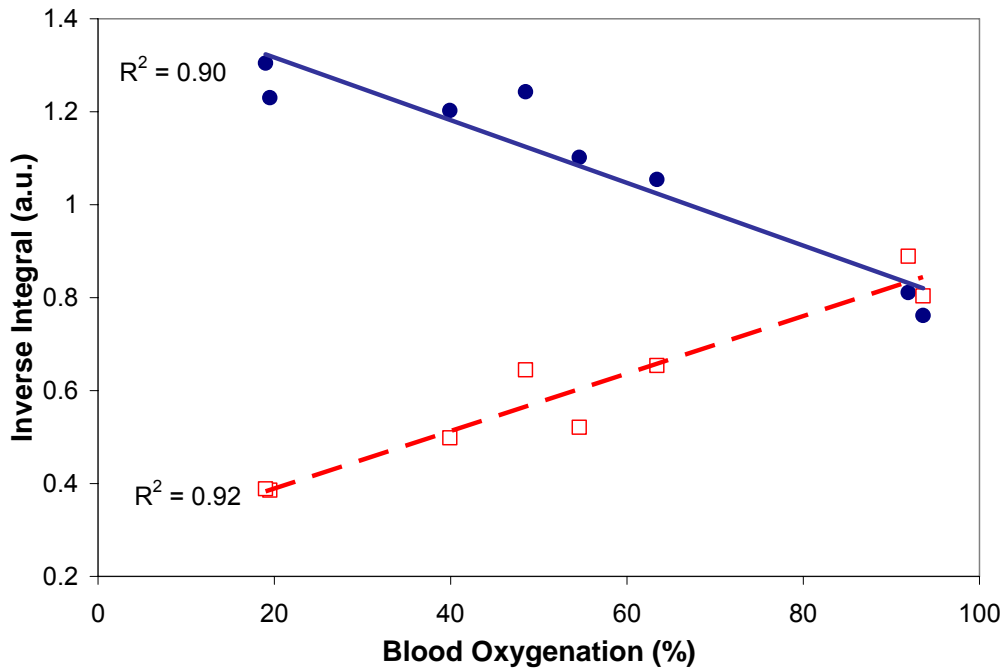
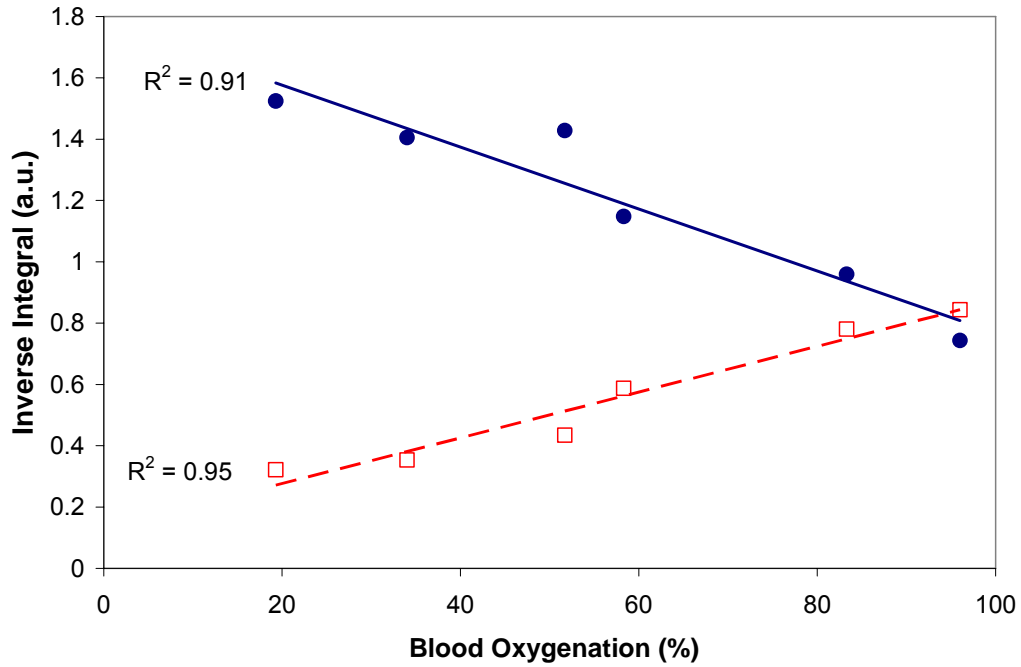


Figure 22: Correlation of temporal inverse integral ratio with blood oxygenation at 700 nm (blue filled circles) and 1064 nm (red squares) (the first cycle appears at the top of the graph while the second cycle appears at the bottom).

By dividing the values shown in Figure 22 with each other, we determined the ratio between the temporal profiles at 700 nm and 1064 nm (Figure 23). This ratio closely followed the ratio of the computationally determined effective attenuation coefficients using Monte Carlo simulation for a cylindrical geometry obtained by Dr. Igor Patrikeev.

To obtain the theoretical values we modeled optoacoustic signals generated by light with 700 nm and 1064 nm for planar geometry with an embedded cylindrical object. We used our Monte Carlo code described in previous work [42]. We assumed that the vessel had a diameter of 8 mm (a typical value for sheep EJV) and was located 3 mm below the skin. To estimate the influence of blood oxygenation, we varied the percentage of oxyhemoglobin from 10% to 90%. The absorption coefficients for each wavelength were calculated from literature data [59] by linear interpolation of molar extinction coefficients of oxyhemoglobin and deoxyhemoglobin. The scattering coefficients were found using the effective attenuation coefficient measured in vitro [60]. The anisotropy factor g was considered constant ($g=0.99$) for both of the wavelengths [61,62]. We held the optical properties of the ambient medium constant as at any of the chosen wavelengths the tissue surrounding the IJV is low absorbing compared to blood, and its influence on the signal is negligible. We did not model photon traces in the skin, but the role of skin as a light diffuser was taken into account. The vessel wall was not included in the model due to its minimal thickness compared to EJV diameter.

The modeled signals were processed with the same algorithm that was applied to the *in vivo* sheep data (Figure 20). Results are presented in Figure 23 [59]. Figure 23 shows the ratio obtained for 700 nm and 1064 nm versus blood oxygenation for one exemplary sheep. The remaining graphs for the other sheep are located in the appendix (Figure 73).

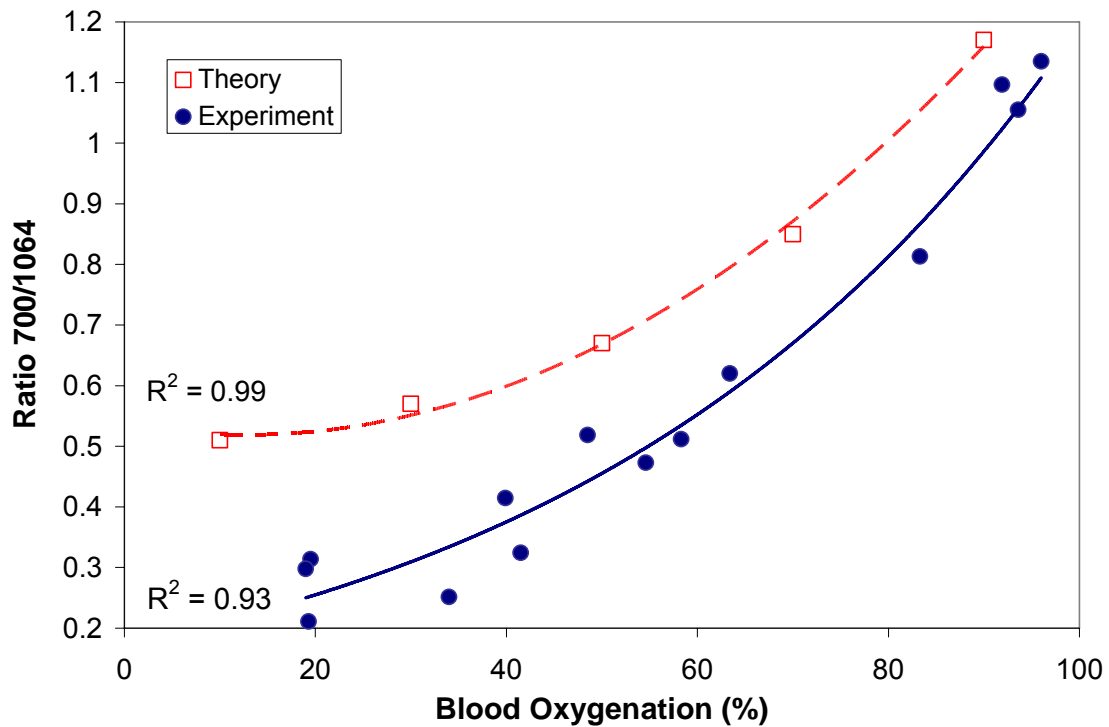


Figure 23: Ratio of temporal profiles 700 nm / 1064 nm for sheep from both cycles (blue filled circles) and derived from computer modeling using Monte Carlo simulation (red squares) [56].

To test the stability of the new data processing method in terms of intersubject variability we combined the ratio of all four successful sheep into one graph. Figure 24 shows the ratio of the normalized amplitude of signals generated at 1064 nm and 700 nm for all four successful sheep and both cycles.

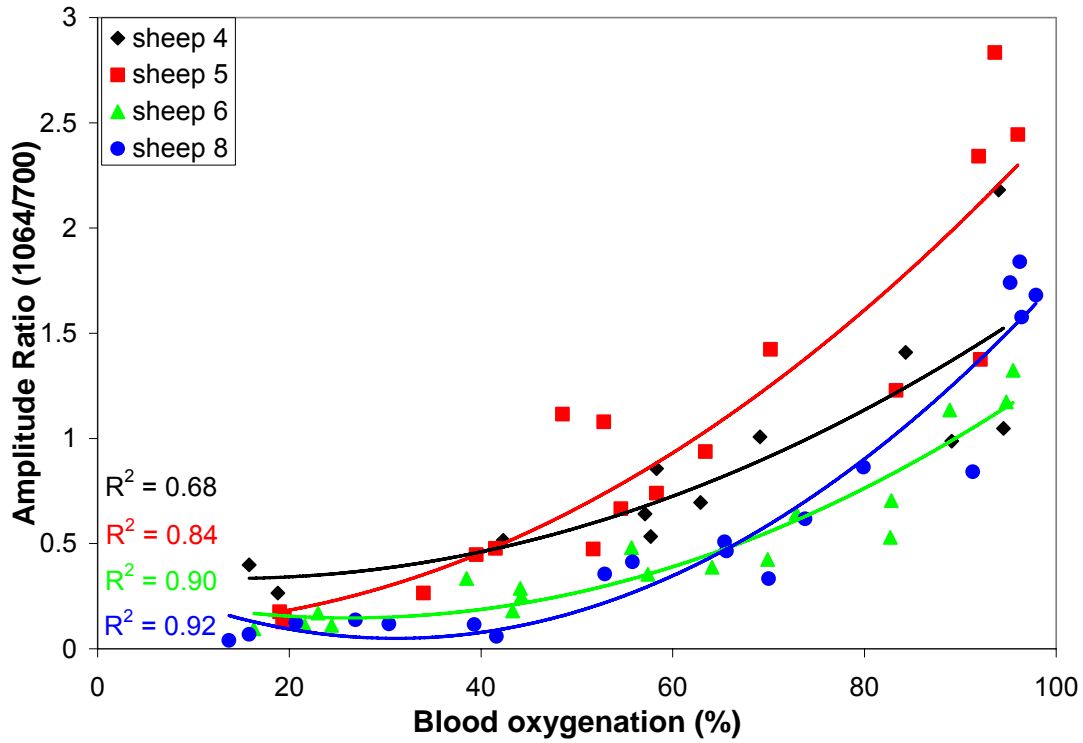


Figure 24: Ratio of normalized amplitudes 1064 nm / 700 nm of all sheep.

The amplitude ratio is similar for all sheep at low levels of blood oxygenation (below 50%). At higher levels the ratios of the different sheep diverge.

For comparison, Figure 25 shows the ratio of the inverse integral of signals generated at 1064 nm and 700 nm for all four sheep and both cycles.

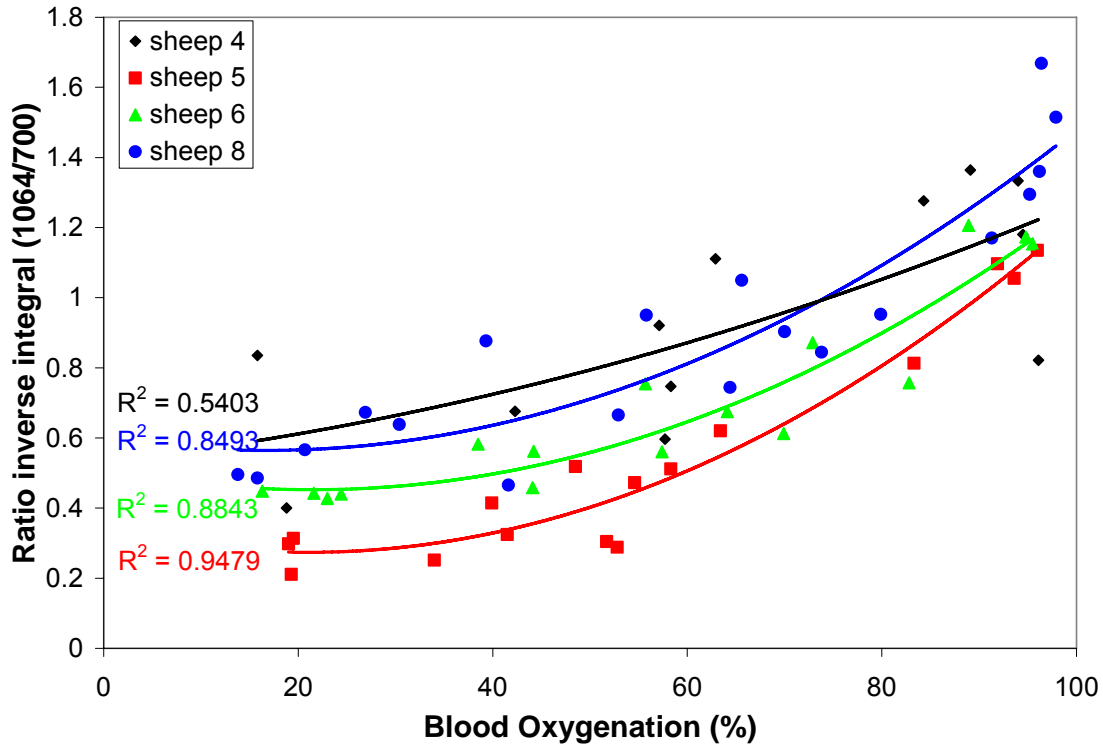


Figure 25: Ratio of temporal profiles 700 nm / 1064 nm of all sheep

The ratios of the temporal profile of the sheep are closer at higher levels of blood oxygenation (60-100%), which is the clinically important region for the measurement of blood oxygenation. The general shape and slope of the ratios between the sheep is similar, but it seems that there is an offset between the sheep.

In vivo studies in eight sheep showed good correlation between the optoacoustic signal amplitude and blood oxygenation. Data processing with the use of the inverse integral method further improved correlation with blood oxygenation. Integration reduced the effect of oscillations generated in the optoacoustic probe. The ratio of the inverse integral obtained at 1064 nm and 700 nm closely followed theoretical data (Figure 23) and allowed the determination of blood oxygenation within 10% for blood oxygenations in the

important clinical range (50-90%). However, when combined the evaluation of the temporal profile did not improve intersubject variability between the different sheep. The small range of overall change with blood oxygenation increased the intersubject variability.

CHAPTER 7: INTERMEDIATE PROBE DESIGNS

The next probe built was again a piezo ceramic probe. The piezo ceramic element had a thickness of 0.2 mm which gave the probe a central frequency of 10 MHz. The element was round and had a diameter of 3 mm. The positive electrode was soldered to a bullet shaped brass backing. The parabolic shape of the backing was selected to reduce reflections of the ultrasound wave within the backing. The sides of the transducer were coated with hollow glass microspheres in an epoxy matrix. This coating was selected for its sound absorbing qualities. Electrical shielding and the ground electrode were combined in a layer of conductive paint and successive electrolytically deposited layers of copper, nickel, and gold. Moreover, the gold layer reflected most of the backscattered light to reduce signal on the surface of the optoacoustic probe. Optical illumination was provided by a separate 1 mm optical fiber that was not included in the probe. The same set of amplifiers was used as in the previous optoacoustic probe. Figure 26 shows a schematic diagram of the probe.

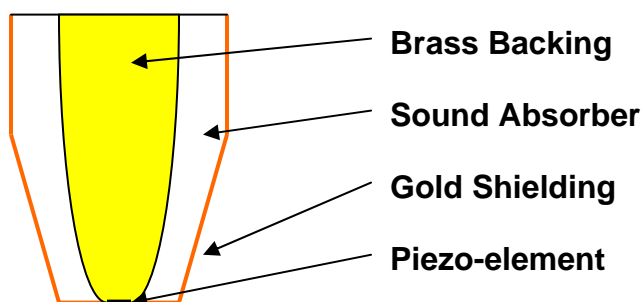


Figure 26: Schematic representation of the 10 MHz piezo ceramic optoacoustic probe.

The frequency response of the optoacoustic probe was tested in the transmission mode (Figure 5). To determine the bandwidth of the piezo ceramic probe, we applied a very short pulse to the piezo element. A 1-cm thick quartz glass plate was used as the hard boundary. The quartz plate facing the laser beam ensured that the signal had no negative part due to decompression at a soft boundary. A 2-mm thick black rubber layer with a very high absorption coefficient was used to generate the pulse. Acoustic contact was maintained with ultrasound gel. The laser pulse at 1064 nm from the Nd:YAG laser was expanded to 4 cm to prevent diffraction of the resulting ultrasound wave due to edge effects. Figure 29 shows the resulting signals of the short pulse measured with the piezo ceramic transducer. The experiment was repeated to ensure repeatability. The signals shown are an average of over 300 signals.

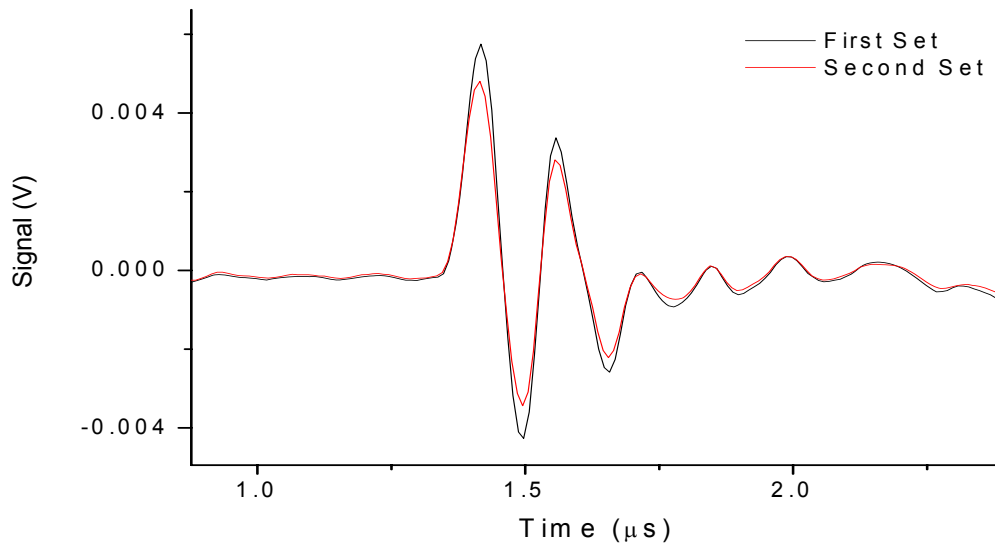


Figure 27: Two optoacoustic signals derived from 2-mm thick black rubber with ultra high absorption coefficient.

The impulse response of our optoacoustic probe showed extensive ringing with a distance between peaks of $0.1 \mu\text{s}$. This delay corresponds to the 10 MHz

center frequency of our piezo ceramic material. The ringing of this transducer was so extensive that further experiments were abandoned.

Next we moved to piezo composite transducers. The acoustic impedance of the piezo composite transducer was 17 MRayl, which is similar to that of aluminum. The transducer element could not be soldered and conductive epoxy could not provide a satisfactory connection. The acoustic impedance of a material can be varied by changing its density [⁵²]. We were able to increase the acoustic impedance by adding tungsten powder into an epoxy matrix. We were able to produce tungsten-filled epoxies with acoustic impedances of up to 11 MRayl but not the necessary 17 MRayl to match the piezo composite transducers. PVDF material has an acoustic impedance of 2.7 MRayl, the same as polycarbonate.

CHAPTER 8: PVDF PROBE DESIGN AND RATIONALE AND TEST

The piezo ceramic probe had a high acoustic impedance (~ 30 MRay) compared to that of tissue (~ 1.5 MRay). This mismatch in the probe and tissue impedances produced reflection of the optoacoustic signal. In the piezo ceramic transducer 85% of the ultrasound wave propagating from the tissue to the piezo-element was reflected, while only 15% entered the transducer and was converted into voltage.

To overcome shortcomings of our previous piezo ceramic probe, we built our second probe using PVDF material. The acoustic impedance of PVDF is significantly lower (2.7 MRay) than that of the piezo ceramic material. This matching between probe and tissue impedances was expected to substantially reduce the unwanted reflections. The optoacoustic probe featured a ring-shaped PVDF element with a central frequency of 10 MHz that converted the applied pressure into an electrical signal (Figure 28). The inner diameter of the element was 2 mm while the outer diameter of the element was 6 mm. The thickness of the piezo-element was 110 μm . The piezo-element was attached to a polycarbonate backing. A single 1-mm optical fiber at the center of the piezo-element provided illumination. The signal from the piezo-element was amplified with the 17 dB low-noise hydrophone preamplifier (Specialty Engineering Associates, A17DB). The probe had an aluminum housing to provide electrical shielding. The piezo-element was electrically shielded with a thin copper foil covered with electrolytically deposited gold. The reflecting layer reduces light absorption and signal generation in the probe itself.

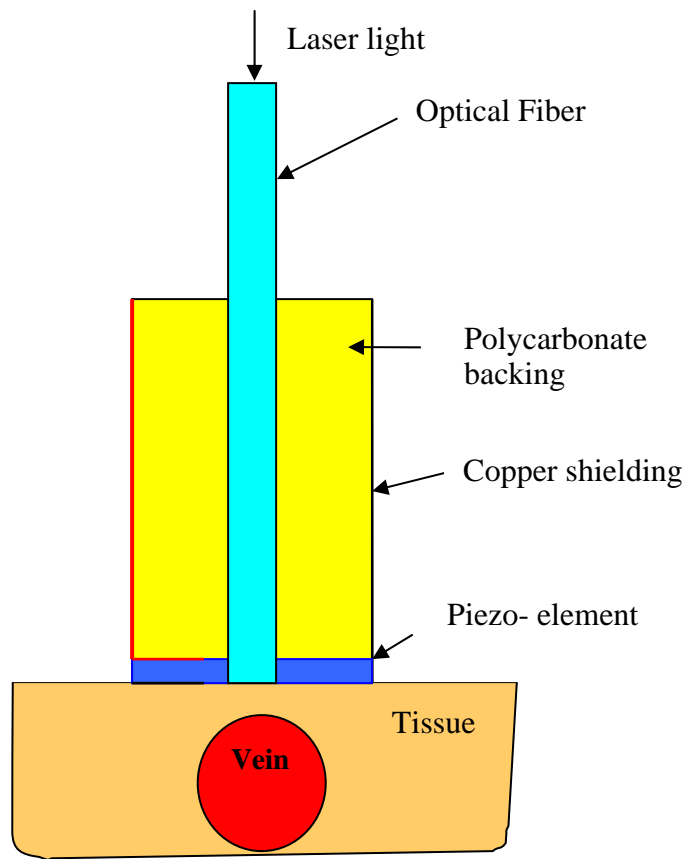


Figure 28: Schematic representation of the PVDF probe cut lengthwise overlying the jugular vein phantom.

Probe Test

The frequency response of the PVDF probe was tested in the same manner as in the previous probe. A 1-cm thick quartz glass plate was used to provide a rigid boundary. The 2-mm thick black rubber with a very high absorption coefficient was used to generate an ultra-wide band optoacoustic pulse. Acoustic contact was maintained with ultrasound gel. The frequency range of the amplifier used was 5 kHz to 25 MHz [53]. Figure 29 shows the resulting signal.

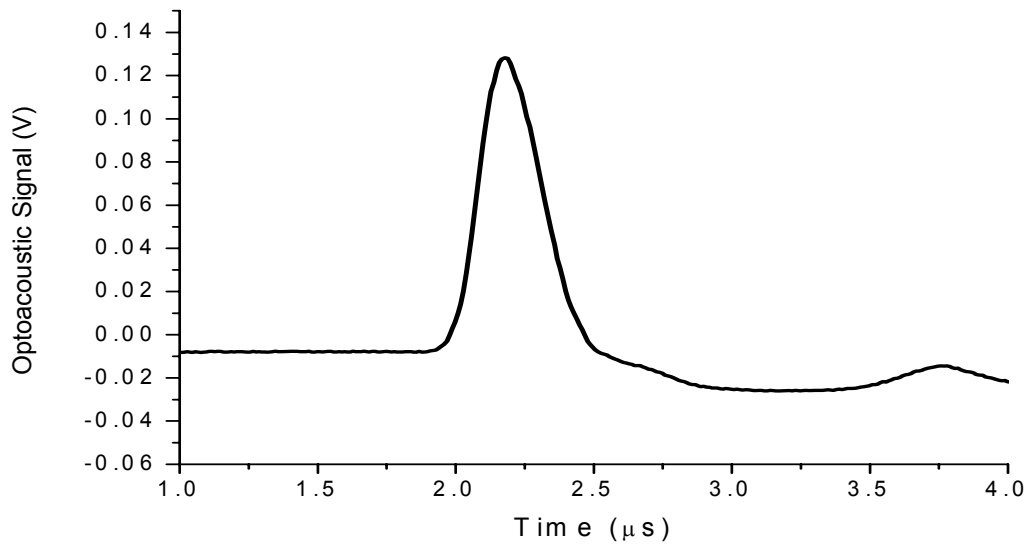


Figure 29: Optoacoustic signal measured from 2-mm thick black rubber with ultra high absorption coefficient.

The response of the PVDF probe shows a much cleaner signal than the piezo ceramic probe (Figure 12). No ringing was detected which should simplify data processing.

Using a Fourier transform we calculated the voltage spectrum of this signal which yielded the frequency response of our optoacoustic probe. The

bandwidth was greater than that of the piezo ceramic probe. Figure 30 shows the frequency response of the PVDF probe.

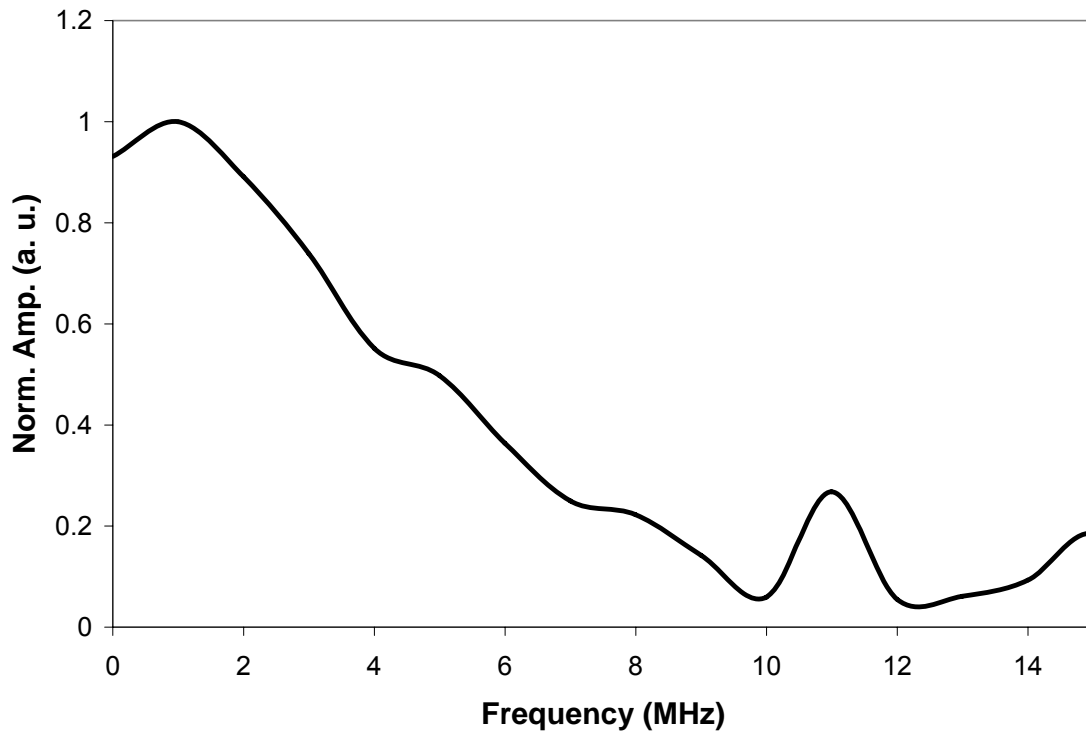


Figure 30: Voltage spectrum of optoacoustic signal measured from the 2-mm thick strong absorbing rubber.

The PVDF probe had a bandwidth of 5 MHz in comparison to the 3.6 MHz bandwidth of the piezo ceramic probe. There is an additional peak at 10 MHz that corresponds to the 10 MHz center frequency of the transducer material used.

Scanning Setup

To eliminate the effect of lateral misalignment, a scanning system was used in the later experiments with the PVDF probes. The scanning system moved the optoacoustic probe across the phantom or blood vessel. The scanning system consisted of a linear stage (New England Affiliated

Technologies) which was controlled by a stepper motor (Rapidsyn Mod. 23d-6102BN) and driver (New England Affiliated Technologies MDM7). Custom designed LabVIEW®-based software controlled the data acquisition portion and the scanning system. The system was configured to perform a 12.5- μm step upon receiving a Transistor Transistor Logic (TTL) pulse. The TTL pulses were delivered using a USB multifunction data acquisition board (National instruments USB-6008), while the signal acquisition was performed using a high speed 2-channel data acquisition board (National Instruments 5112). The driver for the stepper motor could be powered off to allow for manual positioning of the stage while watching the signal in “Oscilloscope Mode” on the computer display. To perform the scan, the driver was switched on and the LabVIEW® program was switched to “Data Collection” mode. The program controlled the number of collection sites and the distance between the sites. Additionally, the number of signals collected and averaged at each site could be varied.

Angular Sensitivity

We estimated the angular sensitivity of the optoacoustic probe using the scanning system. The angular sensitivity was determined using an absorbing solution of 10 cm^{-1} . The optoacoustic probe was scanned across the 1.6-mm silicone tube while illumination of the target area was provided by an external 1-mm fiber which was fixed and did not move with the probe. The angle was determined using \tan^{-1} (probe displacement / tube depth). The tube depth was calculated using the temporal position of the optoacoustic signal from the tube, whereas the lateral displacement was set by the scanning system.

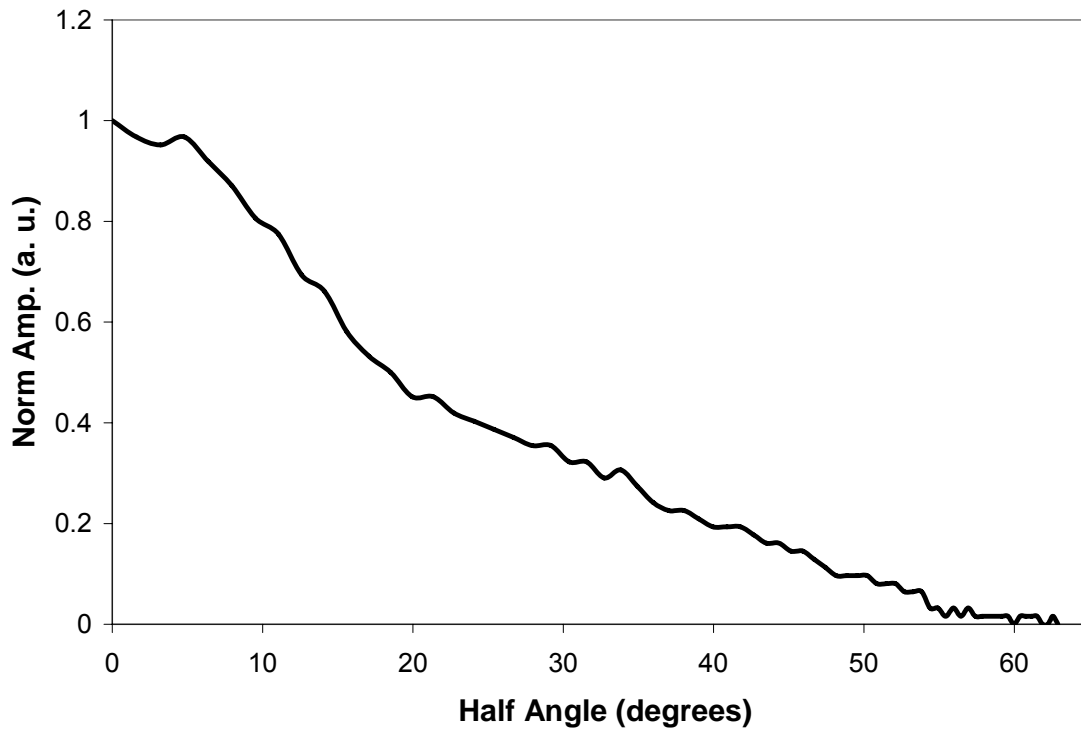


Figure 31: Normalized optoacoustic signal amplitude versus the angle of detection of the transducer.

The angular sensitivity was 60 degrees over the whole range and 18 degrees at the 50% level. Although the angular sensitivity was frequency dependent, this experiment allowed for a direct comparison of the probes.

CHAPTER 9: PHANTOM STUDIES WITH THE PVDF PROBE

Experimental Setup

The optoacoustic setup consisted of a Nd:YAG laser (Ultra CFR, Big Sky Technologies, Inc., Bozeman, MT) at a wavelength 1064 nm with pulse duration of 5 ns. The laser pulse was then coupled into an optical fiber, which directed the light to the optoacoustic probe. The optoacoustic probe was varied throughout the experiments. The optoacoustic signal collected from the probe was then amplified using pre- and secondary amplifiers and then acquired with a 2 Channel 100 MHz digitizer (NI 5112, National Instruments Corp., Austin, TX) and stored on the laptop computer using a LabView program developed in our laboratory.

The preamplifier used in our system was a 17 dB low-noise hydrophone preamplifier (Specialty Engineering Associates, AH-17DB), which was powered by batteries to reduce noise. The nominal voltage gain was 17 dB into 50 Ω . The input impedance was 1 M Ω in parallel with a capacitance of 20 pF. The frequency range of the preamplifier was from 5 kHz to 25 MHz [⁵³].

The secondary amplifier was a bipolar low noise amplifier (Model 322, Analog Modules, Inc. Longwood, FL), which was powered by a bench-top power supply. The nominal voltage gain was 40 dB with a bandwidth from 100 Hz to 10 MHz. The input and output impedance was 50 Ω . The noise was 280 pV/ $\sqrt{\text{Hz}}$.

Phantom Preparation

We used diluted Intralipid solution (an emulsion of fats) to mimic tissue. Intralipid is a nutritional supplement given intravenously to patients who are

unable to get enough fat in their diet. Intralipid is also widely used in optical experiments to provide the scattering component of tissue phantoms, preparations which mimic the optical properties of tissues [63]. The Intralipid solution was diluted to 1.5% to achieve an absorption coefficient of 0.05 mm^{-1} and a reduced scattering coefficient of 1.3 mm^{-1} at 975 nm, a typical value for biological tissue [40,64]. Due to the nature of the lipid model, the optical properties were constant and homogeneous. Optical heterogeneities common in biological tissue were not considered. The blood vessels were simulated by silicone tubing of various sizes filled with naphthol green solution with absorption coefficients of 5, 10, 15, and 20 cm^{-1} at the wavelength of 1064 nm.

Scanning Setup

To eliminate the effect of lateral misalignment, a scanning system was used in the later experiments with the PVDF probes. The scanning system moved the optoacoustic probe across the phantom or the blood vessel. The scanning system consisted of a linear stage (New England Affiliated Technologies) which was controlled by a stepper motor (Rapidsyn Mod. 23d-6102BN) and driver (New England Affiliated Technologies MDM7). Custom designed LabVIEW®-based software controlled the data acquisition part and the scanning system. The system was configured to perform a $12.5\text{-}\mu\text{m}$ step upon receiving a Transistor Transistor Logic (TTL) pulse. The TTL pulses were delivered using a USB multifunction data acquisition board (National instruments USB-6008), while the signal acquisition was performed using a high speed 2-channel data acquisition board (National Instruments 5112). The driver for the stepper motor could be powered off to allow for manual positioning of the stage while watching the signal in “Oscilloscope Mode” on the computer display. To

perform the scan, the diver was switched on and the LabVIEW® program was switched to “Data Collection” mode. The program controlled the number of collection sites and the distance between the sites. Additionally, the number of signals collected and averaged at each site could be varied.

The error associated with lateral misalignment could be reduced by scanning the optoacoustic probe. Figure 32 shows an example of the signal amplitudes normalized for such a scan.

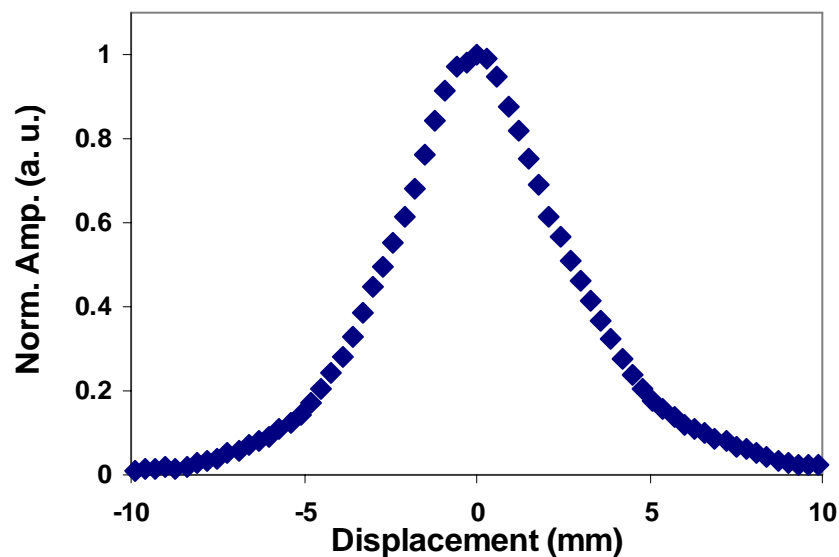


Figure 32: Typical scan of the optoacoustic probe across a jugular phantom ($d = 9.8$ mm) filled with naphthol green solution ($\mu_a = 15$ cm⁻¹).

The scanning was performed with an increment of 0.4 mm. This displacement interval ensured that the point of best alignment was not missed. At each step, 200 samples were collected and averaged. The criterion for the best probe-vein alignment was a maximum in the amplitude of the optoacoustic signal generated in the phantom. The signal from this location was then selected and used for further data processing. Figure 33 shows these maximal signals for four

solutions and water. The phantom used was naphthol green solution in a 9.8-mm ID and 12.7-mm ID silicone tube embedded in diluted Intralipid solution. The incident laser pulse energy was 1.23 mJ. No silicone spacer was used. The absorption coefficients of the solutions measured in a cuvette in transmission mode were 5.6, 8.6, 13.3, and 18.6 cm^{-1} . The range of absorption coefficients in the infrared region between fully oxygenated and deoxygenated blood was between 5 and 20 cm^{-1} .

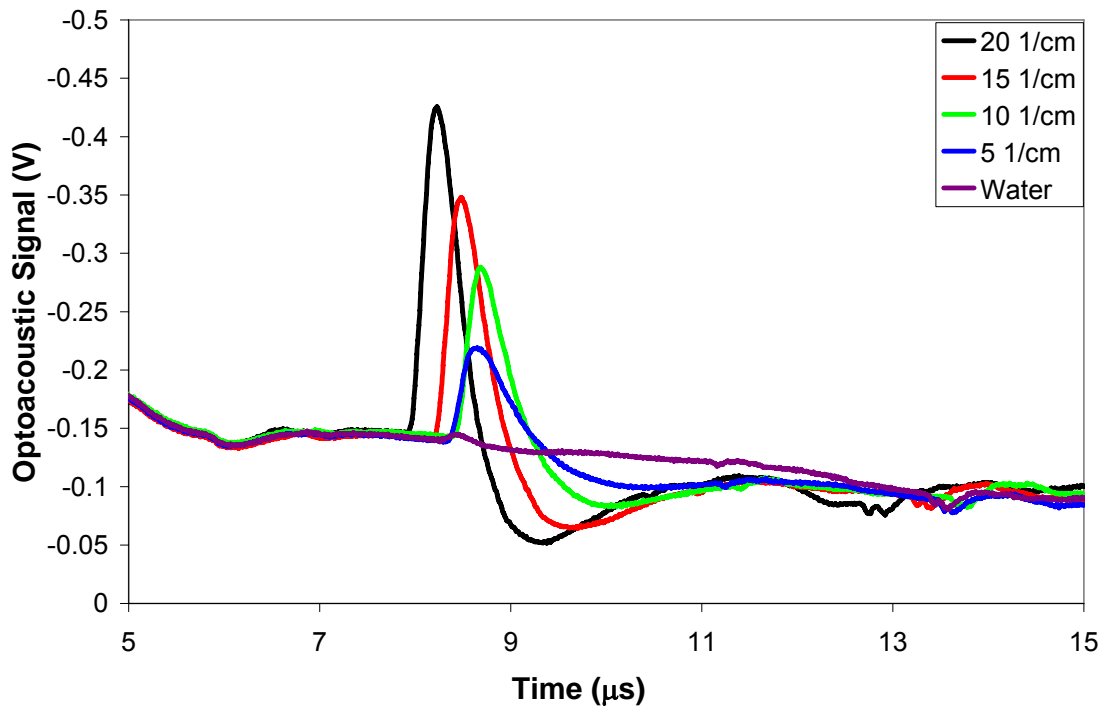


Figure 33: Optoacoustic signals recorded from the 9.8-mm jugular phantom filled with dye solutions of different absorption coefficients and water.

The variation of the temporal location of the optoacoustic signal likely resulted from axial displacement of the phantom that occurred during changing of the absorbing solutions. The solution was removed and the tube was flushed with pure water before new solution was added. The tubes had to be moved during

the changing of solutions and were not placed back at precisely the same location.

There was a signal offset generated by light back-scattered into the optoacoustic probe and absorbed in it. To remove the offset, the optoacoustic signal generated from the tube filled with water was used to subtract the offset from the corresponding signal filled with dye solution. Figure 34 shows the result of this subtraction.

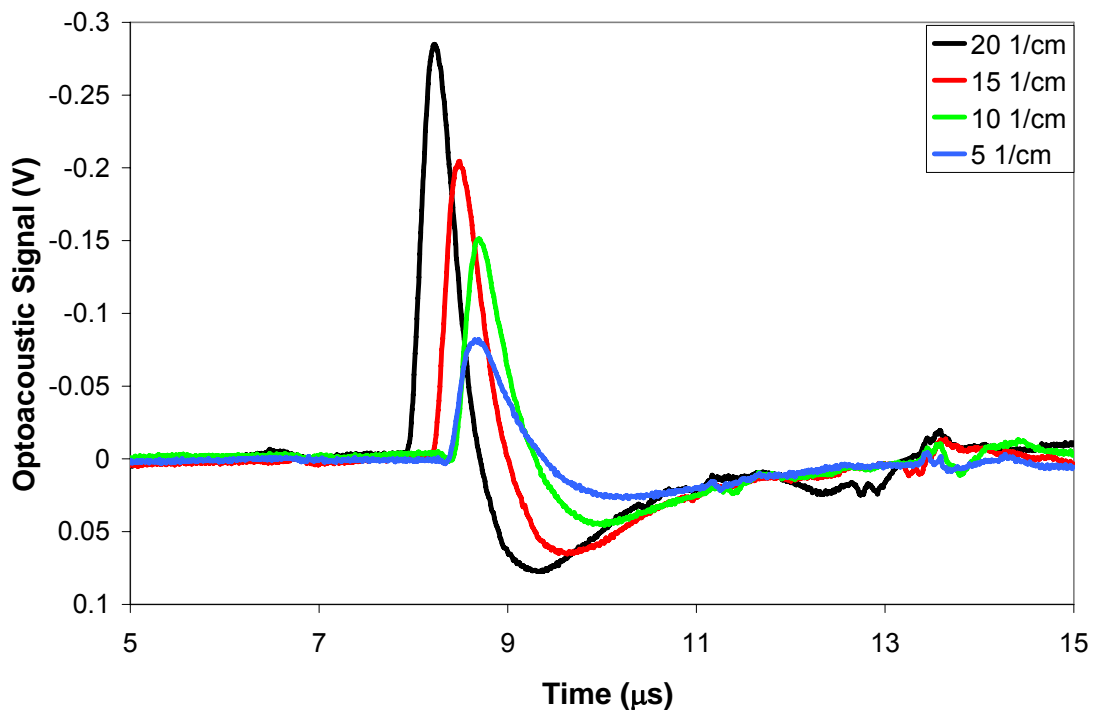


Figure 34: Optoacoustic signals recorded from the 9.8-mm jugular phantom filled with dye solutions of different absorption coefficients after water background subtraction.

The optoacoustic signal showed no ringing in comparison with the signals measures with the piezo ceramic probe. This shows that switching to PVDF material eliminated ringing in the transducer and allowed additional data processing methods.

In order to compare data processing algorithms, the data was first processed with the inverse integral method. Figure 35 shows the correlation of the inverse integral with the absorption coefficient of the phantom. The optoacoustic signals were processed in the same fashion as the signals from the sheep study.

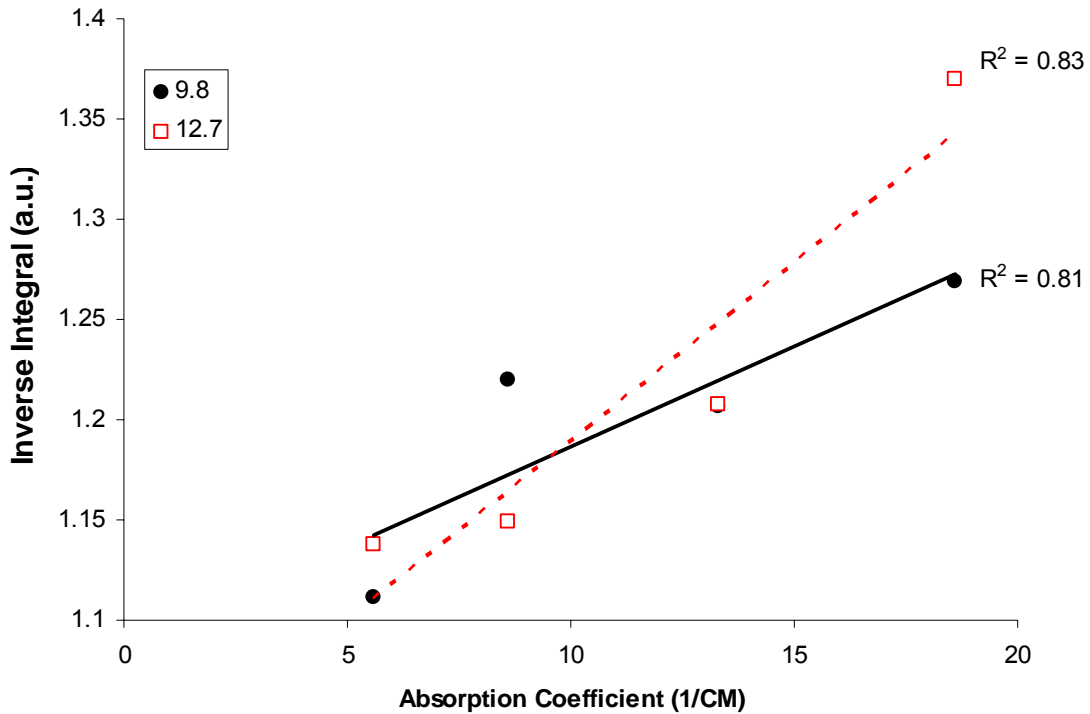


Figure 35: Correlation between the inverse integral of optoacoustic signals in the backward detection and actual absorption coefficient in silicone tubes (9.8 and 12.7 mm).

The change of the inverse integral was calculated by subtracting the minimum from the maximum, and then dividing by the minimum. These calculations resulted in a change of 13% for the 9.8-mm tube and 18% for the 12.7-mm tube.

Since the temporal profile of the optoacoustic signal recorded with the PVDF probe had much less ringing, it allowed us to use exponential fitting of the signals. The minima of the optoacoustic signal were normalized to 1. This normalization eliminated any amplitude effects on the exponential part of the

signal. An exponential fit was then applied to the decreasing part of the signal after a delay of 0.15 μs . This delay ensured that the fit was applied to the exponential part of the signal. The duration of the fit was 200 points corresponding to 2 μs at our sampling rate of 100 Ms. The 2- μs delay is equivalent to a depth of 3 mm in the tissue. The penetration depth of light at 20 cm^{-1} is 0.5 mm and 2 mm at 5 cm^{-1} . Figure 36 shows a diagram of the data processing algorithm utilizing the exponential fit.

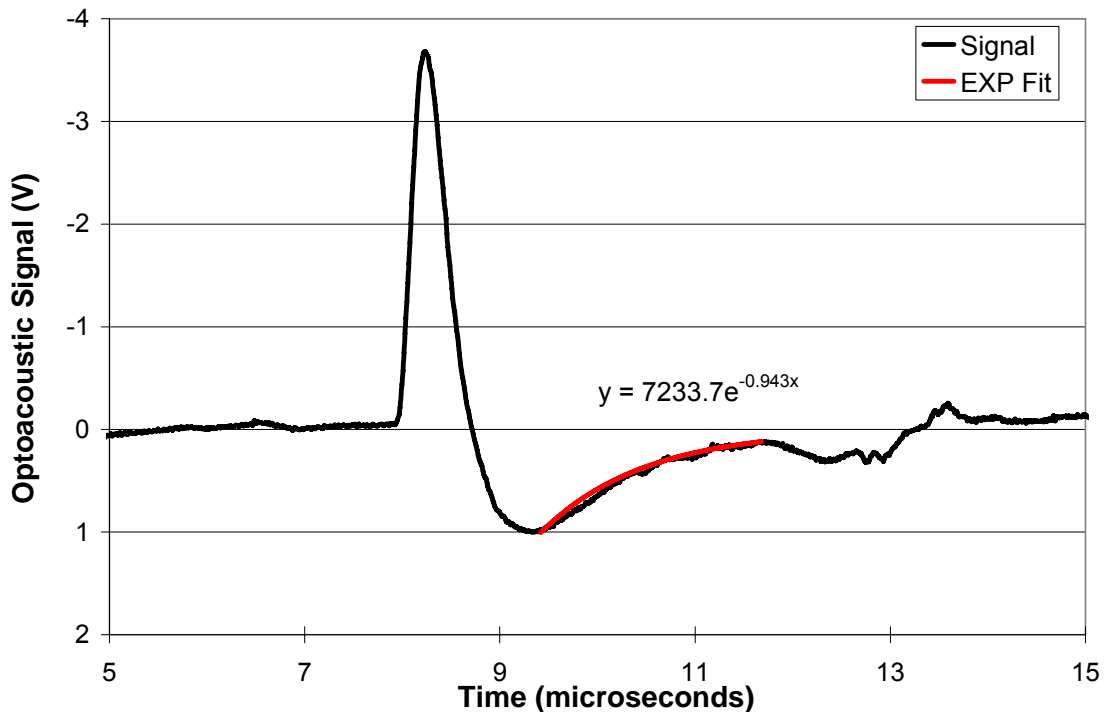


Figure 36: Diagram of the data processing algorithm utilizing the exponential fit.

Figure 37 shows the signals derived in the phantom studies processed with the exponential fit for two phantoms with an inner diameter of 9.8 mm and 12.7 mm.

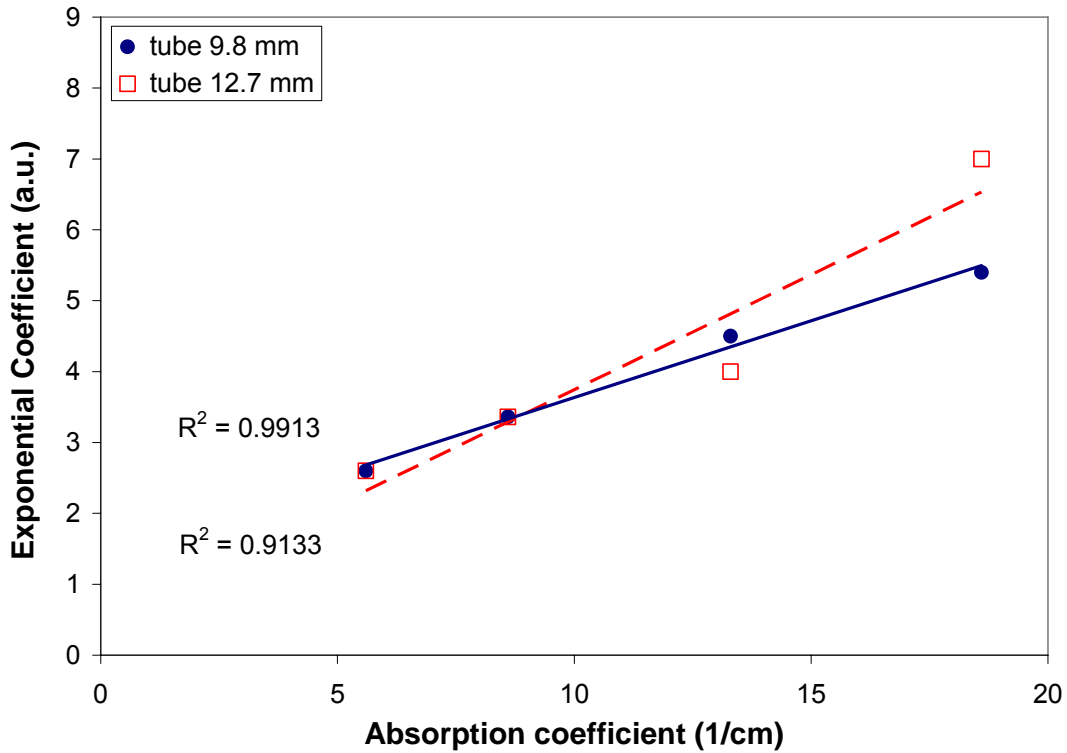


Figure 37: Correlation between measured exponential coefficient of optoacoustic signals in the backward detection and real absorption coefficient in silicone tubes (9.8 and 12.7 mm).

The use of the scanning system allowed the automatic, real-time acquisition of a series of signals across the phantom. Data processing determined the signal with highest amplitude (0 displacement of the probe). The effect of lateral displacement could therefore be eliminated. The PVDF material had a higher frequency bandwidth and showed no oscillations. This allowed the application of the exponential fit on the rising slope of the bipolar optoacoustic signals.

The phantom studies showed less ringing in the optoacoustic signals measured with the PVDF probe compared with the optoacoustic signals measured with the piezo ceramic probe. This allowed the application of an

exponential fit to the signal. The exponential coefficient derived from the exponential fits showed linear dependence on the absorption coefficient in the phantom.

Using the inverse integral method, the change in the phantom was 13% for the 9.8-mm tube and 18% for the 12.7-mm tube for naphthol green solutions with an absorption coefficient between 5 and 19 cm^{-1} . The change in the exponential coefficient was 150% for the 9.8-mm tube and 250% for the 12.7-mm tube, more than 10 times the change of the inverse integral. The greater change provided a better correlation and more accurate determination of the absorption coefficient.

CHAPTER 10: *IN VITRO* STUDIES WITH THE PVDF PROBE

Phantom Preparation

We used diluted Intralipid solution (an emulsion of fats) to mimic tissue. Intralipid is a nutritional supplement given intravenously to patients who are unable to get enough fat in their diet. Intralipid is also widely used in optical experiments to provide the scattering component of tissue phantoms as preparations which mimic the optical properties of tissues [63]. The Intralipid solution was diluted to 1.5% to achieve an absorption coefficient of 0.05 mm^{-1} and a reduced scattering coefficient of 1.3 mm^{-1} at 975 nm, a typical value for biological tissue [40,64]. The blood vessels were simulated by silicone tubing of various sizes. For *in vitro* studies, arterial sheep blood was circulated through the tubing using a peristaltic pump to prevent sedimentation and aggregation of the red blood cells. The pump was set to 50 rpm. Blood oxygenation was reduced using sodium hydrosulfite which competitively binds to hemoglobin therefore replacing the oxygen [12,65,66].

For the *in vitro* studies, the same experiments were performed as in the phantom studies except the absorbing dye solutions were replaced with sheep blood. Blood oxygenation was determined by detection of the hemoglobin saturation (SO_2) of each of the sheep blood samples using the CO-Oximeter. The duration of one scan was 20 minutes. Blood samples were taken 10 minutes into the scan. Figure 38 shows the resulting scans for SO_2 levels ranging from 94.3% to 14.5%. The inner diameter of the phantom was 12.7 mm.

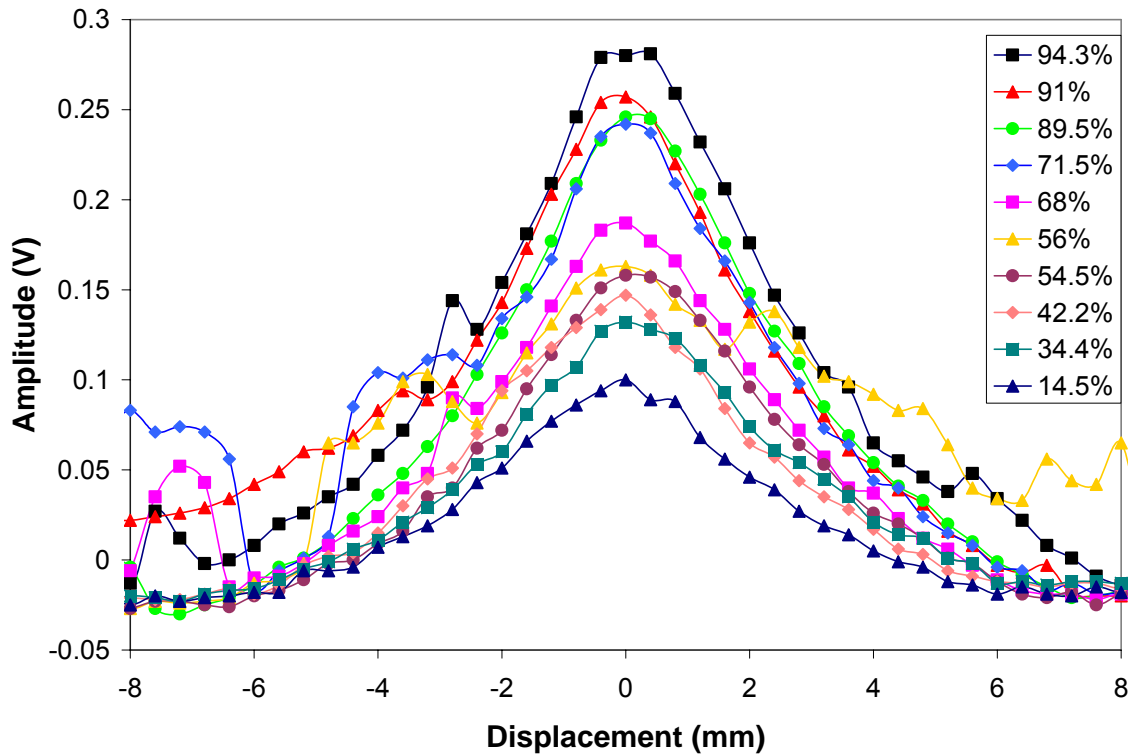


Figure 38: Multiple scans across a 12.7-mm jugular phantom containing sheep blood with blood oxygenation ranging from 94.3% to 14.5%.

The amplitude of the optoacoustic signal increased with oxygenation at 1064 nm. The spacing between scanning points was 0.4 mm. At each step 200 samples were collected and averaged. Figure 30 illustrates the effect of changes in blood oxygenation on the optoacoustic signal. Three representative optoacoustic signals derived from the phantom at three levels of blood oxygenation (94.3% - solid line, 54.5% - dashed line, and 14.5% - dotted line) are shown in Figure 39. The signals shown were measured at zero lateral displacement where the signal amplitude reached its maximal value.

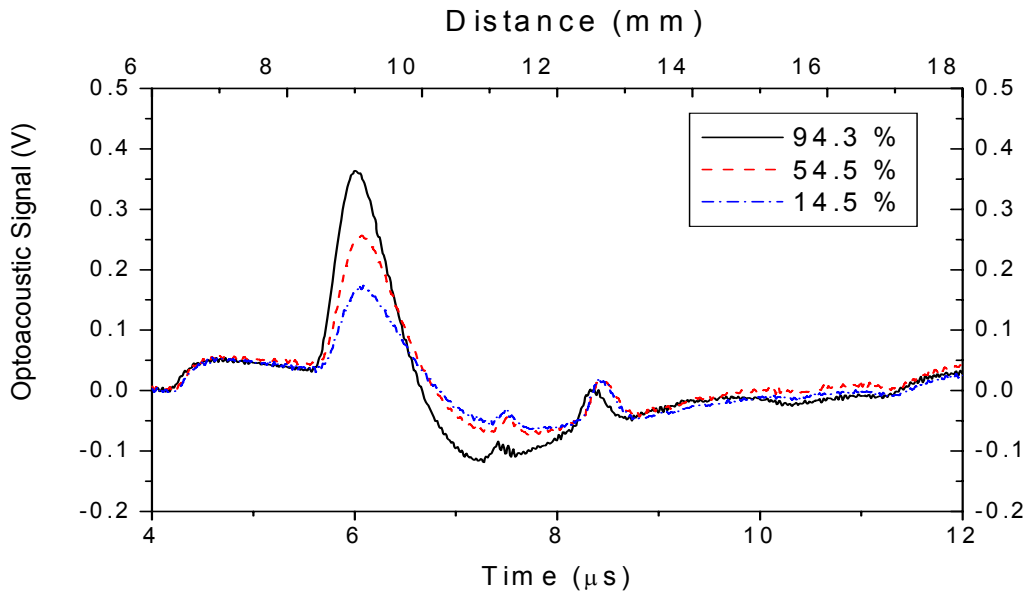


Figure 39: Optoacoustic signals recorded from the 9.8-mm jugular phantom filled with sheep blood of different levels of blood oxygenation.

The amplitude of the optoacoustic signal decreased with SO_2 as expected. There was a small offset in front of the signal generated in the phantom; this offset was attributed to absorption of a small amount of light in the tube surrounding the phantom. The two small peaks in the tail-end of the bipolar signal are assumed to be reflections from trapped air bubbles. Blood is very susceptible to trapping air bubbles.

For comparison the optoacoustic signals obtained in the *in vitro* studies were first processed using the inverse integral method, which was used for the sheep data with the piezo ceramic probe. Figure 40 shows the changes in the inverse integral with blood oxygenation for the 12.7-mm tube.

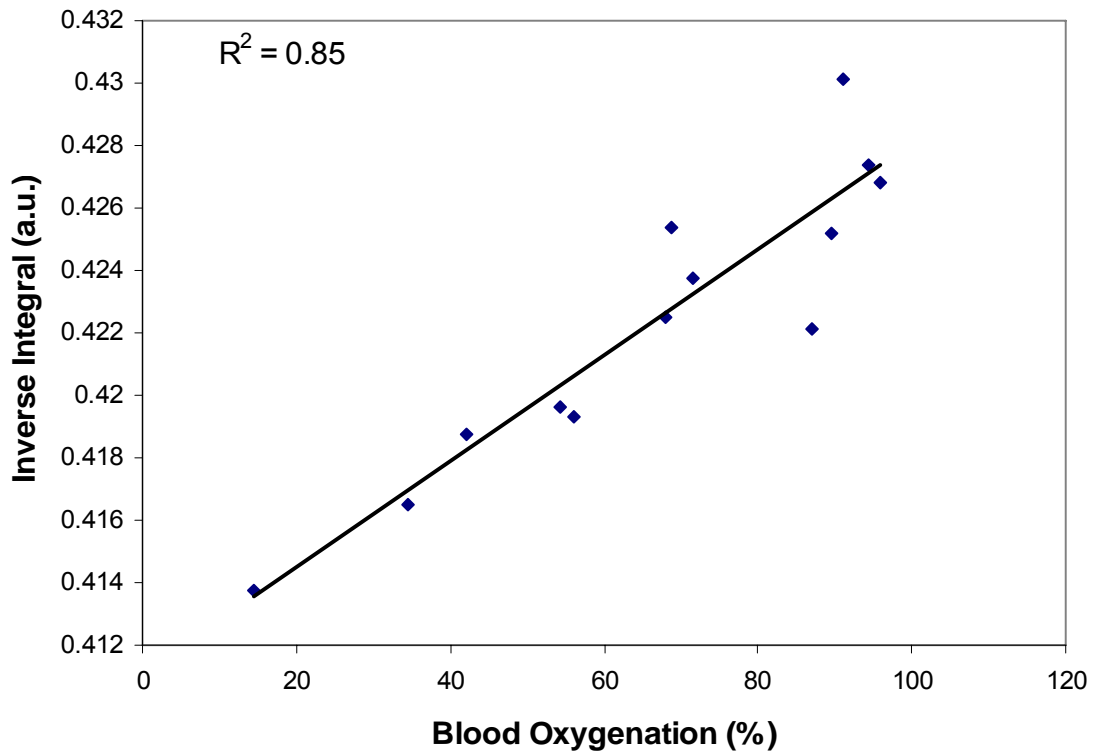


Figure 40: Correlation between inverse integral and blood oxygenation *in vitro* in a silicone tube with a diameter of 12.7 mm.

There was correlation with blood oxygenation of the optoacoustic signals but the overall change was small (0.3 arbitrary units or 3.8% change).

The exponential coefficient of the optoacoustic signals was determined for different blood oxygenations in the same fashion as the phantom experiments. The effective attenuation coefficient of deoxygenated and oxygenated blood ranged between 5 and 11 cm^{-1} [60]. Figure 41 shows the results of this fitting in phantoms in correlation with the absorption coefficient measured in the transmission mode.

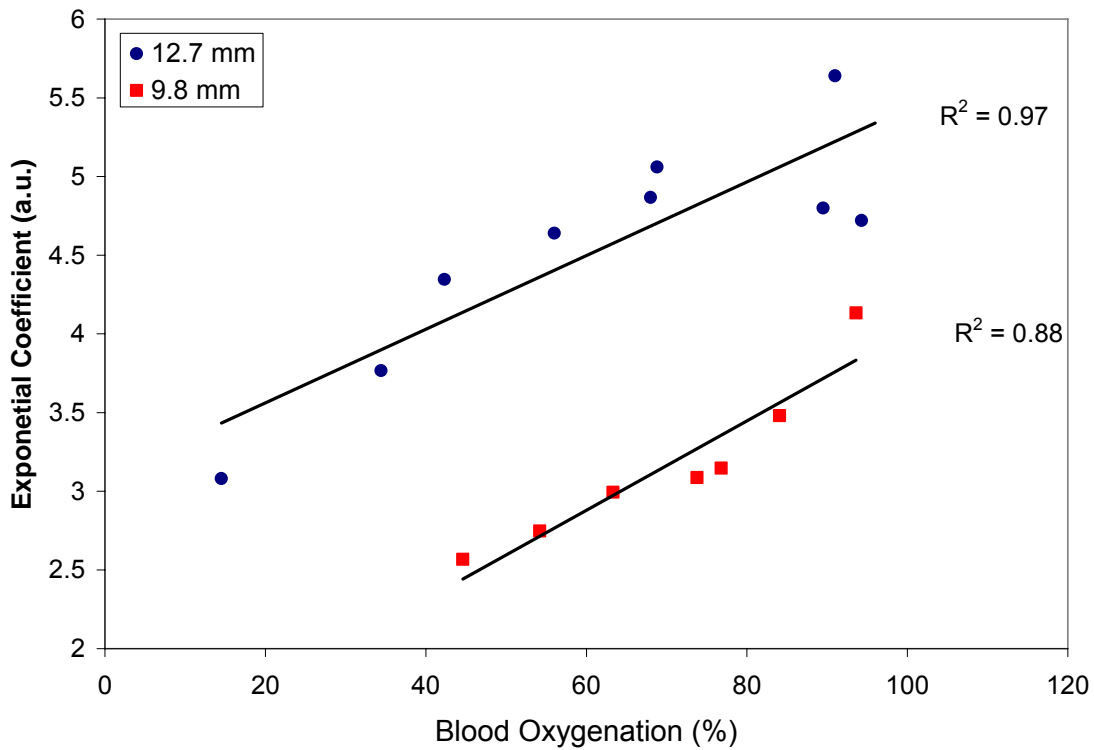


Figure 41: Correlation between exponential coefficient and blood oxygenation in two silicone tubes with a diameter of 9.8 and 12.7 mm.

The two outliers at high blood oxygenation levels in the 12.7-mm phantom were most likely due to inadequate mixing of the sheep blood with the sodium hydrosulfite and were not considered for the calculation of the coefficient of determination (R^2). Hydrosulfite is a powder and had the tendency to accumulate in corners with low blood flow in the circuit. If it was stirred up by taking blood samples it decreased blood oxygenation to a lower point. Points below 45% oxygenation in the 9.8-mm tube were not included due to the increase of methemoglobin (up to 20 %) that was noted during the measurements with the CO-Oximeter. Methemoglobin is a variation of hemoglobin. The iron in the heme group is in the Fe^{3+} state, not the Fe^{2+} state of normal hemoglobin. This renders methemoglobin unable to carry oxygen and gives it its brown color. Methemoglobin is converted back into hemoglobin by a NADH-dependent

enzyme called methemoglobin reductase. Normally 1-2% of human hemoglobin is methemoglobin.

The absorption coefficient of methemoglobin is higher than that of oxygenated blood at 1064 nm [^{41,67-69}]. Therefore, it increases the optoacoustic signal amplitude and the exponential coefficient in the measured signals. This falsifies the measurement of blood oxygenation. The optoacoustic signal amplitudes remained stable or even increased with a decrease of blood oxygenation due to the increase in methemoglobin instead of decreasing at 1064 nm.

The changes in the exponential coefficient in the phantom studies were much greater (~ 4 arbitrary units or 83% change). This greater change will allow for greater accuracy of blood oxygenation monitoring.

Next we tested the stability of the exponential fit toward lateral displacement. Utilizing the scanning system we determined the effect of lateral displacement between the probe and the phantom on the amplitude and the temporal profile of the optoacoustic signals. Figure 42 shows the dependence of optoacoustic signal amplitudes on blood oxygenation at various displacements (0, 1.2, 2.0, and 2.8 mm). The optoacoustic signal amplitude correlated well and linearly increased with blood oxygenation ($R^2 = 0.91$ at zero displacement). The dependence was less pronounced and the correlation decreased (lower R^2 values) with lateral displacement.

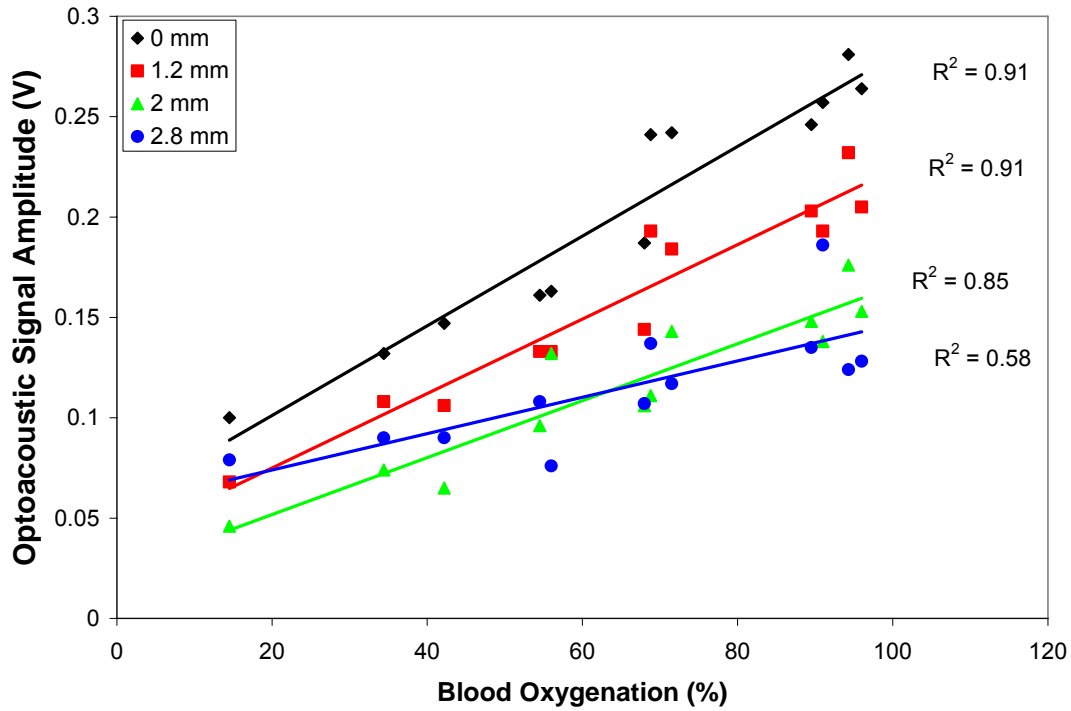


Figure 42: Correlation between optoacoustic signal amplitudes and blood oxygenation at various lateral displacements (0, 1.2, 2.0, and 2.8 mm).

Next the same data was processed with the application of the exponential fit. Figure 43 shows the dependence of the exponential coefficient on blood oxygenation at various displacements (0, 1.2, 2.0, and 2.8 mm).

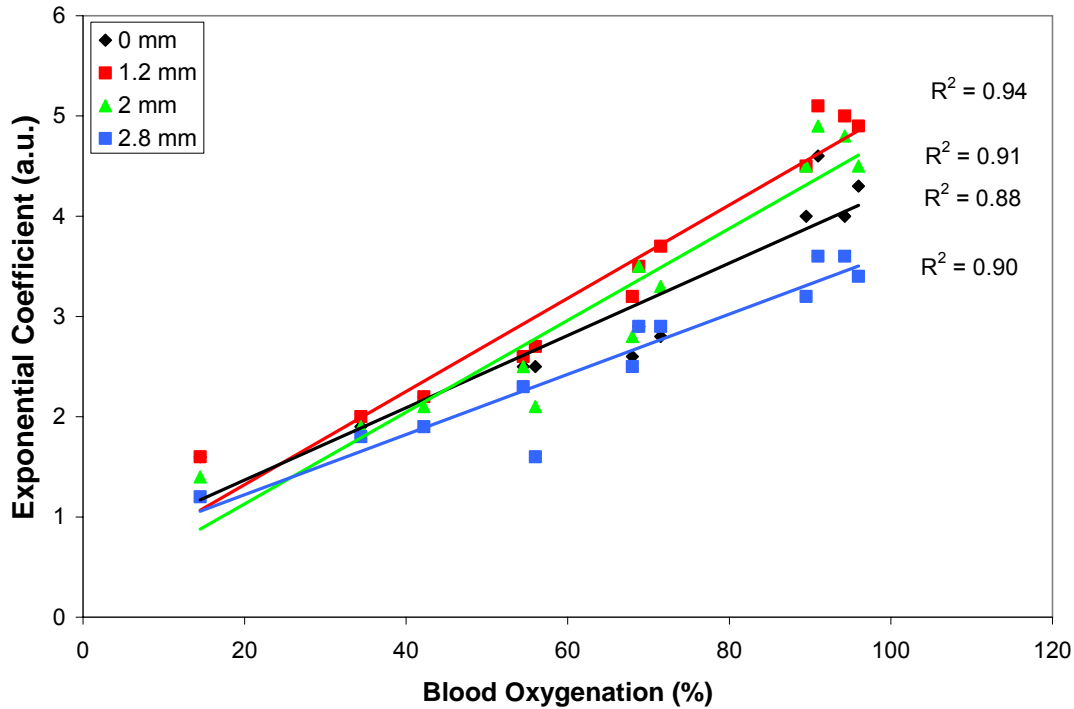


Figure 43: Correlation of the exponential coefficient with blood oxygenation at various displacements (0, 1.2, 2.0, and 2.8 mm).

The exponential coefficient correlated better than the optoacoustic signal amplitudes ($R^2 = 0.94$ at zero displacement). The exponential coefficient was less prone to lateral displacement and correlation with blood oxygenation was higher (R^2 values were higher compared to those for amplitude measurements). This showed the application of an exponential fit was stable against lateral displacement and provided better correlation.

The use of the scanning system allowed the automatic, real-time acquisition of a series of signals across the phantom. Data processing determined the signal with highest amplitude (0 displacement of the probe). The effect of lateral displacement could therefore be eliminated. The PVDF material had a higher frequency bandwidth and showed no oscillations. This allowed the

application of the exponential fit on the rising slope of the bipolar optoacoustic signals.

In the *in vitro* experiments the exponential coefficient changed 83% (Figure 41), while the inverse integral changed only 3.8% (Figure 40). The absorption coefficient of fully oxygenated blood is 11 cm^{-1} , while the absorption coefficient for deoxygenated blood is 6 cm^{-1} with a tHb concentration of 10 g/dl. This leads to a change of 83%, which is the same rate of change as the exponential coefficient. The greater range of change (20 times) in the exponential coefficient provided better correlation. Additionally it was resistant to lateral displacement.

CHAPTER 11: DESIGN RATIONALE AND TEST OF PVDF PROBE

2

Probe Design

A larger ring piezo-element should show better directional sensitivity than a smaller ring [^{33,70}]. Therefore, a third probe was made from a larger PVDF element with similar ring geometry. The inner diameter of the ring was 7 mm and the outer diameter was 10 mm. The dimensions were chosen to test the properties of a larger ring without being too large to widen the optoacoustic signal. The piezo-element was attached to a thicker 22.25-mm diameter polycarbonate backing in order to delay potential reflections and minimize their interference with the signal generated in the IJV. To prevent interference of the unwanted background with the optoacoustic signal, a polycarbonate disk was placed above copper shielding at the end of the probe. This polycarbonate disk was covered with a layer of 24 k leaf gold to reflect scattered light. Copper foil was used to electrically shield the probe. The 1-mm optical fiber was inserted into the center of the ring and protruded 2 mm out of the probe. Figure 44 shows a cross-section of the probe with a silicone spacer attached. The silicone spacer separated the signal generated in skin from the signal generated by scattered light to the piezo-element. Ultrasound gel was used to provide acoustical contact between the probe, silicone, and skin.

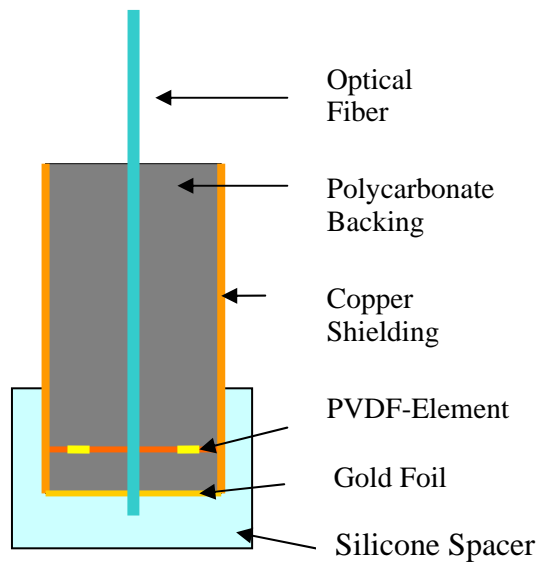


Figure 44: Schematic representation of the third PVDF probe.

Probe Test

The frequency response of the optoacoustic probe was tested as described for the previous two probes. Figure 45 shows the signal induced in the 2-mm black rubber with a very high absorption coefficient

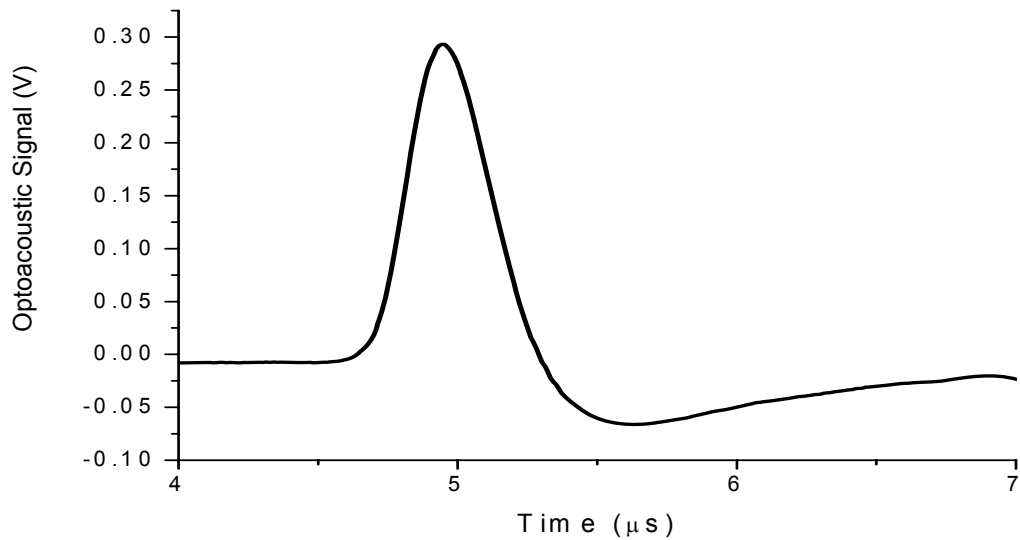


Figure 45: Optoacoustic signal recorded by the new probe from 2-mm thick black rubber with very high absorption coefficient.

Using a Fourier transform we calculated the voltage spectrum of this signal that represented the frequency response of the optoacoustic probe (Figure 46). The bandwidth was 4 MHz, wider in comparison to the piezo ceramic probe but smaller in comparison to the previous probe despite the use of the same PVDF material. The larger area of the active element may have widened the duration of the optoacoustic signal and reduced the recorded bandwidth of the probe. The frequency range of the amplifier used was 5 kHz to 25 MHz [53].

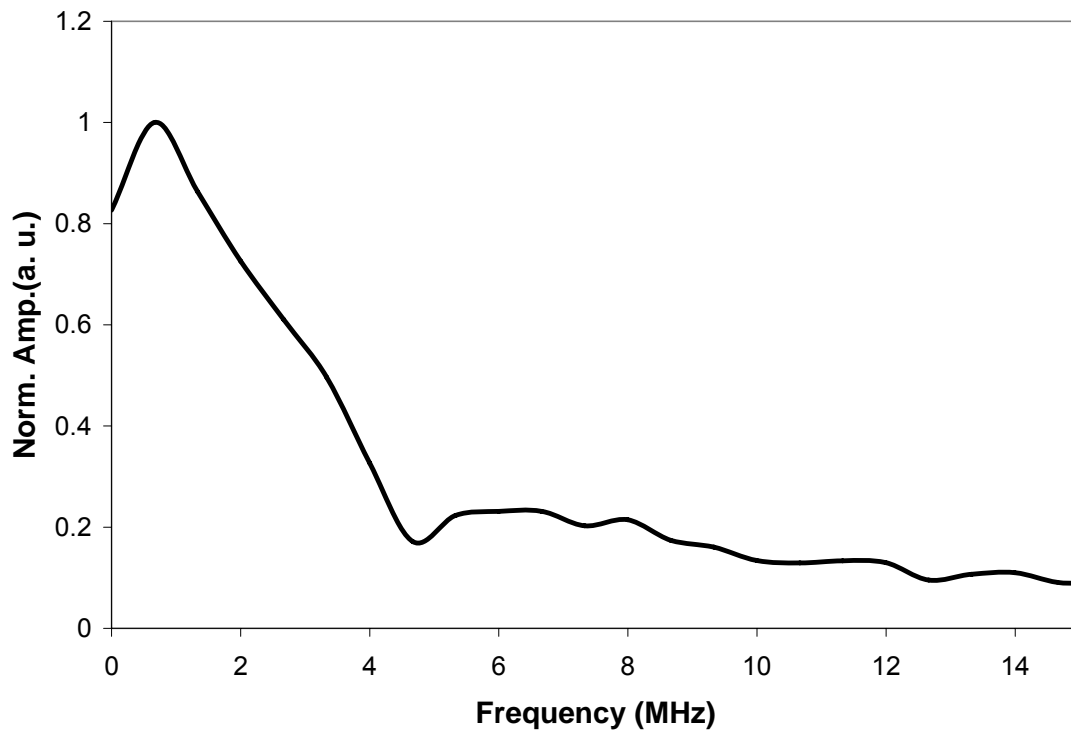


Figure 46: Frequency response of the new PVDF optoacoustic probe.

Angular Sensitivity

The angular sensitivity was determined as described for the previous optoacoustic probe. Figure 47 shows the result of the angular sensitivity test. The angular sensitivity of the new PVDF probe over the whole range was 50 degrees, 10 degrees smaller than that of the previous PVDF probe. At the 50% level the angular sensitivity was 22 degrees, 4 degrees wider than the previous probe.

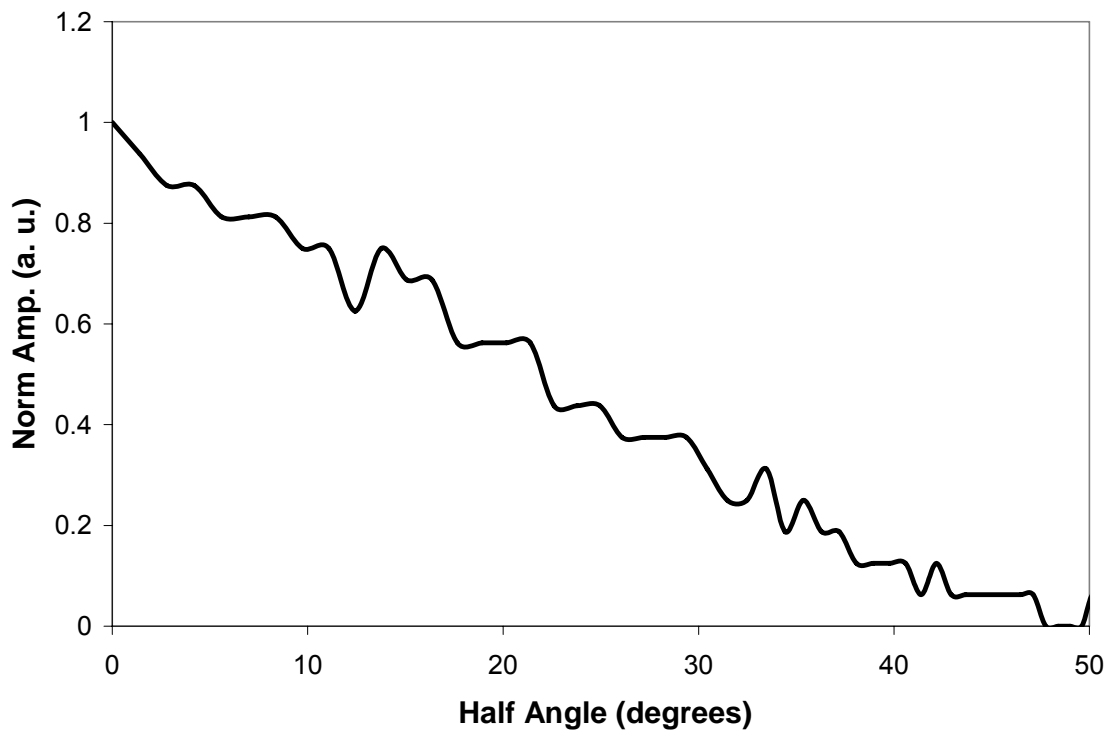


Figure 47: Normalized optoacoustic signal amplitude versus angle of incidence on the probe.

CHAPTER 12: PHANTOM STUDIES WITH PVDF PROBE 2

Experimental Setup

The optoacoustic setup consisted of an Nd:YAG laser (Ultra CFR, Big Sky Technologies, Inc., Bozeman, MT) at a wavelength of 1064 nm with pulse duration of 5 ns. The laser pulse was then coupled into an optical fiber, which directed the light to the optoacoustic probe. The optoacoustic probe was varied throughout the experiments. The optoacoustic signal collected from the probe was then amplified using pre- and secondary amplifiers and then acquired with a 2 Channel 100 MHz digitizer (NI 5112, National Instruments Corp., Austin, TX) and stored on the laptop computer using a LabView program developed in our laboratory.

The preamplifier used in our system was a 17 dB low-noise hydrophone preamplifier (Specialty Engineering Associates, AH-17DB) which was powered by batteries to reduce noise. The nominal voltage gain was 17 dB into 50 Ω . The input impedance was 1 M Ω in parallel with a capacitance of 20 pF. The frequency range of the preamplifier was from 5 kHz to 25 MHz [⁵³].

The secondary amplifier was a bipolar low noise amplifier (Model 322, Analog Modules, Inc. Longwood, FL) which was powered by a bench-top power supply. The nominal voltage gain was 40 dB with a bandwidth from 100 Hz to 10 MHz. The input and output impedance was 50 Ω . The noise was 280 pV/ $\sqrt{\text{Hz}}$.

Phantom Preparation

We used diluted Intralipid solution (an emulsion of fats) to mimic tissue. Intralipid is a nutritional supplement given intravenously to patients who are unable to get enough fat in their diet. Intralipid is also widely used in optical experiments to provide the scattering component of tissue phantoms, preparations which mimic the optical properties of tissues [63]. The Intralipid solution was diluted to 1.5% to achieve an absorption coefficient of 0.05 mm^{-1} and a reduced scattering coefficient of 1.3 mm^{-1} at 975 nm, a typical value for biological tissue [40,64]. Due to the nature of the lipid model the optical properties were constant and homogeneous. Optical heterogeneities common in biological tissue were not considered. The blood vessels were simulated by silicone tubing of various sizes filled with naphthol green solution with absorption coefficients of 5, 10, 15, and 20 cm^{-1} at the wavelength of 1064 nm.

Scanning Setup

To eliminate the effect of lateral misalignment, a scanning system was used in the later experiments with the PVDF probes. The scanning system moved the optoacoustic probe across the phantom or the blood vessel. The scanning system consisted of a linear stage (New England Affiliated Technologies) which was controlled by a stepper motor (Rapidsyn Mod. 23d-6102BN) and driver (New England Affiliated Technologies MDM7). Custom designed LabVIEW®-based software controlled the data acquisition part and the scanning system. The system was configured to perform a $12.5\text{-}\mu\text{m}$ step upon receiving a Transistor Transistor Logic (TTL) pulse. The TTL pulses were delivered using a USB multifunction data acquisition board (National instruments

USB-6008) while the signal acquisition was performed using a high speed 2-channel data acquisition board (National Instruments 5112). The driver for the stepper motor could be powered off to allow for manual positioning of the stage while watching the signal in “Oscilloscope Mode” on the computer display. To perform the scan, the driver was switched on and the LabVIEW® program was switched to “Data Collection” mode. The program controlled the number of collection sites and the distance between the sites. Additionally, the number of signals collected and averaged at each site could be varied.

The phantom studies were conducted in the same manner as with the previous PVDF probe. We used naphthol green solution with different absorption coefficients in silicone tubes surrounded by Intralipid solution. The optoacoustic probe was scanned across the phantom. Figure 48 shows the resulting optoacoustic signals before the subtraction of the water signal, while Figure 49 shows the same signal after the subtraction of the water signal.

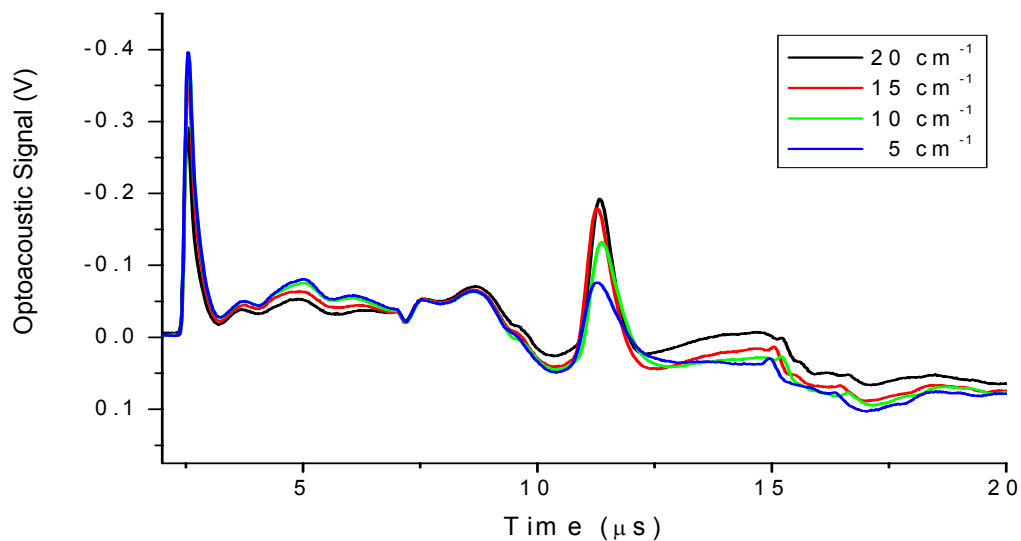


Figure 48: Optoacoustic signals recorded from the 12.7-mm jugular phantom filled with dye solutions of different absorption coefficients before water background subtraction.

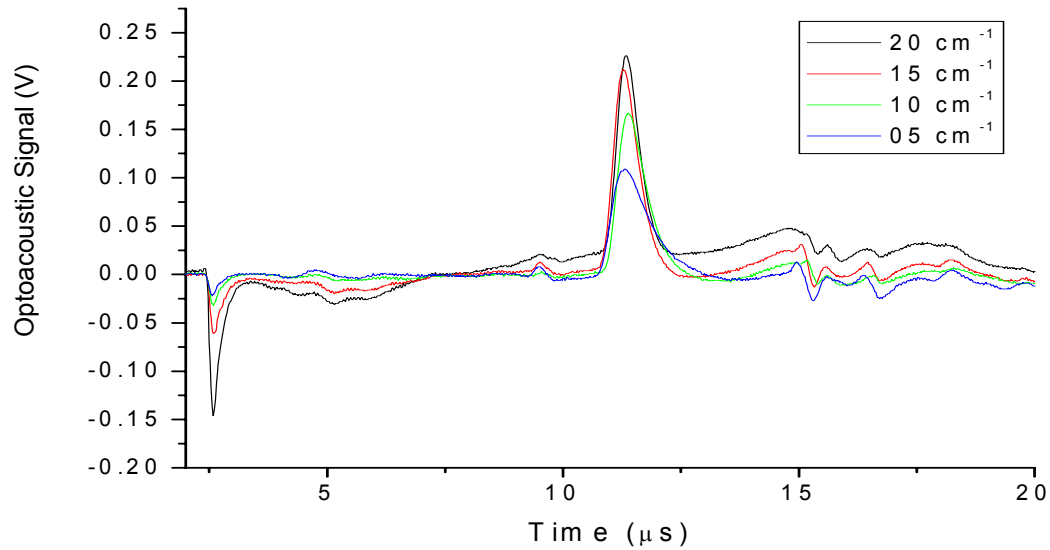


Figure 49: Optoacoustic signals recorded from the 12.7-mm jugular phantom filled with dye solutions of different absorption coefficients after water background subtraction.

A reflection in the optoacoustic signal generated in the phantom occurred at 15 μs which interrupted the monotonic decay of the signal. The 2- μs time interval between the minima of the bipolar signal and the reflection allowed data processing and application of an exponential fit.

The minima of the optoacoustic signal were normalized to 1. This normalization eliminated any amplitude effects on the exponential part of the signal. An exponent was then fitted to the decreasing part of the signal after a delay of 0.1 μs . This delay ensured that the fit was applied to the exponential part of the signal. The time interval for processing was varied to ensure that the exponential fit closely followed the signal and was not distorted by reflection in the probe. Figure 50 shows the results of this fitting in phantoms and correlation with the absorption coefficient measured in the transmission mode.

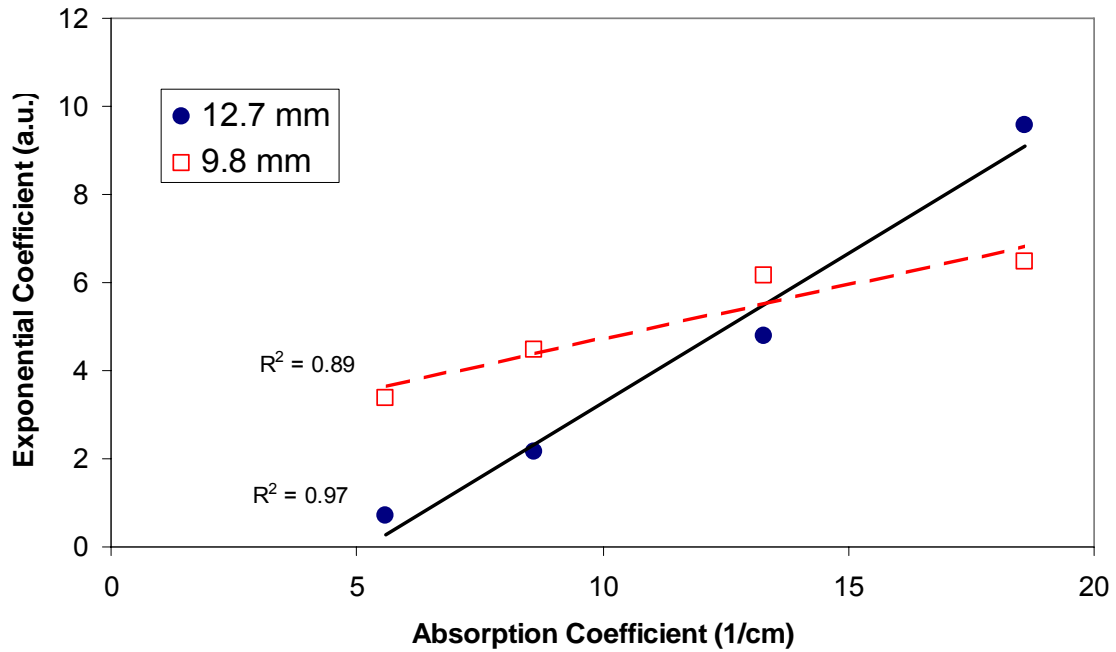


Figure 50: Correlation between exponential slope of optoacoustic signals and actual absorption coefficient in the silicone tube.

The correlation between exponential coefficient and absorption coefficient was better for the previous PVDF probe (Figure 37). Additionally the effect of tube diameter was increased. With the larger ring and smaller angle of acceptance, tube diameter related effects should have been reduced. Theoretically, a smaller angle of acceptance reduces the effect of curvature of the phantom.

CHAPTER 13: IN VITRO STUDIES WITH PVDF PROBE 2

Phantom Preparation

Polyvinylchloride – plastisol (PVC-P) is a material commonly used in fishing lures and other products. PVC plastisols are dispersions of finely ground PVC resin particles in plasticizer. This produces a liquid or paste which contains no volatile components. PVC plastisols are cured or fused into a homogeneous mass, at temperatures of 150 to 200°C, to melt the resin particles into the plasticizer.

The speed of sound through PVC-P and the density of PVC-P are similar to that of tissue. Moreover one can adjust the optical properties by adding titanium dioxide as a scattering agent and black plastic color to increase absorption [71]. Since PVC-P is a solid material, there is no need for tubing in the blood vessel phantom. Teflon® rods with diameters of 1, ¾, 5/8, and ½ inches (25.4, 19.05, 15.875, and 12.7 mm respectively) were imbedded in the PVC-P. After solidification, the Teflon® rods were removed to form cylindrical cavities. These cavities were filled with either naphthol green solution or sheep blood. The tubeless phantom allowed us to vary “blood vessel” diameter over a wide range and eliminated unwanted signals from the tube walls (Figure 32).

Experimental setup

For the *in vitro* studies a cardiovascular bypass system was used. The sheep blood was constantly circulated through the plastisol phantom using a peristaltic pump (Sarns Inc., Ann Arbor, MI; Model 700 MDX) to prevent settling

of red blood cells (RBCs). Blood oxygenation was varied using a membrane oxygenator (Cobe Cardiovascular, Arvada, CO Model HVR 3700) which also kept the blood at 38°C with the use of a heater (Sarns Inc., Ann Arbor, MI; Model 11160). Keeping the blood at body temperature facilitated changes in blood oxygenation and helped dissolve air bubbles trapped in the circuit. Blood oxygenation was varied by altering FiO_2 with a gas mixer (Puritan Bennet, Los Angeles, CA). FiO_2 was monitored using a multifunction gas analyzer (Datex, Helsinki, Finland, Model: Capnomac Ultima). The use of a membrane oxygenator allowed changing blood oxygenation while maintaining low levels of methemoglobin (<1.5%). Previous experiments performed with sodium hydrosulfite only allowed the decrease of blood oxygenation. Blood oxygenation was verified by taking blood samples at the time of measurement. Total hemoglobin and methemoglobin was measured in the sample with the CO-Oximeter.

Figure 51 shows the setup for the experiment with the phantom located in the front center of the picture. The scanning and data acquisition system is located at the left of the phantom, while the optoacoustic probe is above. The membrane oxygenator with the peristaltic pump is behind the phantom. The multifunction gas analyzer is located to the right.

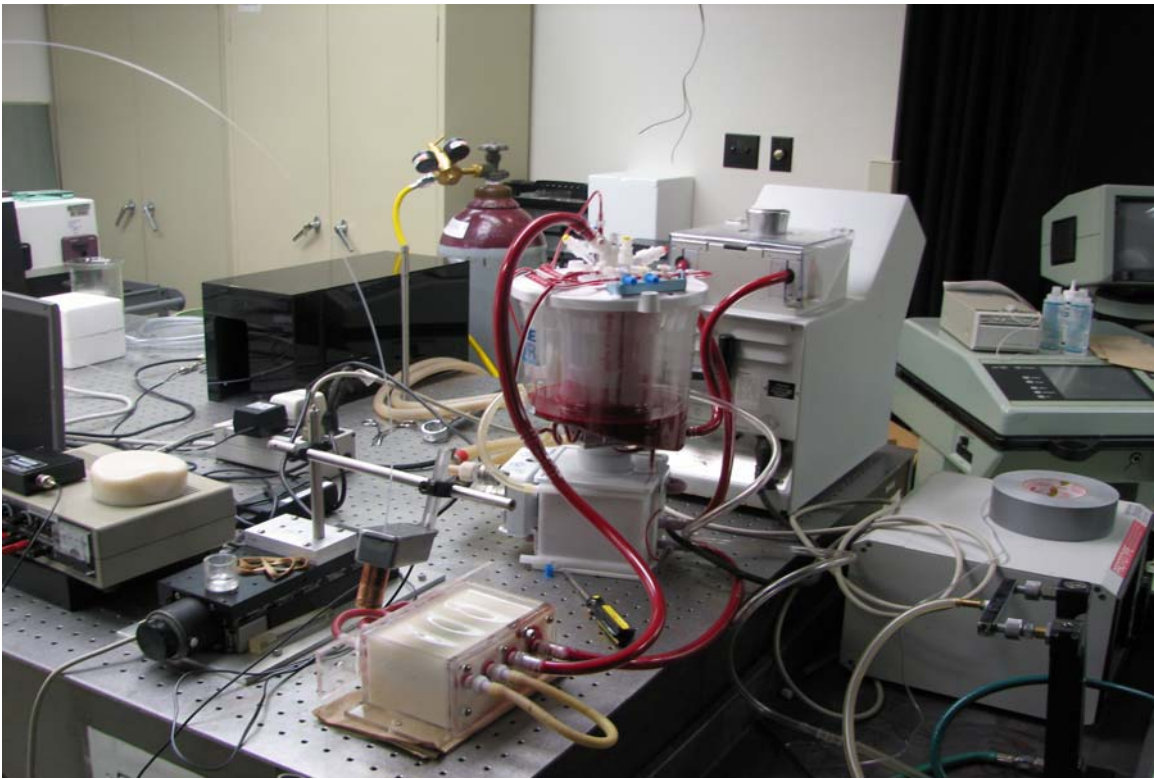


Figure 51: Experimental setup for *in vitro* studies.

The optoacoustic probe was scanned across the phantom, while a thin layer of water was used to maintain acoustical contact between the probe and phantom during the scan.

Figure 52 shows typical optoacoustic signals recorded at best alignment from the 25.4-mm phantom filled with blood with a range of blood oxygenations from 49.8% to 97.7%.

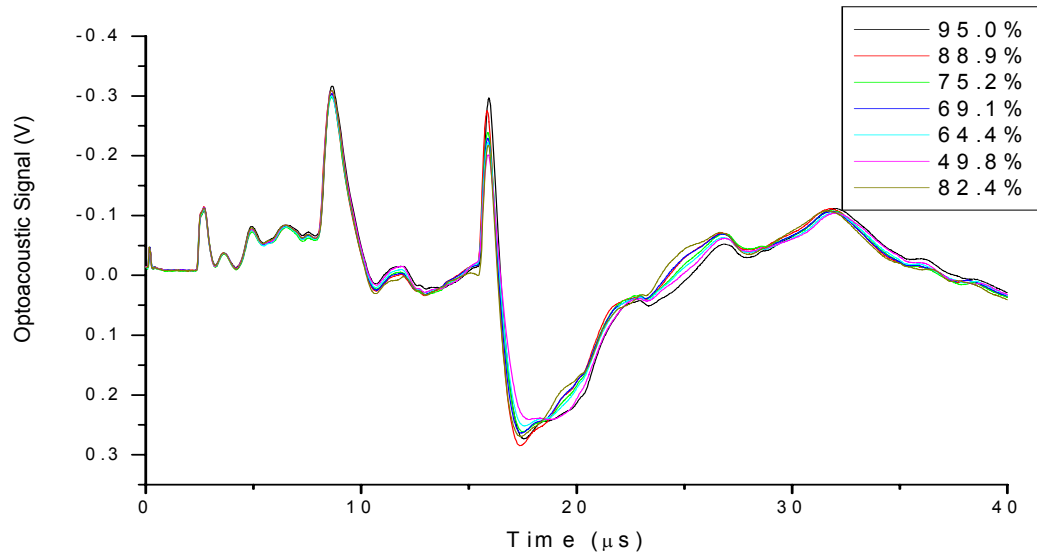


Figure 52: Optoacoustic signals recorded from the 25.4-mm jugular phantom filled with sheep blood of different blood oxygenations (96.5% to 49%).

The optoacoustic signal amplitude correlated well with blood oxygenation. However, the temporal profile could not be accessed due to effects generated in the phantom. A set of signals was acquired where the blood in the phantom was replaced by water. The resulting signals from the same location as the signals generated from blood were used for background subtraction.

Figure 53 shows the corresponding optoacoustic signals after water subtraction.

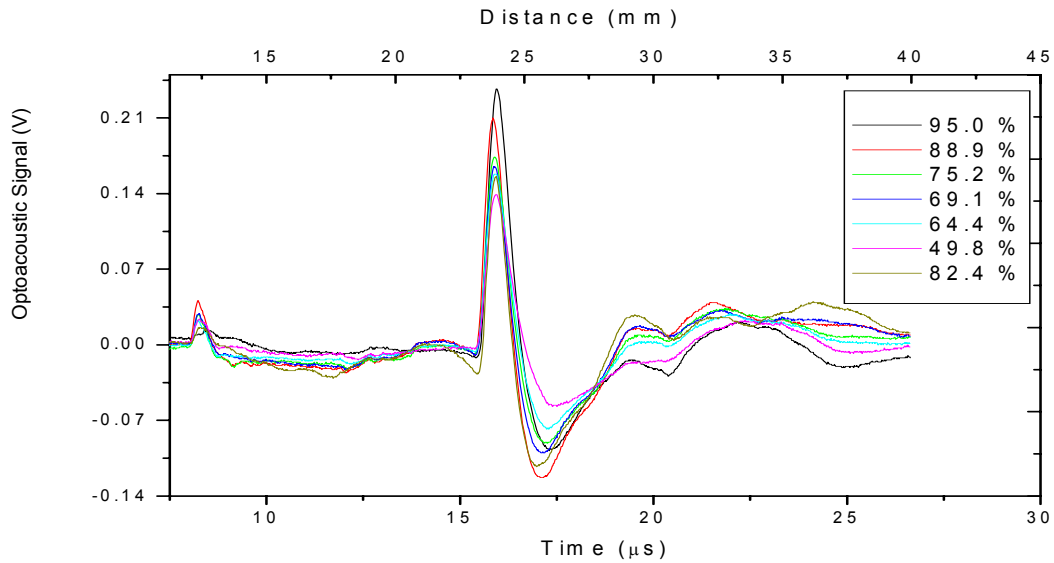


Figure 53: Optoacoustic signals from the 25.4-mm jugular phantom filled with sheep blood of varying blood oxygenation (49% to 96.5%) after water subtraction.

Normalizing the minima of the optoacoustic signal to 1 removed any correlation with blood oxygenation. The optoacoustic signals generated in the phantom did not have a monotonic exponential decay. Therefore, the application of an exponential fit to the rising slope of the exponential signal was not useful. Figure 54 shows the normalized optoacoustic signal amplitudes in correlation to changes in blood oxygenation for phantoms with various diameters. To account for variations of incident laser energy, the optoacoustic signal amplitudes were normalized to 1. The normalization allowed the comparison of the correlation between optoacoustic signal amplitude and blood oxygenation for different tube diameters independent of incident laser energy.

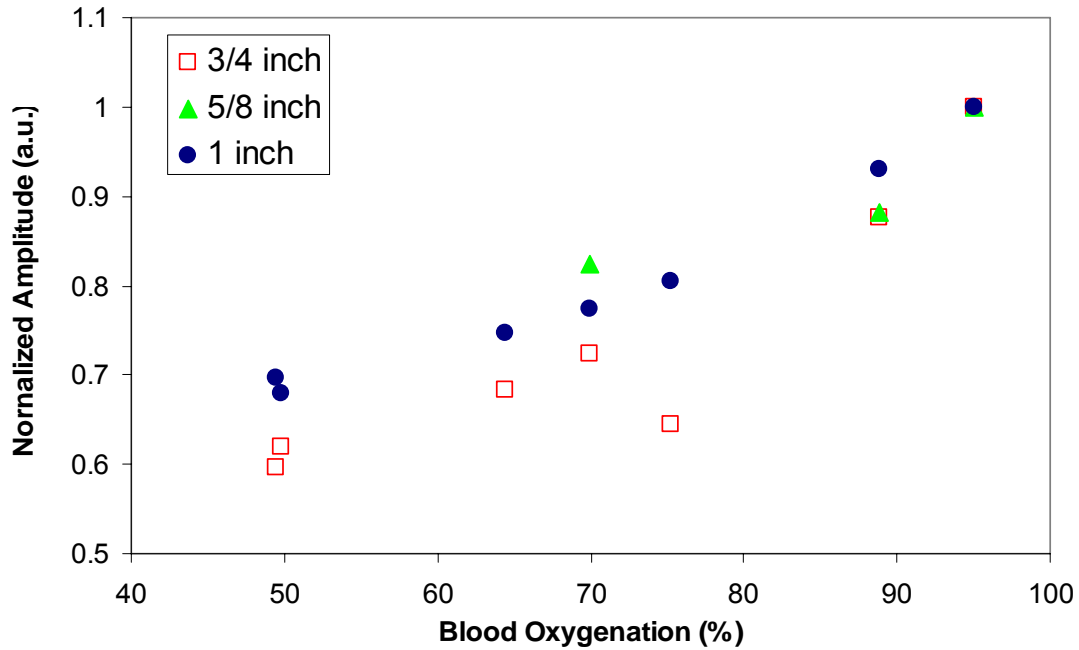


Figure 54: Normalized optoacoustic signal amplitude for jugular phantom of various diameters (15.8, 19.05, and 25.4 mm).

To test the effect of the surrounding medium we used silicone tubes filled with blood with an oxygenation of 94.8%. The surrounding mediums consisted of Intralipid® solutions with water of varying concentrations. Figure 55 shows the effect of the surrounding medium on the optoacoustic signal.

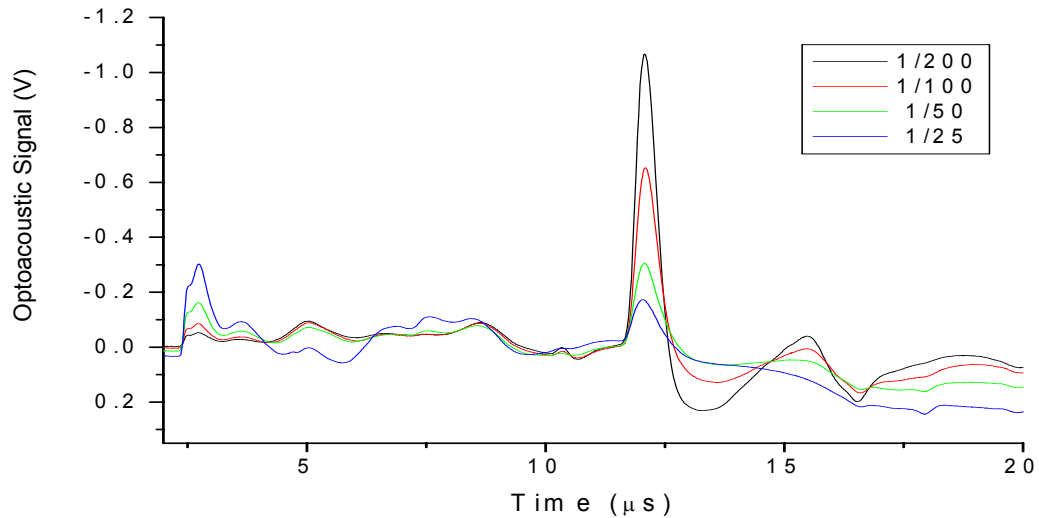


Figure 55: Optoacoustic signals recorded from the 12.7-mm jugular phantom filled with blood ($\text{SaO}_2 = 94.8\%$) surrounded by Intralipid solution of different concentrations (1/200, 1/100, 1/50, and 1/25).

For our usual experiments we used an Intralipid solution at a dilution of 1/100 to simulate connective tissue. This demonstrated that the optoacoustic signal was dependent on the surrounding medium. The majority of the influence was amplitude dependent. An increase in the Intralipid® solution led to an increase in the scattering coefficient. The higher scattering coefficient reduced the amount of light reaching the tube filled with the absorbing solution. This reduction in incident light reduced the optoacoustic signal amplitude.

To exclude amplitude effects the optoacoustic signal was normalized to the minima of the signal. Figure 56 shows the result of this normalization for concentrations from 1/200 to 1/50. There was no minima at the 1/25 concentration so the optoacoustic signal could not be normalized.

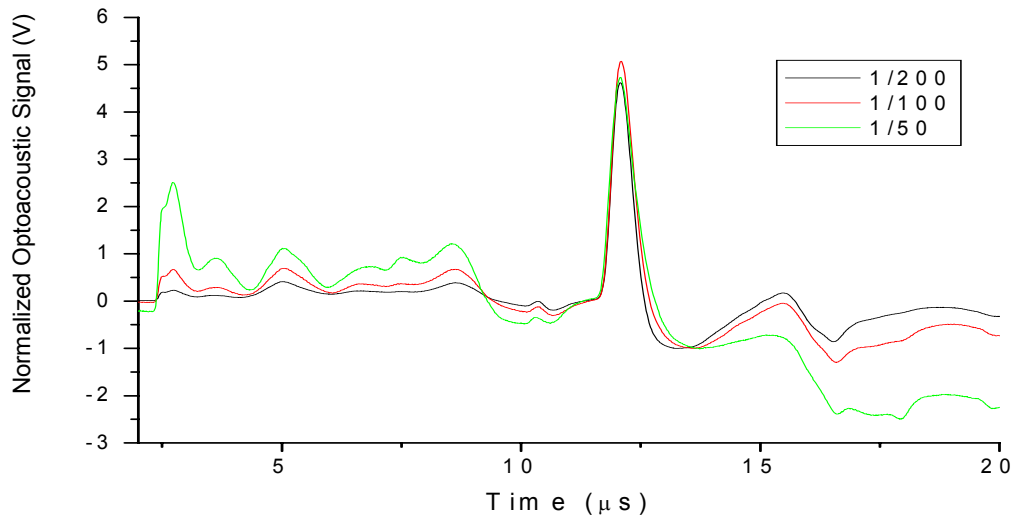


Figure 56: Normalized optoacoustic signals recorded from the 12.7-mm jugular phantom filled with blood ($SO_2 = 94.8\%$) surrounded by Intralipid solution of different concentrations (1/200, 1/100 and 1/50).

The results showed that there are minimal changes in the signal at dilutions of 1/200 and 1/100. The reduction in signal amplitude was due to less light penetration at higher Intralipid® concentrations. Nevertheless, the optoacoustic signal amplitude was altered at lower dilutions (1/50 and 1/25) of the surrounding medium. This finding showed that the temporal profile of the optoacoustic signal was dependent on the optical properties of the surrounding medium if the optical properties change dramatically but remained stable within optical parameters found in tissues.

To test the changes of the optoacoustic signal at lower attenuation coefficients, we used the tube phantoms with diameters of 9.8 mm and 12.7 mm. Variation in the effective attenuation coefficient of the surrounding liquid medium

was simpler than in the solid plastisol phantom. Figure 57 shows the effect of blood oxygenation on the optoacoustic signal.

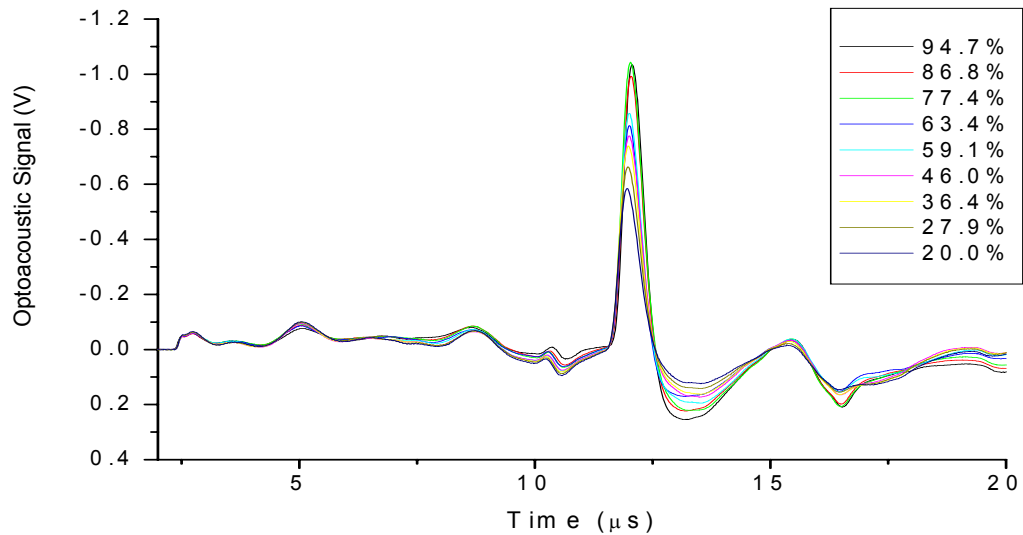


Figure 57: Optoacoustic signals recorded from the 9.8-mm jugular phantom filled with blood of various SO₂ levels surrounded by a 1/100 dilution of Intralipid solution ($\mu_{\text{eff}} = 1 \text{ cm}^{-1}$).

To exclude amplitude effects, the optoacoustic signal was normalized to the minima of the signal. Figure 58 shows the result of this normalization.

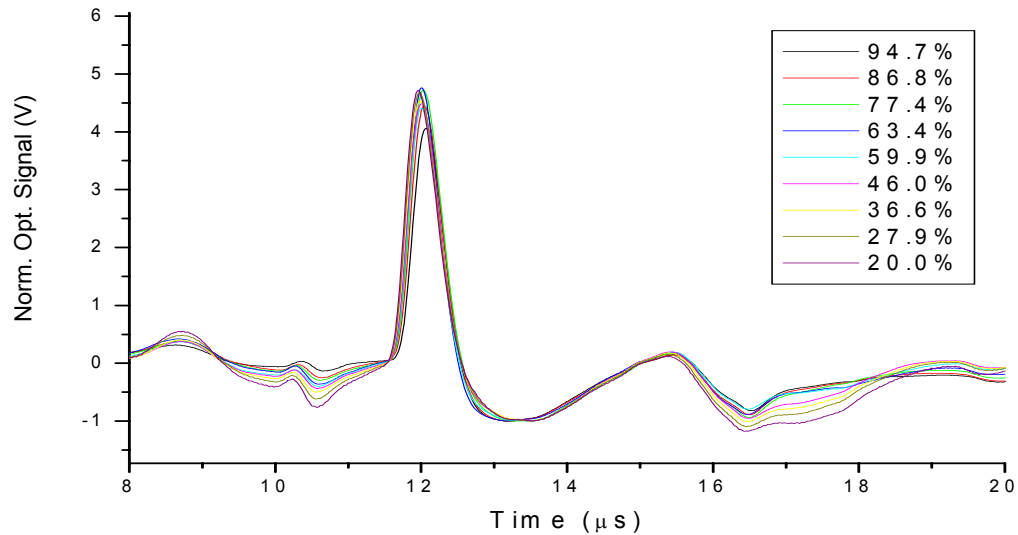


Figure 58: Normalized optoacoustic signals recorded from the 9.8-mm jugular phantom filled with blood of various SO₂ levels surrounded by a 1/200 dilution of Intralipid solution.

Normalizing the minima of the optoacoustic signal to 1 removed any correlation of the slope with blood oxygenation. The lack of correlation was likely due to a suspected reflection of the optoacoustic signal in the 5-mm thick front plate that separated the signal generated from back-reflected light from the signal from the phantom. The application of an exponential fit on the rising slope of the exponential signal did not gain any results. In order to determine any amplitude dependence, the optoacoustic signals were processed in the same manner as the optoacoustic signals from the sheep study. The time after which the value of the integral was determined was extended to 500 points (5 μs) to reduce the effect of the reflection. Figure 59 shows the results of the 1 over Value of Integral method.

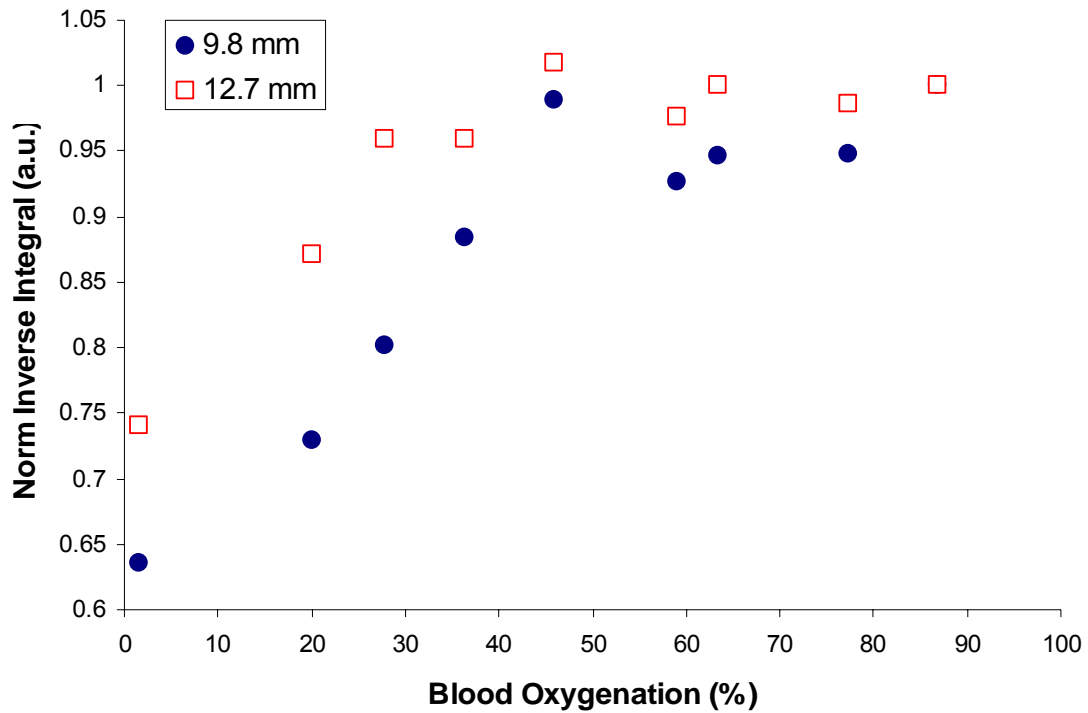


Figure 59: Correlation inverse integral with blood oxygenation for the 9.8- and 12.7-mm jugular phantoms filled with blood of various blood oxygenations surrounded by a 1/200 dilution of Intralipid solution.

There seemed to be a saturation effect in both tubes starting at a blood oxygenation of 46%. The same saturation effect can be detected in the amplitude of the optoacoustic signals. Figure 60 shows the amplitude of the optoacoustic signals of the same experiment. No changes on the frequency response were detected.

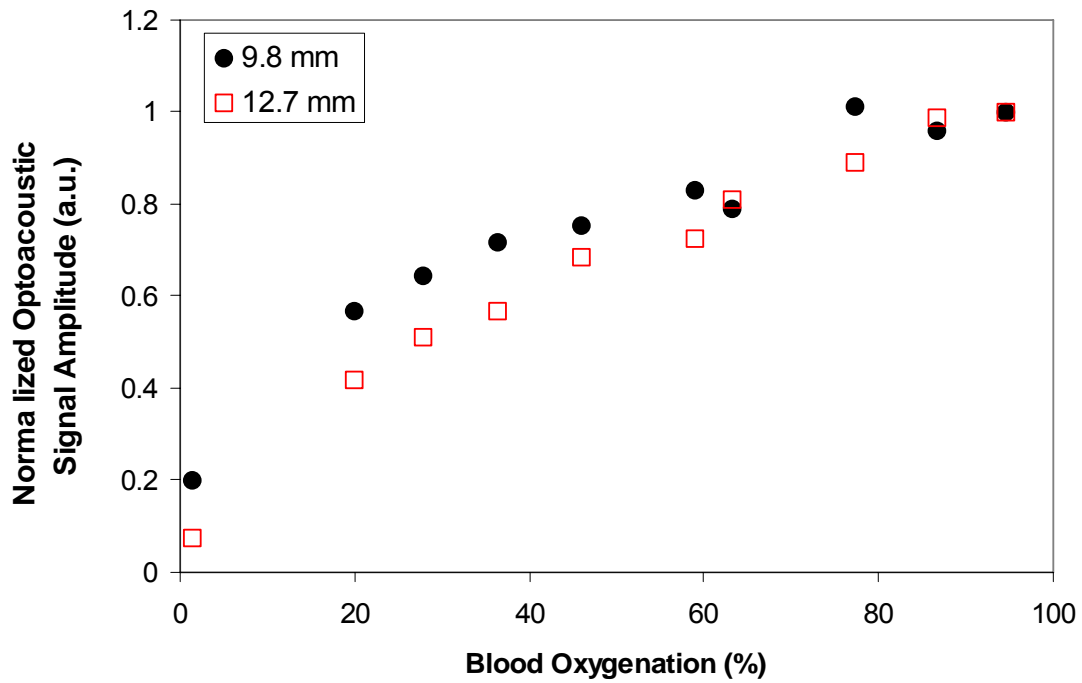


Figure 60: Amplitude correlation of optoacoustic signals with SO_2 for the 9.8- and 12.7-mm jugular phantoms filled with blood of various blood oxygenations surrounded by a 1/200 dilution of Intralipid solution.

CHAPTER 14: IN VIVO STUDIES WITH PVDF PROBE 2 IN VOLUNTEERS

Experimental Setup

The optoacoustic setup consisted of an Nd:YAG laser (Ultra CFR, Big Sky Technologies, Inc., Bozeman, MT) at a wavelength 1064 nm with pulse duration of 5 ns. The laser pulse was then coupled into an optical fiber, which directed the light to the optoacoustic probe. The optoacoustic probe was varied throughout the experiments. The optoacoustic signal collected from the probe was then amplified using pre- and secondary amplifiers and then acquired with a 2 Channel 100 MHz digitizer (NI 5112, National Instruments Corp., Austin, TX) and stored on the laptop computer using a LabView[®] program developed in our laboratory.

The preamplifier used in our system was a 17 dB low-noise hydrophone preamplifier (Specialty Engineering Associates, AH-17DB), which was powered by batteries to reduce noise. The nominal voltage gain was 17 dB into 50 Ω . The input impedance was 1 M Ω in parallel with a capacitance of 20 pF. The frequency range of the preamplifier was from 5 kHz to 25 MHz [⁵³].

The secondary amplifier was a bipolar low noise amplifier (Model 322, Analog Modules, Inc. Longwood, FL), which was powered by a bench-top power supply. The nominal voltage gain was 40 dB with a bandwidth from 100 Hz to 10 MHz. The input and output impedance was 50 Ω . The noise was 280 pV/ $\sqrt{\text{Hz}}$.

Healthy volunteers were placed in a supine position with the head tilted down approximately 15 to 20 degrees. The probing area was first imaged using a

conventional ultrasound machine (B&K Medical systems Inc. Marlborough, MA Model 3535) and the same location was used to generate the optoacoustic signals. The optoacoustic probe with the silicone spacer was attached to the volunteer by hand. Scanning was not performed due to the long time duration required to perform the scan. Three hundred optoacoustic signals were collected and averaged. Figure 61 shows the ultrasound image of the external jugular vein (EJV) of a healthy female volunteer and the corresponding optoacoustic signal [a) and b) respectively]. The external jugular vein collects facial blood. It is very broad and at a shallower location than the internal jugular vein and therefore very accessible.



Figure 61a: Ultrasound image of the external jugular vein of a female healthy volunteer.

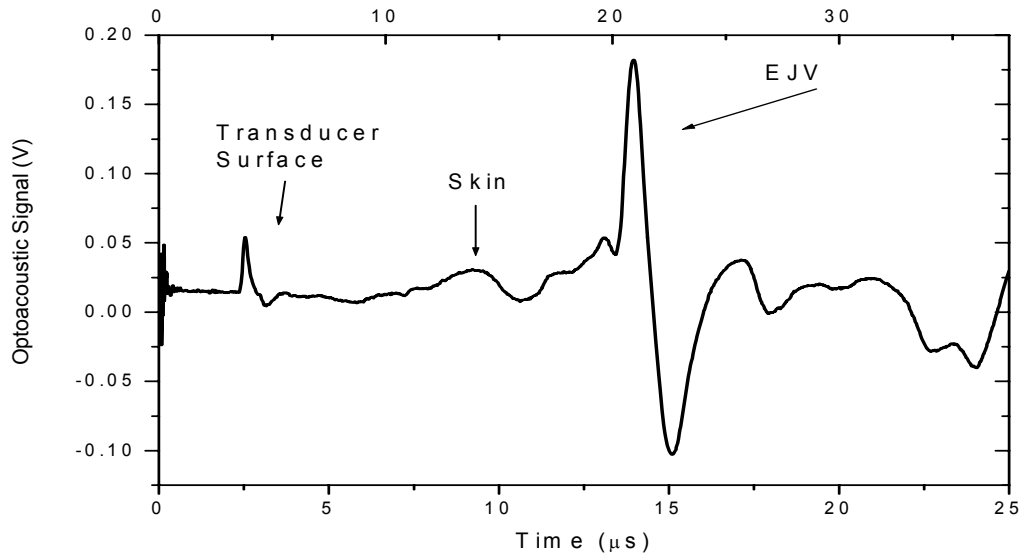


Figure 61b: Corresponding optoacoustic signal measured from the external jugular vein of a healthy female volunteer.

The shape of the optoacoustic signal from the EJV was very similar to the optoacoustic signals generated by the phantom in a 1/100 and 1/200 dilution of Intralipid[®] solution. This showed that the influence of the surrounding medium is relatively low at the wavelength of 1064 nm, and that the 1/100 dilution of Intralipid[®] can be used to simulate surrounding tissue. The signal and ultrasound picture were taken at the same location at the base where the EJV bifurcates. This bifurcation resulted in a very wide and plane geometry ideal for taking optoacoustic measurements.

The exponential coefficient derived from this signal was three which corresponded to a blood oxygenation of about 70% (Figure 43). Figure 43 contains *in vitro* data from a blood vessel phantom with similar dimensions and additional data on the effect of displacement of the probe. The optoacoustic probe was placed by hand which resulted in possible lateral misalignment between probe and blood vessel.

Figure 62 shows the ultrasound image of the internal jugular vein (IJV) of a healthy female volunteer and the corresponding optoacoustic signal [a) and b), respectively].

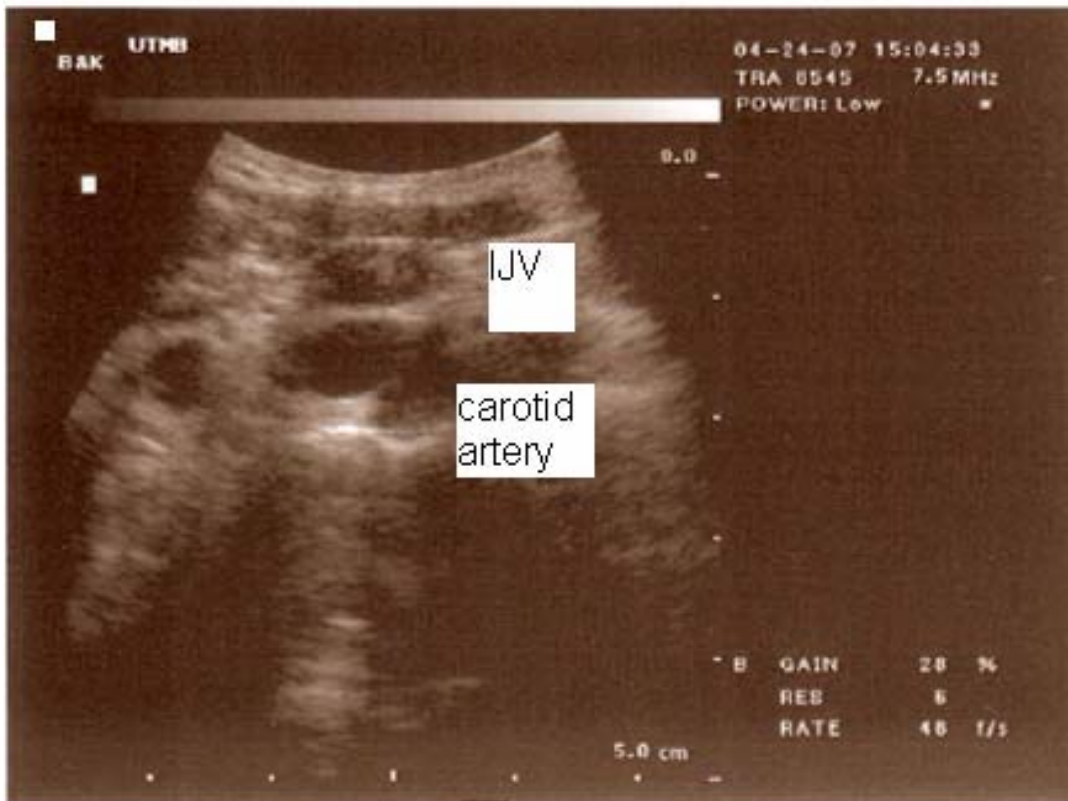


Figure 62a: Ultrasound image of internal jugular vein of a healthy female volunteer.

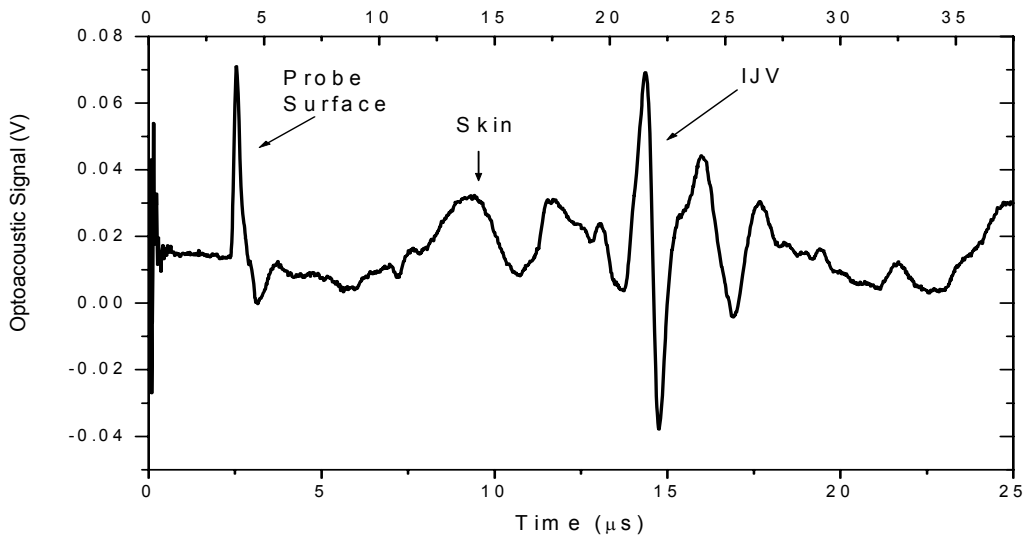


Figure 62b: Corresponding optoacoustic signal measured from the internal jugular vein of a healthy female volunteer.

The ultrasound image of the female volunteer shows the IJV with a diameter of about 7 mm superior to the carotid artery. The carotid artery was clearly detectable in the ultrasound image due to its pulsation. The optoacoustic signal measured at the same location was clearly visible but there was an additional peak just after the peak from the IJV. This peak may have resulted from a reflection of the signal in the silicone spacer caused by an air bubble in the ultrasound gel. The second peak prevented the application of an exponential fit.

Figure 63 shows the ultrasound image of the IJV of a healthy male volunteer and the corresponding optoacoustic signal [a) and b), respectively].

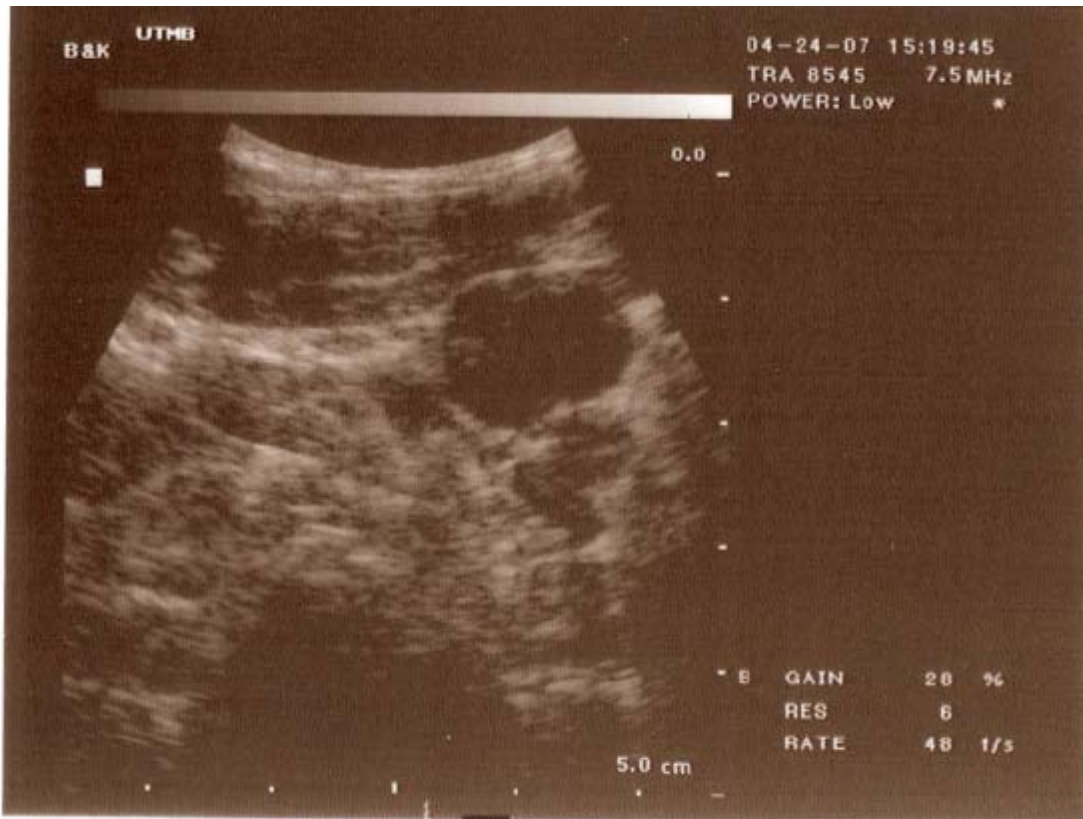


Figure 63a: Ultrasound image of internal jugular vein of a male healthy volunteer.

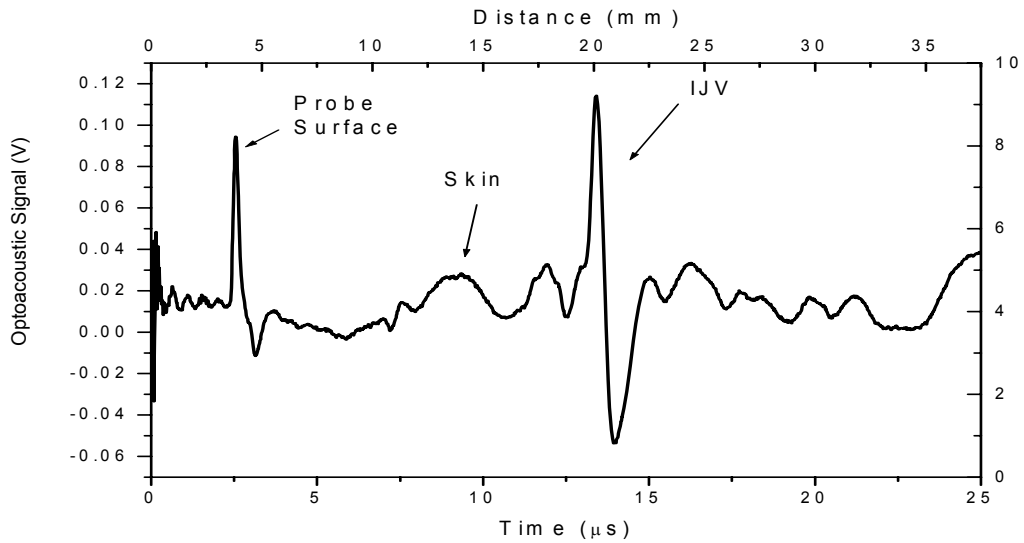


Figure 63b: Corresponding optoacoustic signal measured from the IJV of a healthy male volunteer.

The ultrasound image of the male volunteer shows the IJV with a diameter of approximately 13 mm superior to the carotid artery. The carotid artery was half the size of the IJV but still clearly detectable due to its pulsation. There was no additional peak just after the peak from the jugular vein. The larger size of the IJV blocked light from reaching the carotid artery thereby preventing generation of a signal from the carotid artery. The exponential coefficient measured from this signal was two which correlated to a blood oxygenation of 60% (Figure 43). The value of blood oxygenation was 60%, which is normal for the IJV. Since the optoacoustic probe was placed above the IJV by hand, potential lateral misalignment may have altered the value of the signal.

The system was capable of detecting optoacoustic signals from the external and internal jugular veins correlating with ultrasound pictures taken at the same location.

CHAPTER 15: DISCUSSION

The amplitude and temporal profile of the optoacoustic signal correlated with the absorption coefficient and blood oxygenation obtained with all three probes.

Sheep provide a good model for measuring blood oxygenation in large blood vessels. We used the external jugular vein instead of the internal jugular vein, but since blood oxygenation was monitored globally by changing the fraction of inspired oxygen.

Initial studies in volunteers showed the feasibility of blood oxygenation measurements in humans.

Piezoceramic probe:

Phantom studies revealed the effects of vertical and lateral displacement on the optoacoustic signal. Silicon spacers separated the optoacoustic signal generated in the phantom from the electrical noise generated by the power supply.

The results of the *in vivo* studies indicated that there is a strong qualitative correlation between the amplitude of the optoacoustic signals and the actual blood oxygenation. However, the amplitudes of the signals cannot be used for accurate monitoring of blood oxygenation. The optoacoustic signal amplitudes were dependent on the laser fluence reaching the blood vessel which varied between test subjects. The correlation between amplitude and attenuation coefficient would have to be established for every test subject and alignment.

Therefore, the amplitude measurements alone would not be practical due to the intersubject variability.

The inverse integral method provided high correlation with blood oxygenation. It was less prone to motion artifacts (probe misalignment) and properties of overlying tissues. The higher degree of correlation of the signal at 1064 nm for the amplitude and value of integral measurements resulted from the time delay between optoacoustic measurement and blood sampling. Optoacoustic measurements were generally taken first at 700 nm, then at 800 nm, and last at 1064 nm. Three minutes were required to complete the measurements at all three wavelengths. The blood sample for the measurement of the actual blood oxygenation was acquired immediately after the measurement at 1064 nm. Since blood oxygenation in the sheep was changed by varying FiO_2 , blood oxygenation changed quickly. This contributed to inaccuracy of the measurements, in particular at 700 nm.

While improving reliability for a single subject, the analysis of the inverse integral did not reduce the effects of intersubject variability. One possible reason is the small overall change of the inverse integral over the whole range of blood oxygenation. A data processing algorithm that yields greater overall change would be less sensitive to the offset experienced when combining the ratios of the inverse integral from all sheep.

The temporal profile of the optoacoustic signals could display less ringing if a PVDF-based piezo-element was used because it is not a crystal. The absence of ringing would allow exponential fitting for the measurement of the blood effective attenuation coefficient thereby simplifying signal processing [27]. However, the PVDF transducer might be less sensitive than the piezo ceramic one used in this work.

PVDF Probe 1

The PVDF probe has a wider frequency bandwidth in comparison with the piezo ceramic probe and the optoacoustic signals have no oscillations. Figure 64 shows the frequency bandwidth of both probes.

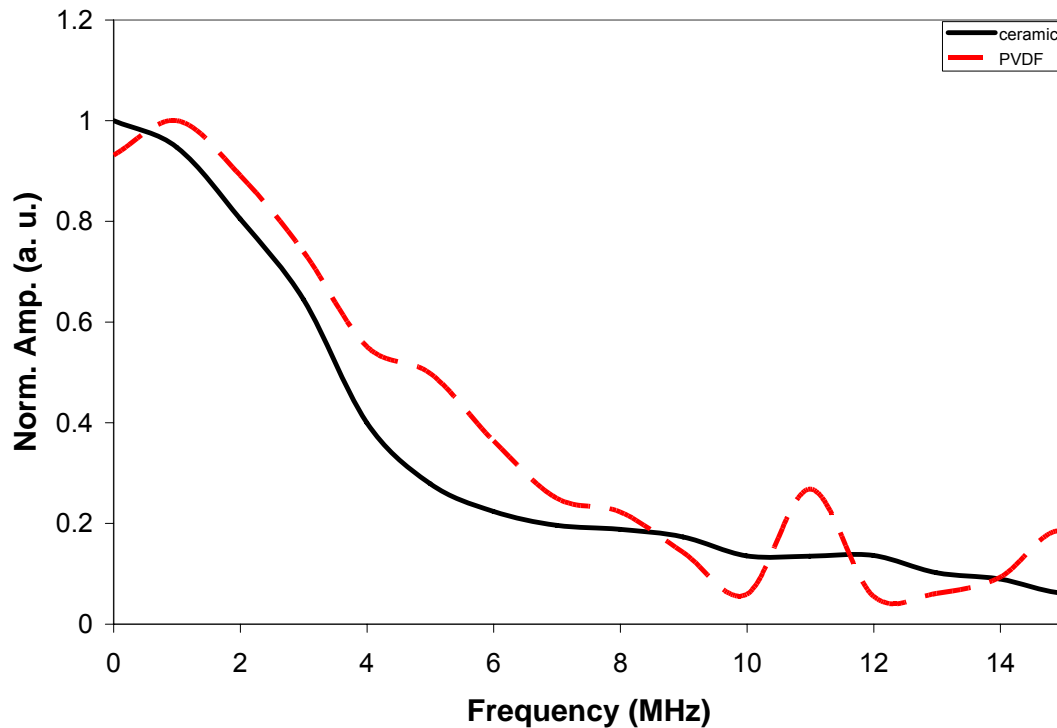


Figure 64: Voltage spectrum of optoacoustic signal measured from 2-mm thick black rubber with very high absorption coefficient using the piezo ceramic and PVDF probes.

This allowed the application of an exponential fit to the decay of the bipolar-shaped optoacoustic signal without distortion due to ringing.

The exponential fitting of the optoacoustic signals generated in the jugular vein showed good correlation with the absorption coefficient in the phantom and

with the blood oxygenation in sheep blood used in the *in vitro* studies. The dependence of the exponential coefficient on tube diameter was greater in blood compared to those in the naphthol green solution. One possible explanation is the difference between blood and the naphthol green solution. Whereas the naphthol green solution was purely absorbing, the sheep blood was scattering and absorbing. The effective attenuation coefficient of sheep blood is dependent on the absorption coefficient μ_a , the scattering coefficient μ_s and the anisotropy factor g (Equation 8). The lower absorption coefficient of blood and its higher scattering coefficient may explain the difference observed in the exponential coefficient between the two tube sizes in the *in vitro* studies.

The lower absorption coefficient increased the penetration depth of the light pulse; therefore, illuminating a larger area of the blood vessel. Figure 65 shows the effect of the absorption coefficient on blood vessel illumination generated in a computer model [^{42,72,73}].

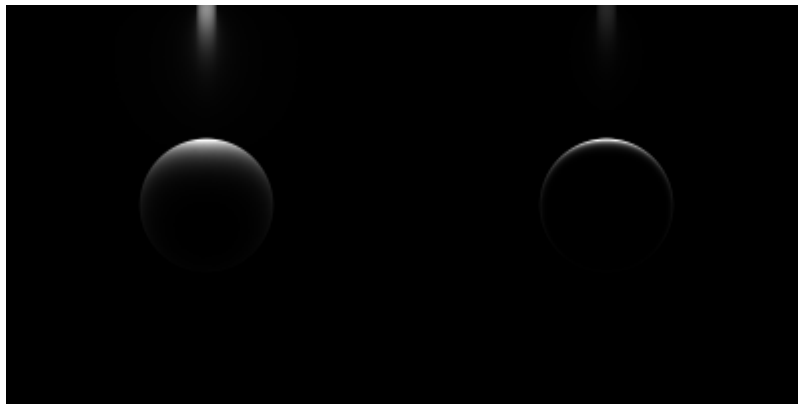


Figure 65: Computed illumination of a 10-mm diameter blood vessel with an absorption coefficient of 5 cm^{-1} (left) and 30 cm^{-1} (right).

The effect of the curvature of the phantom vessels at lower attenuation coefficients was more pronounced whereas at a higher attenuation coefficient the geometry remained planar. A probe with a smaller angle of acceptance would

capture optoacoustic signals from a smaller portion of the blood vessel and might provide better results and less dependence on the diameter of the phantom.

The exponential fit was less dependent on lateral displacement in comparison with amplitude measurements. It also showed greater change with blood oxygenation, which allowed for higher accuracy of blood oxygenation measurements.

The PVDF probe showed higher sensitivity to the signal generated by light reflected back to the transducer despite a layer of electrolytically deposited gold as optical shielding. This unwanted signal could be removed by subtraction of a baseline signal obtained with water in the jugular vein phantom in order to increase accuracy of the measurements. Better optical shielding and a polycarbonate spacer between the optical and electrical shielding would separate and decrease the background signal and eliminate the need for subtraction of the water signal.

The scanning system allowed a quick, computer-controlled scan across the phantom with a pre-determined number of steps and distance between these steps. The optoacoustic signal with the maximal amplitude corresponding to the best probe-vein alignment could be selected and used for further processing. This eliminated the influence of lateral misalignment on the accuracy of the measurements.

PVDF Probe 2

The third PVDF probe featured a large active area of about 40 mm² that made the probe very sensitive. Optoacoustic signals from a 6.35-mm tube surrounded by a 1/100 dilution of Intralipid® solution could be clearly detected at

an incident laser pulse energy of 60 μJ out of the fiber. This was the threshold level for the maximal permissible exposure for ocular exposure ($\text{MPE}_{\text{ocular}}$).

The larger ring showed no smaller angle of acceptance. The polycarbonate disk separated the signal generated from light that is reflected back into the probe and eliminated the offset from the pyroelectric effect in the PVDF material. This eliminated the need for baseline subtraction and allowed *in vivo* studies. Unfortunately, the polycarbonate disk generated a reflection that made exponential fitting starting from the minima of the signal difficult. An increase in thickness of the polycarbonate disk might delay the reflection to a region where the temporal profile of the signal is not influenced. The system was capable of detecting optoacoustic signals from the external and internal jugular veins correlating with ultrasound pictures taken at the same location.

Further Development of the Optoacoustic System

DATA ACQUISITION

The Nd:YAG laser was very stable in laser output power. No variation in output power was detected between the beginning and the end of the experiment where laser output power was measured. The output power of the OPO varied for different wavelengths and at one wavelength over time due to thermal instability of the OPO. Future multi-wavelength measurements should be taken with a more stable laser source. Another possibility is the monitoring of the output power of the OPO to allow for later normalization. A fraction of the laser beam can be diverted and the power of every pulse can be recorded with the second channel of our data acquisition system. Currently a number of signals are averaged and only the average of the signal is saved. By recording every signal and recording the corresponding laser pulse energy we can normalize for the laser output and determine the variation induced by the changes in laser output power.

PROBE

The integration method and the exponential fit are dependent on the offset of the exponential signal. There are two sources of offset of the optoacoustic signal.

The first source is the contribution of the optoacoustic signal in the probe due to signal generation from back-reflected light or due to reflections in the probe that interfere with the optoacoustic signal. This offset can be managed by

using custom coatings with a reflectivity of 99.9%. Such a coating would reflect all light back into the tissue and would eliminate the signal generated in the probe. The reflections inside the transducer can be avoided by the use of a new material. It is a conglomerate of rubber pieces and hollow glass beads in an epoxy matrix. Its acoustic impedance can be matched to the PVDF material to avoid reflections. Additionally its heterogeneous structure of rubber pieces and hollow glass spheres scatter the ultrasound wave and absorb it. The use of this new backing material would minimize reflections within the transducer.

The second source is the contribution of the surrounding material to the optoacoustic signal collected by the probe. This contribution can be minimized by further reducing the angle of acceptance and limiting the temporal window for the data processing to the region where the signal is generated.

The data and experience regarding the effect of lateral displacement generated with the scanning system can be used to build an optoacoustic transducer array that simultaneously captures a number of signals and automatically selects the signal at 0 displacement. This would reduce the time for the acquisition and prevent loss of contact between the optoacoustic probe and tissue due to the scanning.

OTHER DATA PROCESSING ALGORITHMS

The inverse integral and the application of an exponential fit are both offset-dependent data processing methods. In our current data processing algorithm, the offset recorded in the time delay from the silicone or polycarbonate spacer is recorded and subtracted from the signal. While future probes can greatly reduce the offset generated in the probe itself, the offset generated in the tissue surrounding the blood vessel will remain constant and lead to intersubject

variability. Further studies are necessary to quantify the influence of the surrounding medium on the temporal profile of the optoacoustic signals.

Another possibility is the application of offset-independent data processing algorithms like the changes in the frequency response. The idea is based on the increase in the central frequency with an increase in the effective attenuation coefficient (Table 1).

The correlation between the frequency spectrum of the optoacoustic signals from blood vessels and the attenuation coefficient was determined. The optoacoustic signal from the blood vessel was selected and the voltage spectrum analysis was performed using LabView[®] software. As the absorption coefficient increases, the peak of the power spectrum should shift to a higher frequency and the power spectrum should become wider. The frequency approach was tested with the *in vivo* studies in sheep performed with the piezo ceramic probe. The power spectrum of the optoacoustic signal generated in the EJV was calculated using LabView[®] software. Figure 66 shows the power spectrum of one of the experiments for three different blood oxygenations (94.8, 64.1, and 16.3%) at the wavelength of 700 nm. The effective attenuation coefficient of blood increased with decreased oxygenation at 700 nm.

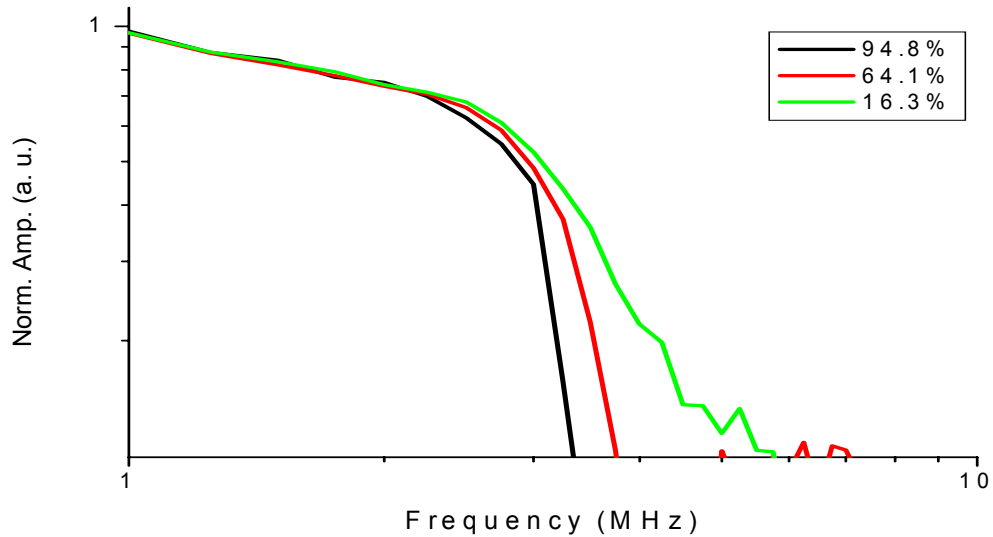


Figure 66: Power spectrum of the optoacoustic signal derived from the external jugular vein of sheep for three different blood oxygenations (16.3, 64.1, and 94.8%) at the wavelength of 700 nm.

The sheep data was sampled at 100 Ms which allowed determination of the voltage spectrum up to 50 MHz. At 700 nm the effective attenuation coefficient increased with an increase in blood oxygenation. The power spectrum widens with a decrease in blood oxygenation (increase in μ_{eff}). Figure 66 uses a log scale for both axes. The slope at the higher blood oxygenation (low μ_{eff} at 700 nm) is much steeper than the slope for low blood oxygenation (high μ_{eff} at 700nm).

The same data processing algorithm was then tested in the phantom using the first PVDF probe. The signal generated from the phantom was selected and the optoacoustic signal was normalized to the negative peak of the bipolar signal and the power spectrum determined.

Figure 67 shows the power spectrum of the optoacoustic signals shown in Figure 43.

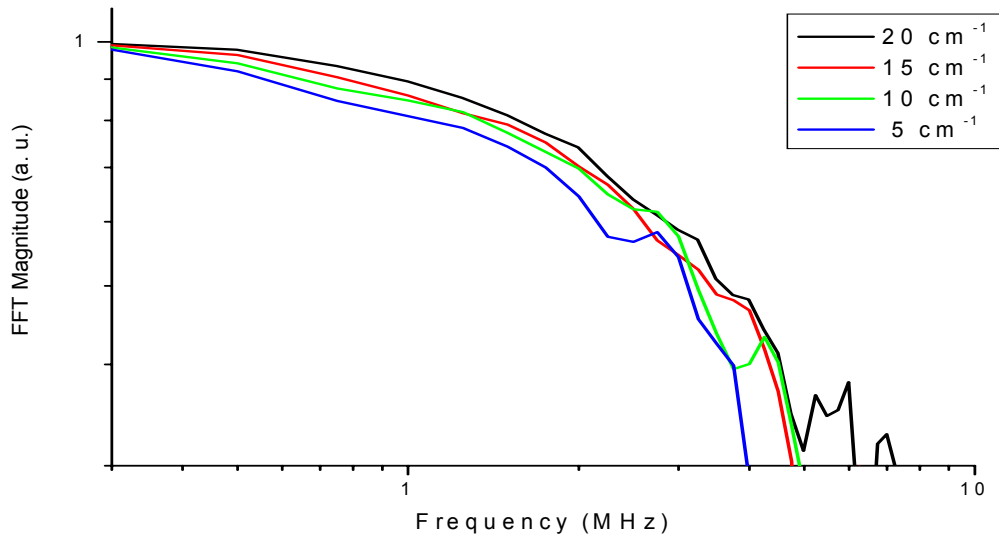


Figure 67: Power spectrum of the optoacoustic signal derived from the 9.8-mm jugular vein phantom filled with absorbing solution (5, 10, 15 and 20 cm^{-1}).

Figure 67 uses a log scale for both axes. The slope at the higher absorption coefficient ($\mu_a = 20 \text{ cm}^{-1}$) is not as steep as the slope for low absorption coefficient ($\mu_a = 5 \text{ cm}^{-1}$), but the curves are closer together than in the previous *in vivo* studies.

The Fourier transform of an exponent is an exponent correlating to the original exponent. In prior data processing algorithm we took the derivative of the exponent. The derivative of an exponent is an exponent with the same exponential coefficient. It worked well for simulated signals but taking the derivative of real signals amplified the noise and rendered the data processing method unusable. By applying the Fourier transform we can gain the same offset independence that we achieved by taking the derivative without the negative influence of high frequency noise.

Figure 68a shows the exponential decay of the optoacoustic signals shown in Figure 43, and Figure 68b shows the corresponding power spectrum.

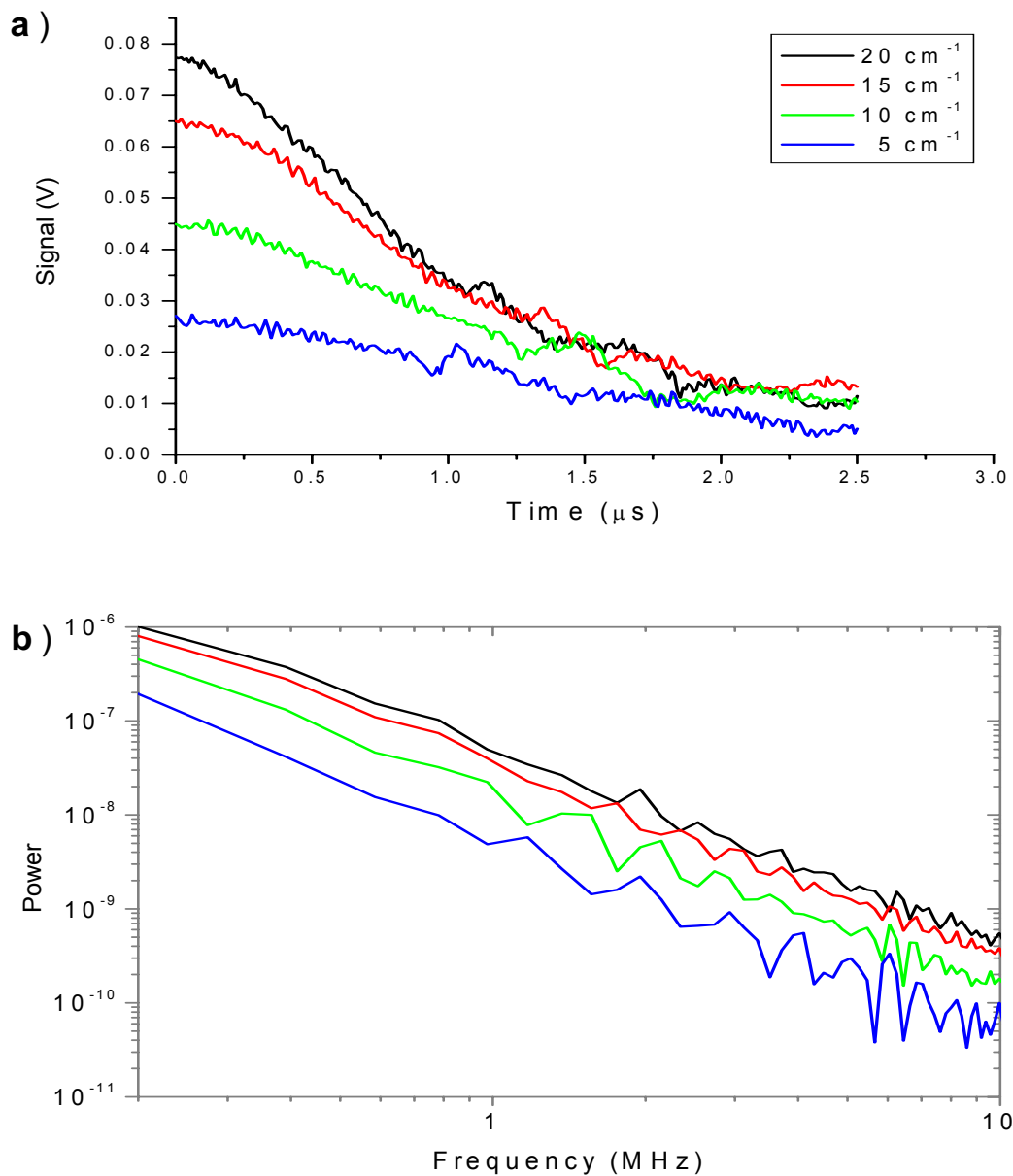


Figure 68: a) Exponential decay of the optoacoustic signals from the phantom studies (Figure 43); b) Power spectrum of the exponential decay of the optoacoustic signal derived from the 9.8-mm jugular vein phantom filled with absorbing solution (5, 10, 15 and 20 cm^{-1}).

By switching from the time to the frequency domain, new data processing algorithms can be developed that are amplitude and frequency independent.

CHAPTER 16: CONCLUSION

Three optoacoustic probes were evaluated for their performance to accurately determine blood oxygenation in large blood vessels. The piezo ceramic and the large ring PVDF probe were the most sensitive. The large active area of the PVDF probe of 40 mm^2 was able to accurately capture optoacoustic signal from phantom at incident laser energy of $60 \text{ }\mu\text{J}$. The piezo ceramic probe was capable of accurately capturing signals at the same energy level. Although the least sensitive, the small ring PVDF probe showed the widest bandwidth, and no reflections or oscillations inside the probe. It required about $600 \text{ }\mu\text{J}$ of incident laser energy (10 times the limit for ocular exposure: safety goggles required).

The scanning system eliminated the effect of lateral displacement and helped to determine necessary specifications of a future array-type probe (elements can be 1 mm apart).

This study showed that the tail-end of the bipolar optoacoustic signal could be used to extract information of the optical properties of the measured subject. The value of the integral and the exponential fit methods both correlated with changes in the absorption coefficient and therefore blood oxygenation. Normalization to the minima of the optoacoustic signals removed amplitude dependence and limited the effect of the influence of the surrounding tissue on the optoacoustic signals. The determination of the exponential coefficient provided greater range and potentially higher resolution. Additionally it was resistant to lateral displacement. The greater range (20 times) provided a better correlation coefficient and appeared to be the more accurate data processing algorithm. Unfortunately, it was vulnerable to reflections and oscillations. We

were able to successfully apply it in the second small ring PVDF probe. The inverse integral method was successfully applied in all three probes and was working with a greater variety of probes.

Despite being described as early as 1880, the optoacoustic technique has only recently become a topic of intense biomedical research. Wideband optoacoustic probes are not yet commercially available and probes are custom made. Due to the variation of the hand-made probes, the data processing algorithm will need to be tailored to the probe used in the experiment.

Nevertheless, the optoacoustic technique is a promising tool to monitor blood oxygenation in large blood vessels.

GLOSSARY

Delta Signal – Short pulse with the shape of the Greek letter Δ .

Hemoglobin Saturation – Percentage of oxygen saturation of hemoglobin.

Hematocrit – The hematocrit is a measure of the proportion of blood volume that is occupied by red blood cells.

Isosbestic point – In spectroscopy, an isosbestic point is a specific wavelength at which two (or more) chemical species have the same absorptivity.

Laser – Laser is an acronym for: Light Amplification by Stimulated Emission of Radiation.

Piezo-electricity – Greek Piezo = pressure, conversion of pressure into voltage. A piezo-element can electrically be seen as a voltage generator in series with a capacitor.

Probe – The probe is the complete optoacoustic probe consisting of piezo – element, optical fibers for illumination, backing, electrical shielding and preamplifier.

Transducer – The active element (piezo-element).

APPENDIX

In Vivo studies in sheep (Additional Graphs)

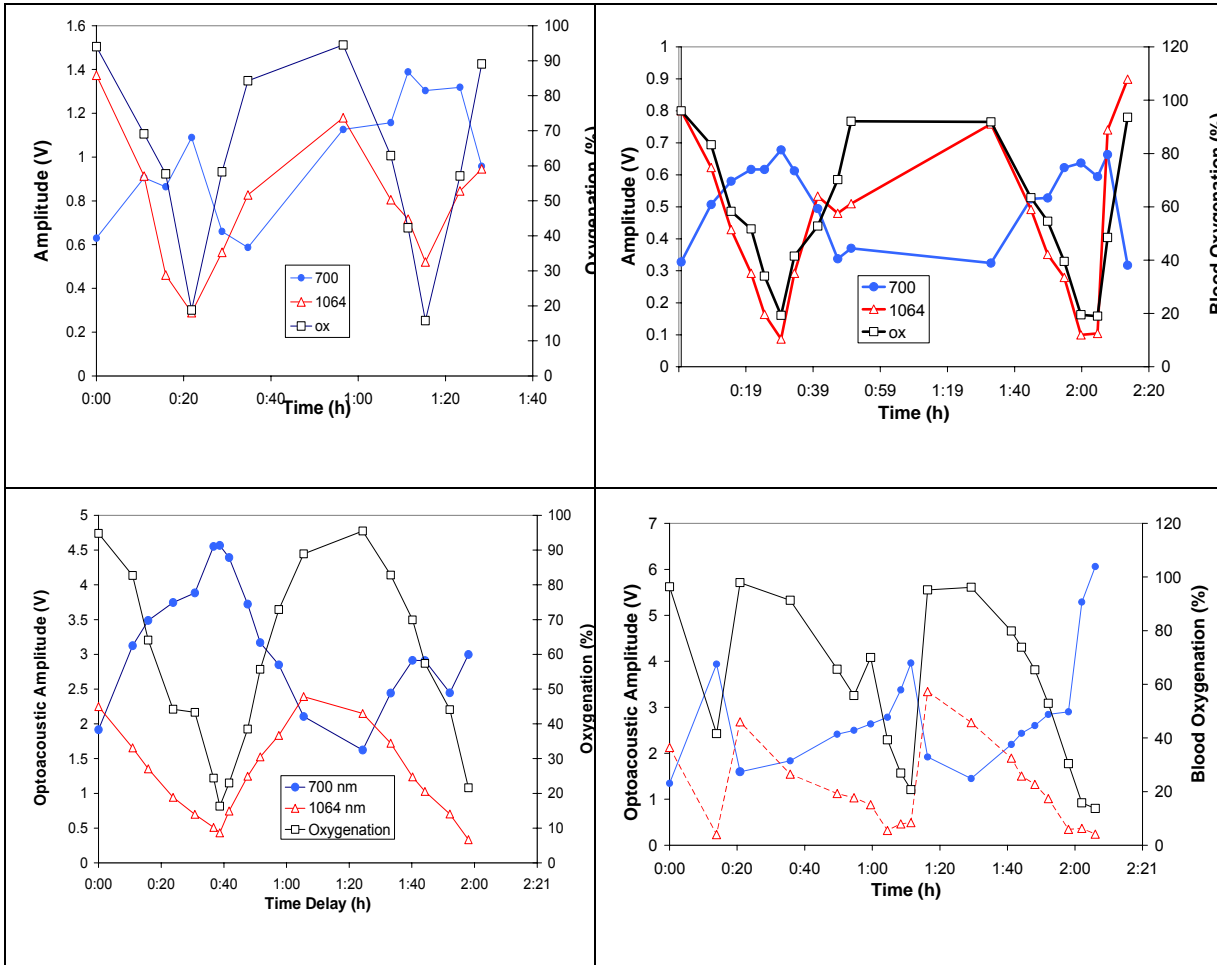


Figure 69: Time course of optoacoustic signal amplitudes at 700 nm (blue filled circles) and 1064 nm (red triangles) with respect to blood oxygenation (black squares).

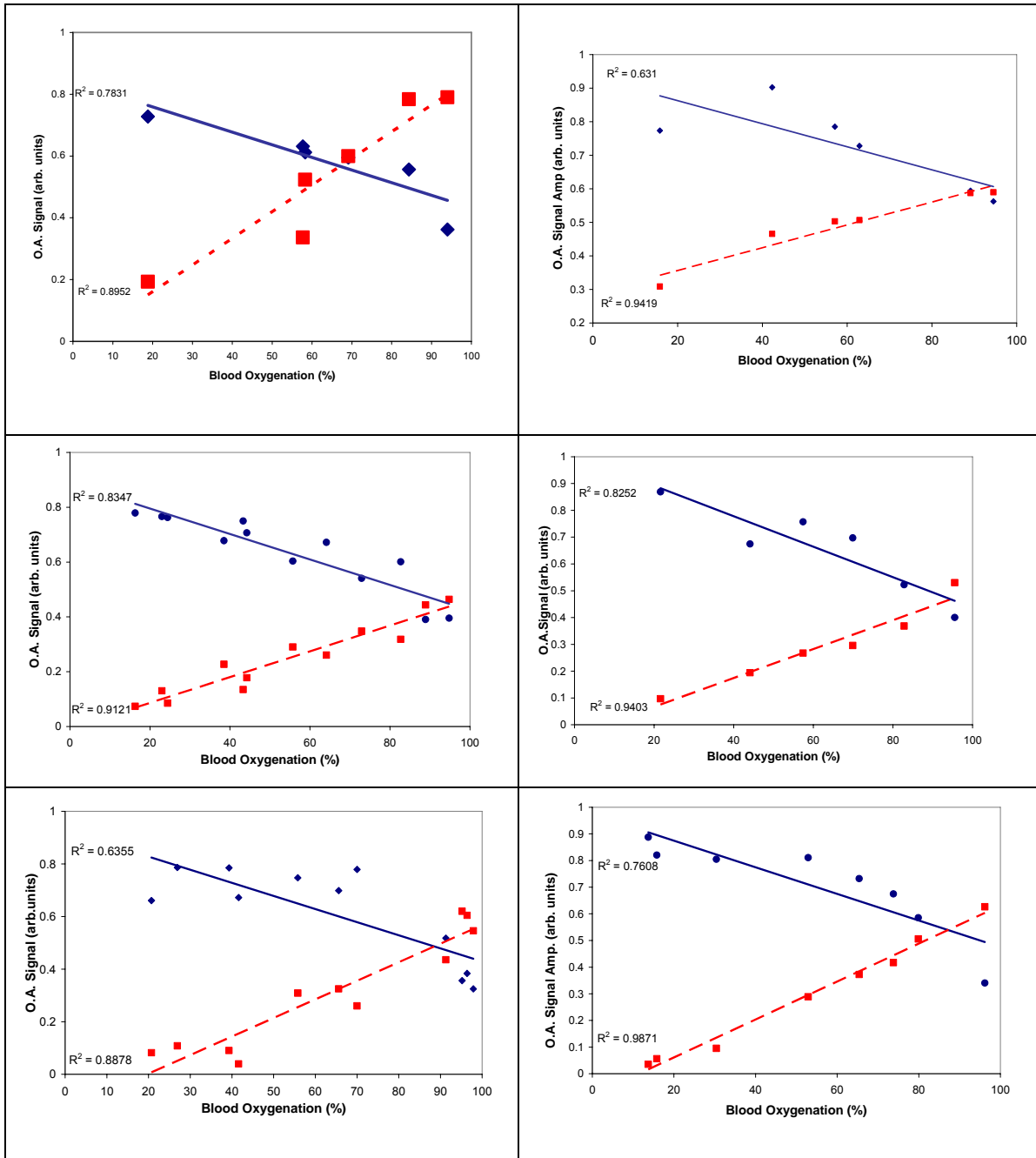


Figure 70: Optoacoustic signal amplitudes at 700 nm (blue filled circles) and 1064 nm (red empty squares) corrected with the optoacoustic signal amplitude at 800 nm for variations in incident laser power.

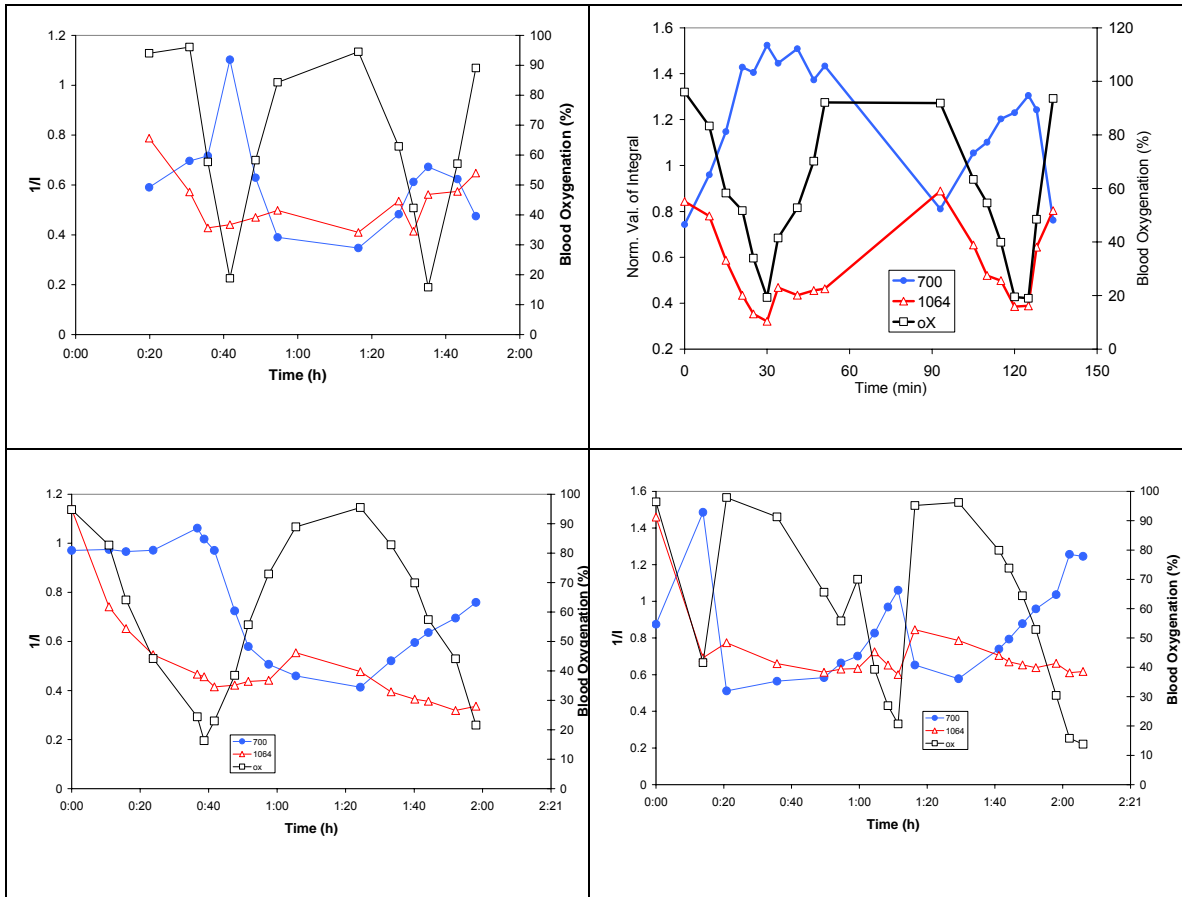


Figure 71: Time course of utilizing temporal profile at 700 nm (blue filled circles) and 1064 nm (green triangles) with respect to blood oxygenation (black filled diamonds). Graph shows both cycles.

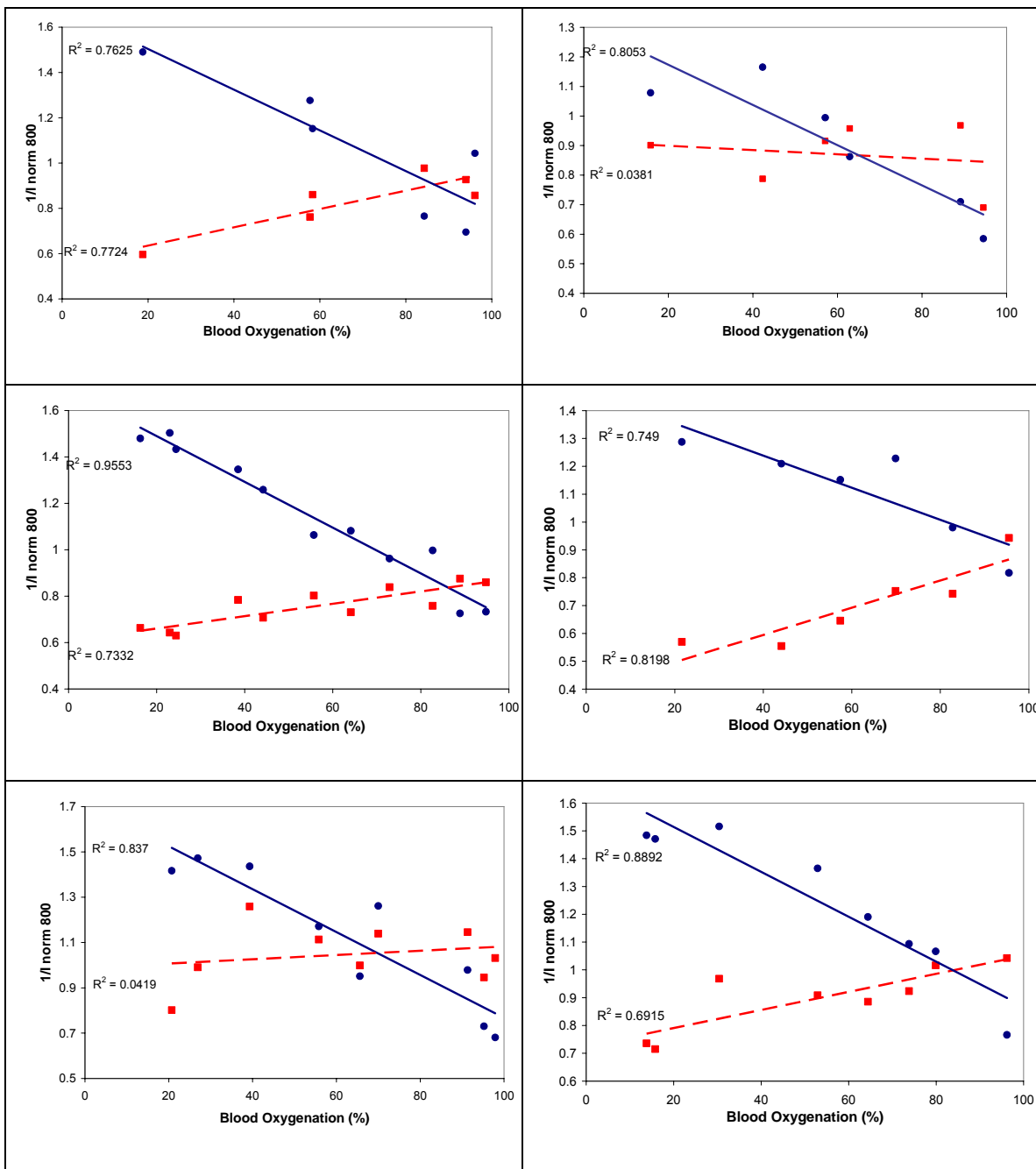


Figure 72: Correlation of temporal profiles with blood oxygenation at 700 nm (blue filled circles) and 1064 nm (red squares) corrected for variations in incident laser power. Graph shows all 4 sheep top to bottom and first cycle (left) second cycle (right).

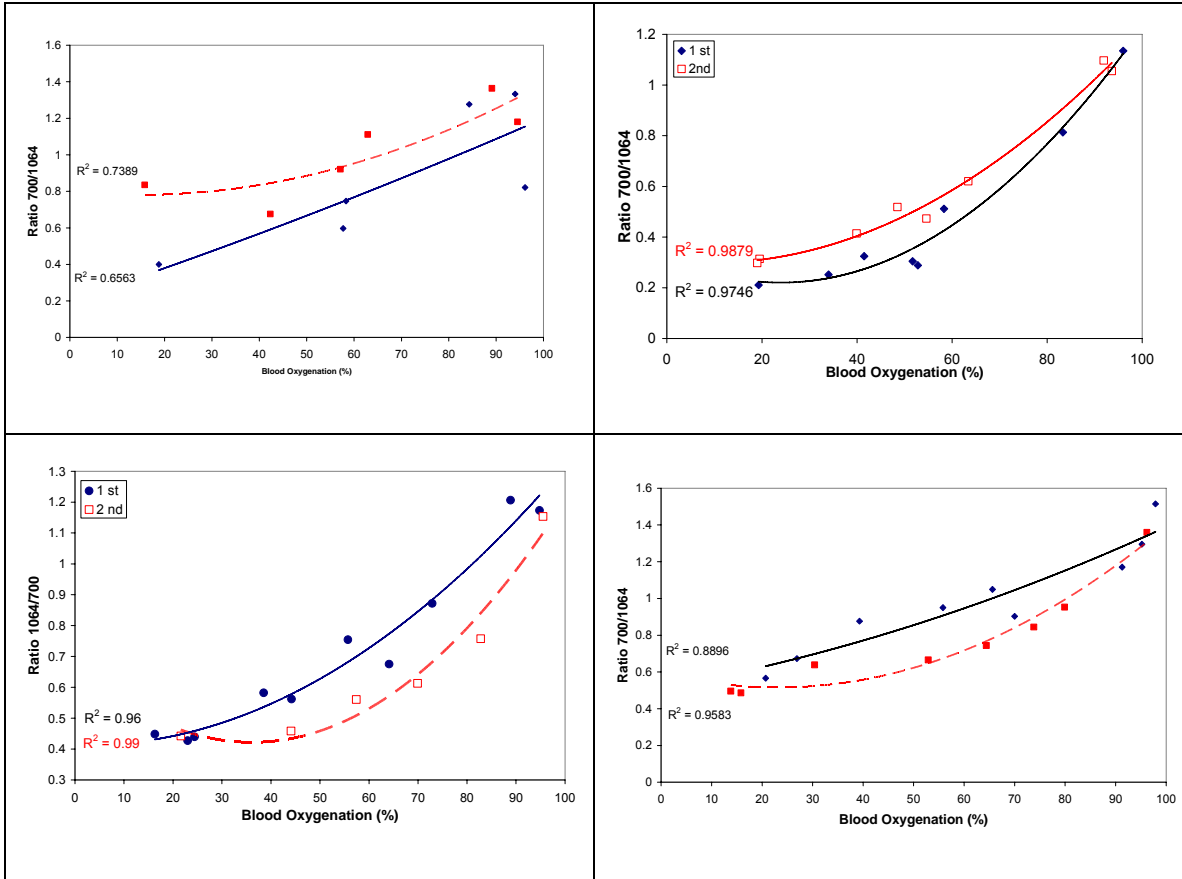
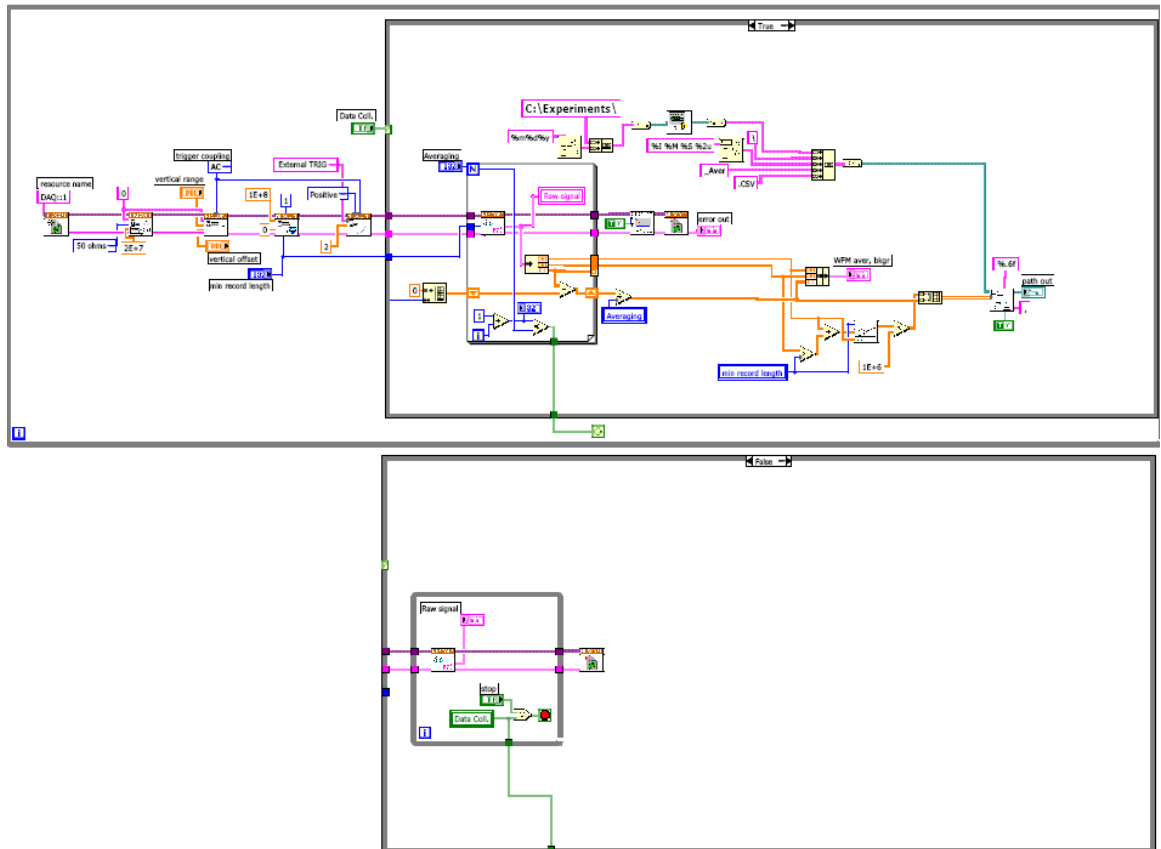


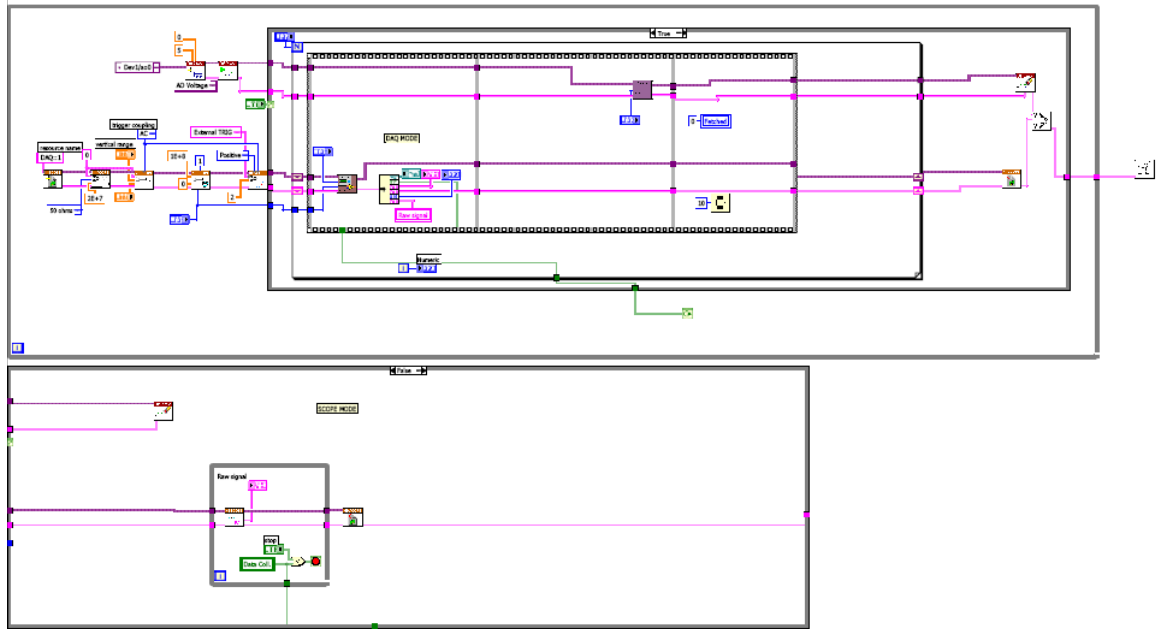
Figure 73: Ratio of temporal profiled 700/1064 nm for all four sheep at both cycles (1st cycle blue diamonds, 2nd cycle red squares).

BLOCK DIAGRAMS OF LABVIEW PROGRAMS USED FOR DATA ACQUISITION AND PROCESSING

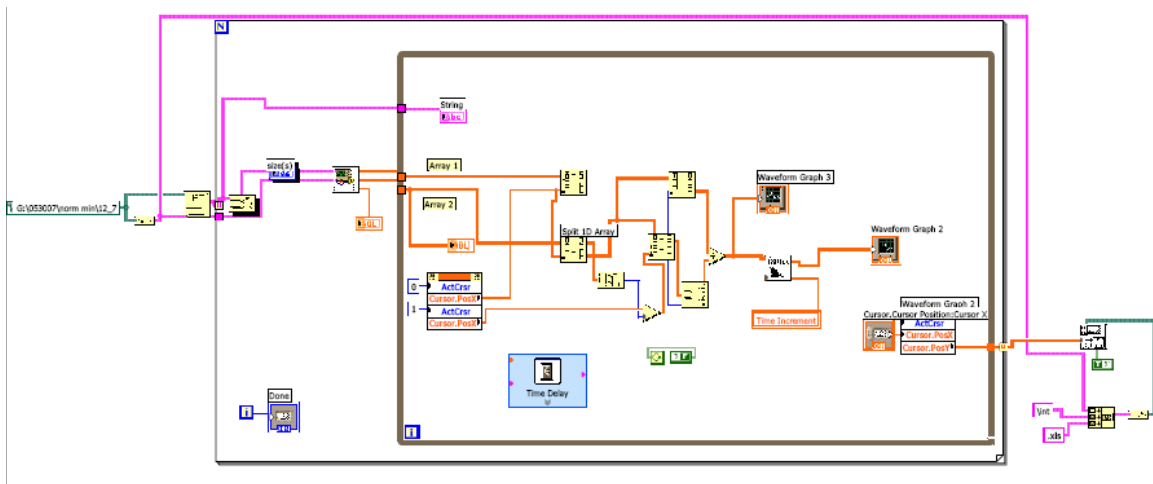
Program for data acquisition of a single file



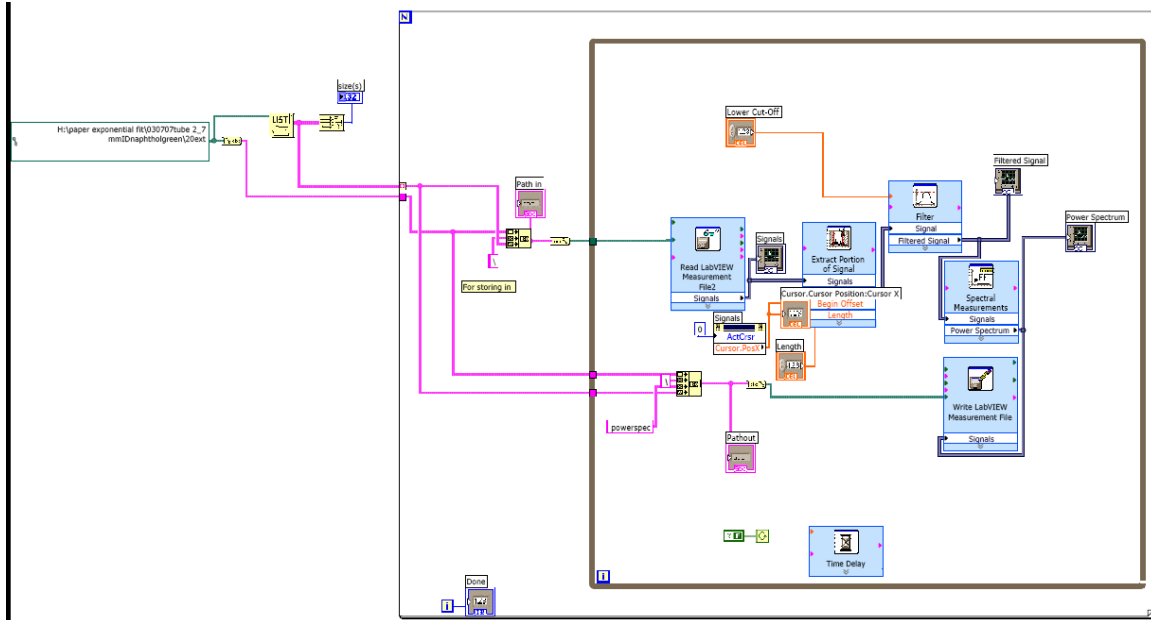
Program for data acquisition and probe scanning



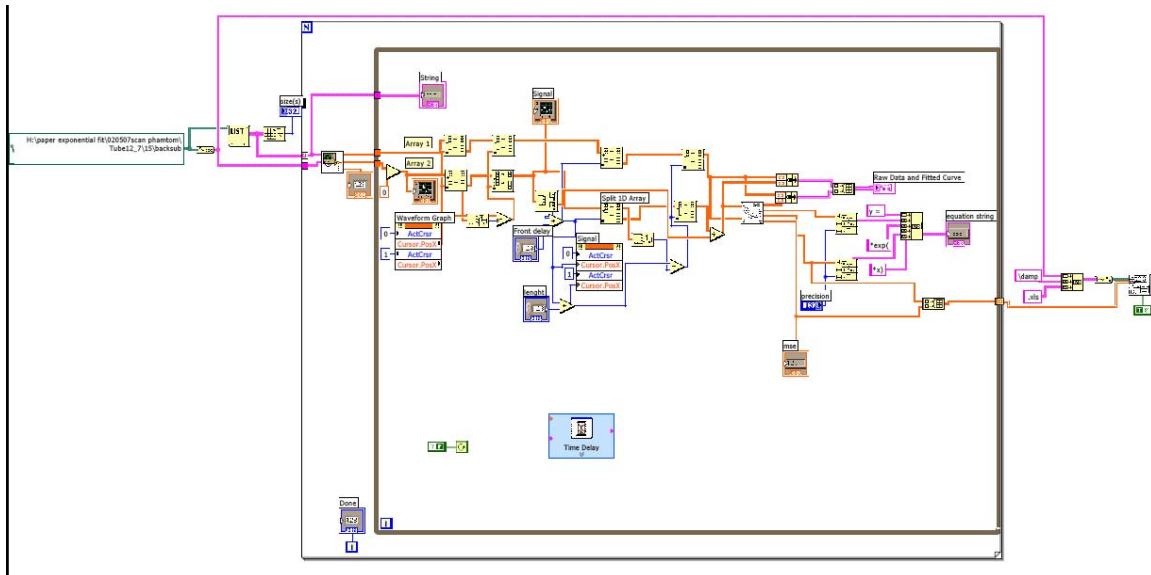
Program for determination of value of integral



Program for determination of power spectrum



Program for determination of the exponential coefficient



REFERENCES

1. J. A. Langlois and R. W. Sattin, "Traumatic brain injury in the United States: Research and programs of the Centers for Disease Control and Prevention (CDC) - Preface," *Journal of Head Trauma Rehabilitation* **20**, 187-188 (2005).
2. J. Cruz, M. E. Miner, S. J. Allen, W. M. Alves, and T. A. Gennarelli, "Continuous Monitoring of Cerebral Oxygenation in Acute Brain Injury - Injection of Mannitol During Hyperventilation," *Journal of Neurosurgery* **73**, 725-730 (1990).
3. Z. Feldman and C. S. Robertson, "Monitoring of cerebral hemodynamics with jugular bulb catheters," *Critical Care Clinics* **13**, 51 (1997).
4. B. F. Matta, A. M. Lam, T. S. Mayberg, Y. Shapira, and H. R. Winn, "A Critique of the Intraoperative Use of Jugular Venous Bulb Catheters During Neurosurgical Procedures," *Anesthesia and Analgesia* **79**, 745-750 (1994).
5. D. E. Remmers, W. G. Cioffi, K. I. Bland, P. Wang, M. K. Angele, and I. H. Chaudry, "Testosterone: The crucial hormone responsible for depressing myocardial function in males after trauma-hemorrhage," *Annals of Surgery* **227**, 790-796 (1998).
6. C. S. Robertson, A. B. Valadka, J. Hannay, C. F. Contant, S. P. Gopinath, M. Cormio, M. Uzura, and R. G. Grossman, "Prevention of secondary ischemic insults after severe head injury," *Critical Care Medicine* **27**, 2086-2095 (1999).
7. A. W. Unterberg, K. L. Kiening, R. Hartl, T. Bardt, A. S. Sarrafzadeh, and W. R. Lanksch, "Multimodal monitoring in patients with head injury: Evaluation of the effects of treatment on cerebral oxygenation," *Journal of Trauma-Injury Infection and Critical Care* **42**, S32-S37 (1997).
8. A. Zauner, E. M. R. Dopperberg, J. J. Woodward, S. C. Choi, H. F. Young, and R. Bullock, "Continuous monitoring of cerebral substrate delivery and clearance: Initial experience in 24 patients with severe acute brain injuries," *Neurosurgery* **41**, 1082-1091 (1997).
9. D. A. Boas, J. P. Culver, J. J. Stott, and A. K. Dunn, "Three dimensional Monte Carlo code for photon migration through complex heterogeneous media including the adult human head," *Optics Express* **10**, 159-170 (2002).
10. J. Dings, A. Jager, J. Meixensberger, and K. Roosen, "Brain tissue pO₂ and outcome after severe head injury," *Neurol. Res.* **20 Suppl 1**, S71-S75 (1998).

11. J. Dings, J. Meixensberger, and K. Roosen, "Brain tissue pO₂-monitoring: catheter stability and complications," *Neurol. Res.* **19**, 241-245 (1997).
12. A. Roggan, M. Friebel, K. Dorschel, A. Hahn, and G. Muller, "Optical properties of circulating human blood in the wavelength range 400-2500 NM," *Journal of Biomedical Optics* **4**, 36-46 (1999).
13. P. J. Kirkpatrick, P. Smielewski, P. C. Whitfield, M. Czosnyka, D. Menon, and J. D. Pickard, "An Observational Study of Near-Infrared Spectroscopy During Carotid Endarterectomy," *Journal of Neurosurgery* **82**, 756-763 (1995).
14. W. J. Levy, S. Levin, and B. Chance, "Near-Infrared Measurement of Cerebral Oxygenation - Correlation with Electroencephalographic Ischemia During Ventricular-Fibrillation," *Anesthesiology* **83**, 738-746 (1995).
15. V. Pollard, D. S. Prough, A. E. Demelo, D. J. Deyo, T. Uchida, and R. Widman, "The influence of carbon dioxide and body position on near-infrared spectroscopic assessment of cerebral hemoglobin oxygen saturation," *Anesthesia and Analgesia* **82**, 278-287 (1996).
16. V. Pollard, E. Demelo, D. J. Deyo, and D. S. Prough, "The Effect of Carbon-Dioxide and Position Change on Near-Infrared Spectroscopic Assessment of Cerebral Hemoglobin Saturation," *Anesthesiology* **81**, A531 (1994).
17. Invos Cerebral Blood Oximeter. www.somanetics.com/invos_principles.htm. Accessed 9-9-2007.
18. J. K. Barton, T. J. Pfefer, A. J. Welch, D. J. Smithies, J. S. Nelson, and M. J. C. van Gemert, "Optical Monte Carlo modeling of a true port wine stain anatomy," *Optics Express* **2**, 391-396 (1998).
19. T. Bowen, "Radiation-Induced Thermoacoustic Soft Tissue Imaging," 817-822 Proceedings IEEE Ultrasonics Symposium, (1981).
20. T. Bowen, L. Nasoni, A. E. Pifer, and G. H. Sembrosk, "Some Experimental Results on the Thermoacoustic Imaging of Soft Tissue-Equivalent Phantoms," 823-827 (1981).
21. H. P. Brecht, D. S. Prough, Y. Y. Petrov, I. Y. Petrova, D. Deyo, and R. O. Esenaliev, "Accurate, noninvasive measurement of total hemoglobin concentration with optoacoustic technique," *Conf. Proc. IEEE Eng Med. Biol. Soc.* **1**, 375-376 (2004).
22. H. P. Brecht, Prough DS, Petrov YY, I. Patrieev, and Esenaliev RO, "Scanning system for noninvasive optoacoustic monitoring of blood oxygenation in the internal jugular vein," Conference proceeding A.A.Oraevsky and L.V.Wang, eds., *Photons plus Ultrasound, SPIE*, (2007).

23. J. A. Copland, M. Eghtedari, V. L. Popov, N. Kotov, N. Mamedova, M. Motamedi, and A. A. Oraevsky, "Bioconjugated gold nanoparticles as a molecular based contrast agent: Implications for imaging of deep tumors using optoacoustic tomography," *Molecular Imaging and Biology* **6**, 341-349 (2004).
24. D. J. Deyo, R. O. Esenaliev, O. Hartrumpf, M. Motamedi, and D. S. Prough, "Continuous Non-invasive Optoacoustic Monitoring of Hemoglobin Saturation," *Anesthesia and Analgesia*, **92**, p140 (2001).
25. S. Y. Emelianov, M. A. Lubinski, A. R. Skovoroda, R. Q. Erkamp, S. F. Leavey, R. C. Wiggins, and M. O'Donnell, "Reconstructive ultrasound elasticity imaging for renal transplant diagnosis: kidney ex vivo results," *Ultrason. Imaging* **22**, 178-194 (2000).
26. S. Y. Emelianov, X. Chen, M. O'Donnell, B. Knipp, D. Myers, T. W. Wakefield, and J. M. Rubin, "Triplex ultrasound: elasticity imaging to age deep venous thrombosis," *Ultrasound Med. Biol.* **28**, 757-767 (2002).
27. R. O. Esenaliev, A. A. Oraevsky, V. S. Letokhov, A. A. Karabutov, and T. V. Malinsky, "Studies of Acoustical and Shock-Waves in the Pulsed-Laser Ablation of Biotissue," *Lasers in Surgery and Medicine* **13**, 470-484 (1993).
28. R. O. Esenaliev, A. A. Karabutov, and A. A. Oraevsky, "Sensitivity of laser opto-acoustic imaging in detection of small deeply embedded tumors," *IEEE Journal of Selected Topics in Quantum Electronics* **5**, 981-988 (1999).
29. R. O. Esenaliev, I. V. Larina, K. V. Larin, D. J. Deyo, M. Motamedi, and D. S. Prough, "Optoacoustic technique for noninvasive monitoring of blood oxygenation: a feasibility study," *Applied Optics* **41**, 4722-4731 (2002).
30. R. O. Esenaliev, Y. Y. Petrov, O. Hartrumpf, D. J. Deyo, and D. S. Prough, "Continuous, noninvasive monitoring of total hemoglobin concentration by an optoacoustic technique," *Applied Optics* **43**, 3401-3407 (2004).
31. A. A. Karabutov, N. B. Podymova, and V. S. Letokhov, "Time-resolved laser optoacoustic tomography of inhomogeneous media," *Applied Physics B-Lasers and Optics* **63**, 545-563 (1996).
32. A. A. Karabutov, E. V. Savateeva, and A. A. Oraevsky, "Optoacoustic tomography: New modality of laser diagnostic systems," *Laser Physics* **13**, 711-723 (2003).
33. R. G. M. Kolkman, M. C. Pilatou, E. Hondebrink, and F. F. M. De Mul, "Photo-acoustic A-scanning and monitoring of blood content in tissue," *Conference Proceeding In Biomedical Optoacoustics*, 3916, p76-83 (2000).

34. R. G. M. Kolkman, J. H. G. M. Klaessens, E. Hondebrink, J. C. W. Hopman, F. F. M. De Mul, W. Steenbergen, J. M. Thijssen, and T. G. van Leeuwen, "Photoacoustic determination of blood vessel diameter," *Physics in Medicine and Biology* **49**, 4745-4756 (2004).
35. K. V. Larin, I. V. Larina, M. Motamedi, and R. O. Esenaliev, "Optoacoustic laser monitoring of cooling and freezing of tissues," *Quantum Electronics* **32**, 953-958 (2002).
36. K. V. Larin, I. V. Larina, and R. O. Esenaliev, "Monitoring of tissue coagulation during thermotherapy using optoacoustic technique," *Journal of Physics D-Applied Physics* **38**, 2645-2653 (2005).
37. I. V. Larina, K. V. Larin, and R. O. Esenaliev, "Real-time optoacoustic monitoring of temperature in tissues," *Journal of Physics D-Applied Physics* **38**, 2633-2639 (2005).
38. J. Laufer, R. Simpson, M. Kohl, M. Essenpreis, and M. Cope, "Effect of temperature on the optical properties of ex vivo human dermis and subdermis," *Physics in Medicine and Biology* **43**, 2479-2489 (1998).
39. J. Laufer, C. Elwell, D. Delpy, and P. Beard, "In vitro measurements of absolute blood oxygen saturation using pulsed near-infrared photoacoustic spectroscopy: accuracy and resolution," *Physics in Medicine and Biology* **50**, 4409-4428 (2005).
40. J. Laufer, D. Delpy, C. Elwell, and P. Beard, "Quantitative spatially resolved measurement of tissue chromophore concentrations using photoacoustic spectroscopy: application to the measurement of blood oxygenation and haemoglobin concentration," *Physics in Medicine and Biology* **52**, 141-168 (2007).
41. J. Lee, N. El Abaddi, A. Duke, A. E. Cerussi, M. Brenner, and B. J. Tromberg, "Noninvasive in vivo monitoring of methemoglobin formation and reduction with broadband diffuse optical spectroscopy," *Journal of Applied Physiology* **100**, 615-622 (2006).
42. I. Patrikeev, Y. Y. Petrov, I. Y. Petrova, D. S. Prough, and R. O. Esenaliev, "Monte Carlo modeling of optoacoustic signals from human internal jugular veins," *Applied Optics* **46**, (2007).
43. Y. Y. Petrov, D. S. Prough, D. J. Deyo, M. Klasing, M. Motamedi, and R. O. Esenaliev, "Optoacoustic, noninvasive, real-time, continuous monitoring of cerebral blood oxygenation: An in vivo study in sheep," *Anesthesiology* **102**, 69-75 (2005).
44. I. Y. Petrova, R. O. Esenaliev, Y. Y. Petrov, H. P. E. Brecht, C. H. Svensen, J. Olsson, D. J. Deyo, and D. S. Prough, "Optoacoustic monitoring of blood

- hemoglobin concentration: a pilot clinical study," *Optics Letters* **30**, 1677-1679 (2005).
45. Gray's Anatomy Online. <http://www.bartleby.com/107/168.html>. 3-3-2007.
 46. A.G.Bell, "On the Production and Reproduction of Sound by Light: the Photophone," *American Journal of Science* **3**, 305-324 (1880).
 47. V. E. Gusev and A. A. Karabutov, "Introduction," in *Laser Optoacoustics*, (American Institute of Physics, New York, 1993), pp. XI-XVII.
 48. A. J. Welch and M. J. C. Van Gemmert, *Optical thermal response of laser irradiated tissues*, (Plenum Press, New York, 1995).
 49. G. Fleury and C. Gondard, "Improvements of Ultrasonic Inspections through the use of Piezo Composite Transducers," Nice, France, (1994).
 50. Iowa State University. Website for Non destructive testing Iowa State University, <http://www.ndted.org/EducationResources/CommunityCollege/Ultrasonics/Physics/acousticimpedance.htm>. 1-1-2005.
 51. H. Vogel, "Kapazitaet," in *Gerthsen Physik*, (Springer Verlag, Berlin - Heidelberg, 1999), pp. 305-317.
 52. H. Wang, T. Ritter, C. Wenwu, and K. Shung, "Passive Materials for High Frequency Ultrasound Transducers," SPIE, San Diego, 35-42 (1999).
 53. ONDA Cooperation. Preamplifier Selection Table, http://www.ondacorp.com/products_testingsol_selection_table.html. 3-14-2007.
 54. "ANSI Z136.3 - 1996," in *American national standard for safe use of lasers in health care facilities*: (The Laser Institute of America, Orlando, FL, 2001).
 55. "ANSI Z136.1 - 2000," in *American national standard for safe use of lasers*, (The Laser Institute of America, Orlando, FL, 2000).
 56. H. P. Brecht, D. S. Prough, D. J. Deyo, Y. Y. Petrov, I. Cicenaitis, and R. O. Esenaliev, "Monitoring of Blood Oxygenation in Large Veins with a Triple-Wavelength Optoacoustic System," *Optics Express* (in Press) (2007).
 57. Karabutov, A. A., Savateeva, E. V., Podymova, N. B., and Oraevsky, A. A. Backward mode detection of laser-induced wide-band ultrasonic transients with optoacoustic transducer. *Journal of Applied Physics* **87**[4], 2003-2014. 2-15-2000.
 58. Y. Y. Petrov, I. Y. Petrova, I. A. Patrikeev, R. O. Esenaliev, and D. S. Prough, "Multiwavelength optoacoustic system for noninvasive monitoring of

- cerebral venous oxygenation: a pilot clinical test in the internal jugular vein," *Opt. Lett.* **31**, 1827-1829 (2006).
59. S. A. Prahl,
Optical Absorption of Hemoglobin,
<http://omlc.ogi.edu/spectra/hemoglobin/index.html>. 4-2-2007.
 60. Y. Y. Petrov, D. S. Prough, D. J. Deyo, I. Y. Petrova, M. Motamedi, and R. O. Esenaliev, " In vivo noninvasive monitoring of cerebral blood oxygenation with optoacoustic technique.," IEEE, San Francisco, 2052-2054 (2004).
 61. W. F. Cheong, S. A. Prahl, and A. J. Welch, "A review of the optical properties of biological tissues," *IEEE Transactions on Medical Imaging* **26**, 2166-2185 (1990).
 62. A. N. Yaroslavsky, I. V. Yaroslavsky, T. Goldbach, and G. H. Sembrosk, "The Optical Properties of blood in the near infrared spectral range," D. L. Farkas, R. C. Leif, A. V. Priezzhev, T. Asakura, and B. J. Tromberg, eds., *Proceeding Spie*, 314-324 (1996).
 63. I. Driver, J. W. Feather, P. R. King, and J. B. Dawson, "The optical properties of aqueous suspensions of Intralipid, a fat emulsion," *Physics in Medicine and Biology* **34**, 1927-1930 (1989).
 64. H. J. Vanstaveren, C. J. M. Moes, J. Vanmarle, S. A. Prahl, and M. J. C. Vangemert, "Light-Scattering in Intralipid-10-Percent in the Wavelength Range of 400-1100 Nm," *Applied Optics* **30**, 4507-4514 (1991).
 65. J. T. Kuenstner, K. Norris, and V. F. Kalasinsky, "Spectrophotometry of human hemoglobin in the midinfrared region," *Biospectroscopy* **3**, 225-232 (1997).
 66. J. M. Steinke and A. P. Shepherd, "Effects of Temperature on Optical Absorbency Spectra of Oxyhemoglobin, Carboxyhemoglobin, and Deoxyhemoglobin," *Clinical Chemistry* **38**, 1360-1364 (1992).
 67. B. L. Horecker, "The absorption spectra of hemoglobin and its derivatives in the visible and near infra-red regions," *Journal of Biological Chemistry* **148**, 173-183 (1943).
 68. L. L. Randeberg, J. H. Bonesronning, M. Dalaker, J. S. Nelson, and L. O. Svaasand, "Methemoglobin formation during laser induced photothermolysis of vascular skin lesions," *Lasers in Surgery and Medicine* **34**, 414-419 (2004).
 69. W. G. Zijlstra, A. Buursma, and W. P. Meeuwsenvanderroest, "Absorption-Spectra of Human Fetal and Adult Oxyhemoglobin, De-Oxyhemoglobin,

Carboxyhemoglobin, and Methemoglobin," *Clinical Chemistry* **37**, 1633-1638 (1991).

70. R. G. M. Kolkman, E. Hondebrink, W. Steenbergen, T. G. van Leeuwen, and F. F. M. De Mul, "Photoacoustic imaging of blood vessels with a double-ring sensor featuring a narrow angular aperture," *Journal of Biomedical Optics* **9**, 1327-1335 (2004).
71. G. M. Spirou, A. A. Oraevsky, I. A. Vitkin, and W. M. Whelan, "Optical and acoustic properties at 1064 nm of polyvinyl chloride-plastisol for use as a tissue phantom in biomedical optoacoustics," *Physics in Medicine and Biology* **50**, N141-N153 (2005).
72. I. Patrikeev, Personal Communication 1-2-2007.
73. I. Patrikeev, Y. Y. Petrov, I. Y. Petrova, D. S. Prough, and R. O. Esenaliev, "Monte Carlo Modeling of Optoacoustic Signals from Large Veins: Implication for Noninvasive Monitoring of Cerebral Blood Oxygenation ," *Biomedical Optics 2006 Technical Digest* (2006).